Electrostatic Zipping Actuators and Their Application to MEMS

by

Jian Li

B.S., Precision Instruments, Tsinghua University (1997)
M.S., Precision Instruments, Tsinghua University (2000)

Submitted to the Department of Mechanical Engineering
in partial fulfillment of the requirements for the degree of

Doctor of Philosophy in Mechanical Engineering

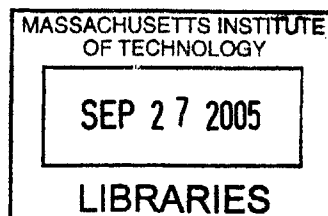at the

MASSACHUSETTS INSTITUTE OF TECHNOLOGY

February 2004

Author . . . .
Department of Mechanical Engineering
January 22, 2004

Certified by . .
Alexander H. Slocum
Professor of Mechanical Engineering
Thesis Supervisor

Certified by . .
Jeffrey H. Lang
Professor of Electrical Engineering and Computer Science
Thesis Supervisor

Accepted by . .
Ain A. Sonin
Chairman, Department Committee on Graduate Students

Electrostatic Zipping Actuators and Their Application to MEMS

by

Jian Li

Abstract

Electrostatic actuation is the most common and well-developed method of generating motion on the micro scale. To overcome the challenge of providing both high force and large displacement, electrostatic zipping actuators have been developed and applied to various devices. As device thicknesses increase, however, conventional laterally-moving zipping actuators become less practical due to their high pull-in voltages caused by their minimum achievable electrode gaps.

This thesis presents a fundamental improvement of the laterally-moving electrostatic zipping actuator. Its major contributions are: 1) a compliant starting zone is introduced into the fixed electrode to significantly reduce the pull-in voltage of the zipping electrode; 2) numerical and analytical methods are developed to solve general zipping actuator problems; 3) optimization is performed to minimize the effort required to actuate the zipping electrode and its load; and 4) the improved zipping actuators are designed into a relay to illustrate their use and performance.

To design a cross-bar micro relay, two zipping actuators are combined with a curved bistable switch beam and two contacts. The micro relay is monolithically fabricated in silicon using deep reactive ion etching to move laterally in the wafer plane. Both actuators provided up to 10 mN of actuation force over their 80 μm of stroke at 140 V, and toggle the bistable relay at a maximum rate of 160 Hz. Pull-in voltage, actuation voltage and force-displacement measurements of the actuators and switch beam confirm theoretical expectations based on numerical, analytical and finite element analyses, after accounting for fabrication variations. The shortest pulse required to switch the relay is 400 μs, and the time taken for the actuator to close the relay was approximately 3 ms. The relay was operated at 100 Hz for over 120 hours through more than 40 million cycles without any observed stiction or fracture fatigue.

To achieve low contact resistance for a laterally-moving micro relay, wet anisotropically etched silicon {111} planes are developed to form relay contact surfaces that offer flat wiping surfaces and ease of thick metalization. Experimental contacts are fabricated and their average contact resistance is measured to be $\sim$ 50 mΩ. A process

plan is also proposed to combine the {111} plane contacts with the prior zipping actuators and the switch beam to build a micro relay with low contact resistance for power protection applications.

The compliant starting zone concept can also be applied to vertically-moving MEMS devices. A MEMS valve is also designed using a zipping actuator having compliant starting zones. As another application of the zipping mechanism, a nonlinear spring is also presented and analyzed.

Thesis Supervisor: Alexander H. Slocum
Title: Professor of Mechanical Engineering

Thesis Supervisor: Jeffrey H. Lang
Title: Professor of Electrical Engineering and Computer Science

Acknowledgements

First and foremost, I would like to thank my thesis supervisors Professor Alexander Slocum and Professor Jeffrey Lang, who have given me the opportunity to work in this project technically and financially, have guided me through my Ph.D study and research, have constantly encouraged me, and have spent hours and hours with me attacking problems I met in research. To Alex and Jeff, I cannot thank you enough.

I am indebted to Professor Michael Brenner who provided invalueable help in solving the actuator problem and on the optimization of the system. From Michael I learned a lot in effectively applying mathematics to engineering problems.

Professor Samir Nayfeh reviewed the thesis and provided very helpful comments. Professor Simona Socrate appointied me a Teaching Assistant position for the last term during my Ph.D study. I wish to thank them for their support.

I benefited greatly from Dr. Jin Qiu and Dr. Joachim Sihler who commented on this research. Particularly, I wish to thank Jin for his help on testing the devices and Joachim for his suggestions on fabrication.

I would also like to thank MTL staff for their help during fabrication: Kurt Broderick, Dennis Ward, Paul Tierney, Linvhu Ho, Dr. Hongwei Sun...

I have been blessed by the family of Precision Engineering Research Group (PERG) since I came to MIT. I would thank all PERGers for the pleasure we had together and for the help I got from them.

This thesis is based in part on [1] and [2].

Finally, I would like to thank my parents Qinghan Li and Yizhen Li, and my sister Hui Li for their constant support and encouragement.

Contents

7

9

List of Figures

11

13

15

List of Tables

17

Chapter 1

Introduction

This thesis focuses on electrostatic zipping actuators and their application to MEMS. To achieve high force and large displacement at the same time, the actuator employs a flexible cantilever that zips along a fixed electrode, providing force and motion at the free end. A compliant starting zone is also incorporated into the electrode to significantly reduce its intial pull-in voltage. Two such actuators are incorporated with a bistable beam and two contacts to form a MEMS crossbar relay for power applications. Numerical, analytical and finite element analyses are applied to the modeling, design and optimization of the actuator and the switch beam in order to lessen the force requirement of the actuator. The relay is fabricated monolithically in silicon using DRIE and bonded to a Pyrex substrate. Break-off tabs are then broken to achieve insulation between electrodes. Taking into account fabrication variations, the experimental test data agree well with the theoretical predictions.

This thesis also studies micro relay contacts formed by silicon {111} surfaces. Experimental devices are fabricated and low contact resistance is achieved. A process is also proposed to combine the wet anisotropically etched contacts with DRIE etched actuator and switch beam.

Zipping actuators with compliant starting zone can also be used in vertically-moving MEMS devices. A MEMS valve is designed in this thesis using zipping actuators with compliant starting zones. As another application of zipping mechanism, a nonlinear spring design is also presented.

Section 1.1 addresses the background of MEMS and MEMS actuators. In Section 1.1.2, some existing MEMS actuators are surveyed and different actuation schemes are compared. Section 1.2 describes the motivation and goals of this thesis and Section 1.3 overviews the relay application. Finally, Section 1.4 outlines the thesis frame structure.

1.1 Background

1.1.1 MEMS

Microelectromechanical Systems (MEMS), or Microsystems, are integrated micro devices or systems combining electrical and mechanical components [5] [6]. They are fabricated using integrated circuit (IC) batch processing techniques and can range in size from micrometers to millimeters. Since the earliest MEMS devices were fabricated in the 1960's, MEMS have been used to sense, control and actuate on the micro scale [7]. Among the most successful MEMS devices, micro-machined nozzles are used in ink jet printer cartridges to eject small amounts of ink, which enables high quality color printing at low cost; silicon pressure sensors are used in automobiles to measure acceleration and rotation and decide when to activate airbags during collisions[8]; hundreds of thousands of micro-mirrors are employed in projectors to project images onto a screen [9] [10]. In addition to these examples, MEMS are growing fast into other areas such as biomedicine [11], telecommunications [12] and optics [10].

Most MEMS devices are made by lithography-based microfabrication that is borrowed from the microelectronics industry. With in-plane sub-micron precision, the microfabrication technology makes it possible to build micro-scale mechanical components, such as silicon cantilevers that are a few microns thick. Moreover, the technology enables batch fabrication which can reduce cost when manuracturing in high volume. In addition, because it shares fabrication with conventional microelectronics, there are always opportunities to combine micro mechanical elements with electronic circuits and generate fully integrated micro systems. MEMS microfabrication has also

been extended beyond microelctronics fabrication. For examples, although only two dimensional devices can be built using conventional lithography technology, wafer-bonding and thin-film methods have been developed to allow the creation of three dimensional MEMS devices [13]; Deep Reactive Ion Etching (DRIE) has been employed to etch through the whole depth of silicon wafers; wet anisotropic etching of silicon opens up opportunities to fabricate 3-D structures with crystal planes that are in certain angles with the wafer surface.

Most of the materials used for IC products are silicon and related inorganic materials such as silicon dioxide, silicon nitride, copper and aluminum. The range of materials for MEMS, however, has been extended more broadly. For example, SU-8 as a thick photoresist is widely used to form micro fluidic devices; Pyrex is commonly used to anodically bond to silicon and form more sophisticated micro structures. Many metals like gold are utilized in micro systems to achieve better optical or electrical properties.

As the devices are scaled down, although most macro physical laws are still applicable, the relative importance of different types of phisical effects changes. Micro structures become stiffer and lighter with higher shock resistance; some external forces such as electrostatic, thermal electric and piezoelectric forces are comparable to inertia forces and therefore can be employed to actuate mechanical components.

All of these differences open up opportunities to design MEMS devices that are very different from macro machines. The modeling and analysis of MEMS have also been very different. Numerical analysis is widely applied to MEMS because of their nonlinearity. Commercial FEA packages that are customized for the multi-physics in MEMS are also available. On the other hand, analytical methods are still desirable to achieve insight and understanding and therefore enhance the design and optimization of MEMS.

1.1.2   MEMS actuators

One of the promises of MEMS devices lies in their ability to generate micro scale mechanical motion. The most common driving principles include magnetic, electric,

Actuation Principle	Typical Devices	Voltage	Current
Magnetic	microscanner [16]	about 1 V	hundreds of mAs
Electric	microshutter [17] microrelay [18] [19]	tens of volts to $\sim$ hundreds of volts	nA $\sim$ mA
Electrothermal	microvalves [20]	a few volts to tens of volts	mA $\sim$ tens of mAs
Piezoelectric	micropump [21]	tens of volts to hundreds of volts	nA $\sim$ mA
Shape memory alloy	micropump [22]		

Table 1.1: MEMS actuators using different principles.

electrothermal, piezoelectric and shape memory forces. Each principle has specific advantages and disadvantages with respect to deflection range, required force, power requirement, and response time. A brief overview of each driving principle is shown in Table 1.1 [14] [15]. Among these principles, electric actuation is often applied because of its low power consumption, high actuation speed, good fabrication compatibility and reasonably high energy density. Accordingly, the actuator developed in this thesis is based on electric actuation.

1.2 Motivation

1.2.1 More forceful electrostatic actuators

Although electric actuation has its advantages over other actuation scheme, it is difficult to design an electric actuator with large stroke, high force and simple fabrication process, which are desirable as MEMS is applied to more and more areas, especially when forceful actuation is required.

1.2.2 MEMS relay

Compared to Magnetic Relays (EMR), MEMS relays offer small size, low power consumption, mechanical reliability and integration capability. Compared to Solid State

Properties	Requirements
Stroke	$\geq 80 \ \mu$m
Actuation force	≥ 5 mN
Excitation Voltage	≤ 200 V
Switching time	≤ 4 ms
Power consumption	as small as possible
Size	$< 7 \times 7 \times 1 \ \text{mm}^3$

Table 1.2: functional requirements for the actuator.

Relays (SSR), MEMS relays offer the safety of galvanic isolation. MEMS relays have been built for different applications, including optical switches, RF relays, etc.

To achieve high off-state resistance and low on-state resistance, relay components with large stroke and high contact force are desirable. This, however, would result in a challenging requirement for the actuator that drives the relay.

A bistable structure with precurved shape has been invented [23]. This structure requires no residual stress and can be fabricated using micro fabrication with one mask, which make it a good candidate as switch component for MEMS relays. This beam has a large stroke and high contact force, which achieves high off-state and low on-state resistance. Moreover, due to the inherent bistability, persistent actuation is not required and memory is maintained during power failure.

The functional requirements for the actuators to drive the bistable structure are listed in Table 1.2. Magnetic, elctric and electrothermal actuators were initially studied for actuating the relay beam [24]. However, if conventional designs are employed, estimation shows that electromagnetic actuators would require a current too big or a magnetic field not realizable; Electric actuators would require much larger size than an elctrothermal actuator. Although an electrothermal actuator was finally built to actuate the relay [25], elctric actuators are still highly desirable due to their low power and fast switching speed. Part of the goal of this thesis is thus to build an electrostatic actuator particularly used for a MEMS power relay.

It is usually difficult to achieve low resistance through DRIE-etched laterally-moving MEMS relay contacts, because it is difficult to deposit enough metal on the vertical sidewalls by evaporation or sputtering. Electroplating can be used therein

23

but the fabrication is more complicated and expensive. This thesis thus also considers alternative methods to achieve low relay contact resistance.

1.2.3 Other applications

The actuators designed for the relay are very forceful and hence can be applied to broader areas, such as MEMS valves. The motivation of this thesis also lies on designing general forceful electrostatic actuators and developing design/modeling methodologies for these systems.

1.3 Device overview

1.3.1 The actuators and the switch

Two electric actuators are designed in this thesis and incorporated with the bistable switch beam. As shown in the top view (Figure 1-1) and cross section view (Figure 1-2) of the device, the relay system consists of two layers: silicon device layer and pyrex handle layer. The device is defined using one DRIE through etch in a silicon wafer, and then bonded to handle wafer through the bond pads 12. The flexures then rest on top of recesses etched into the handle wafer and can move laterally. As voltage (140 V in this thesis) is applied between electrode 1, 10 and flexure beams 3 and 7, the fexure beams 3 and 7 are pulled in to the electrodes at the outside ends and push the bistable bistable switch beam 11 through the T bar 6 in the middle and toggle the double beam. Electrode 5 is used to pull the double beam back to initial position by attracting 3 and 7 upward. compliant starting cantilevers 2, 4 ,8 and 9 are utilized to reduce the pull-in voltages and will be discussed in Section 2.2.3. The performance of the actuator and relay system is described in Table 1.3. To form a crossbar relay, contacts can be connected to the bistable relay beam. The contacts will be discussed in Chapter 4
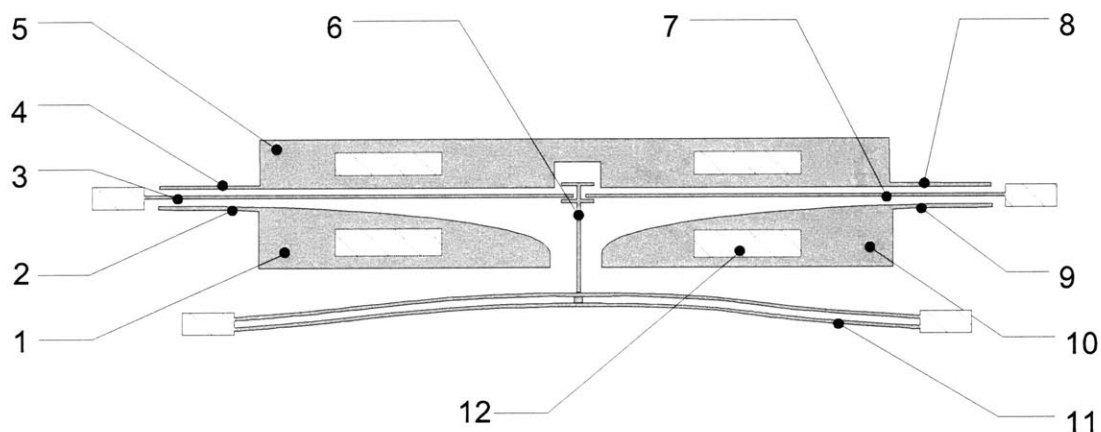
Figure 1-1: device top overview.
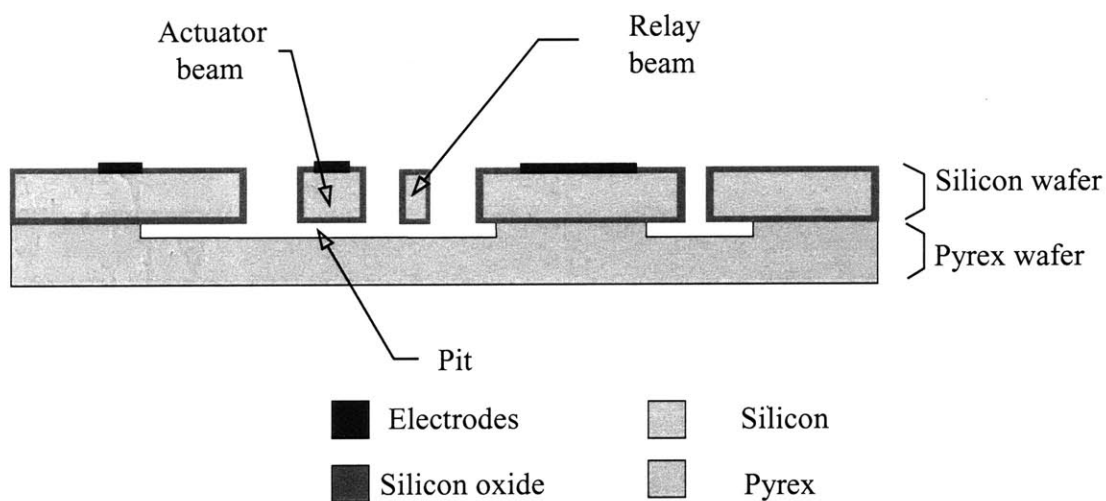
Figure 1-2: device cross section overview.

Properties	Unit	Value
Overall size	mm³	$9 \times 2 \times 0.8$
Actuator stroke	μm	80
Relay stroke	μm	120
Actuator Initial pull-in voltage	V	75
Relay excitation voltage	V	140
Combined actuator force (140 V)	mN	2 - 10
Fracture cycles		$> 4 \times 10^7$
Switching time	ms	3
Shortest excitation pulse	μs	400

Table 1.3: performance of the micro relay system.

25

a) Wet anisotric etch

b) Metal sputtering

c) Bring to contact
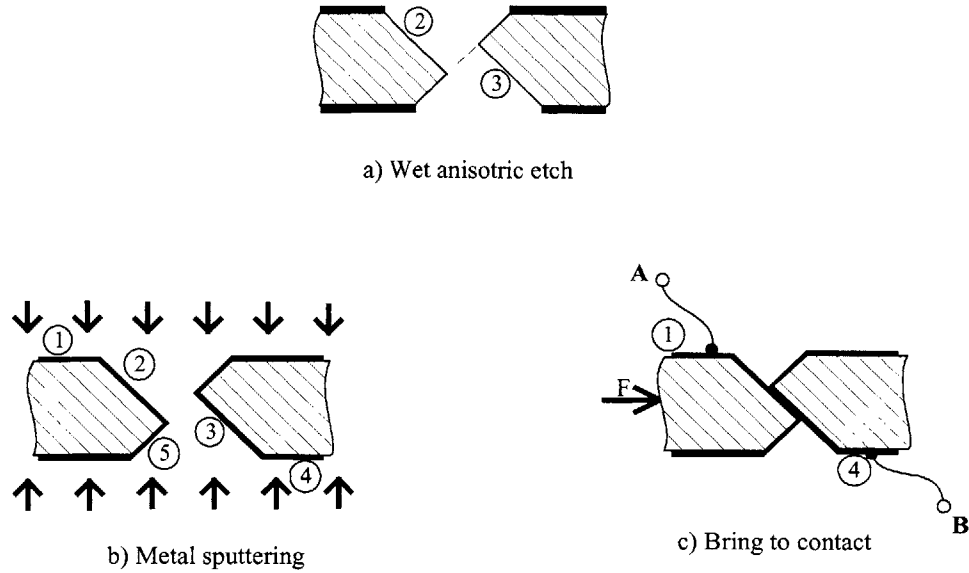
Figure 1-3: wet-anisotropically-etched relay contacts.

1.3.2 Relay contact

DRIE-etched contacts are initally etched in this thesis. The contact resistance is measured to be approximately 1 Ω, which is believed to be caused by low efficiency of sputtering metal to DRIE-etched vertical sidewalls. New contacts are then designed that consist of two parallel wet-anisotropically-etched silicon {111} surfaces, as shown in Figure 1-3. The masks on two sides of the wafer are shifted relative to each other and therefore the two triangles etched from two opposite sides meet in the middle, as shown in Figure 1-3a, forming an overlapped area between the two parallel surfaces 2 and 3. After the structure is released, since surfaces 2 and 3 are slanted with respect to the wafer $\langle 100 \rangle$ surface in an angle of 54.74°, the metal can be easily deposited, as shown in Figure 1-3b. As surface 2 is actuated by the acturator and brought to contact with surface 3, current flows through and low resistance can be achieved between A and B, as shown in Figure 1-3c.

The experimental devices etched in this thesis achieved an average of contact resistance of ~ 50 $m\Omega$, compared to ~ 1 Ω of resistance with DRIE-etched sidewall contacts [26].

26

1.4 Thesis overview

The rest of the thesis is organized as follows. Chapter 2 addresses the design, modeling and analysis of DRIE etched zipping actuators where it is shown that force-displacement characteristics of the actuators satisfy the requirements for a MEMS relay with power applications. Chapter 3 presents the fabrication of MEMS relays actuated by the designed zipper actuators and reports fabrication and measurement results. Chapter 4 descirbes a new design for a MEMS relay contact and a process flow to make the MEMS relay with improved contact resistance. Chapter 5 introduces other applications of the zipping actuators such as a MEMS valve and nonlinear spring. Chapter 6 concludes this thesis and addresses future work. Appendices provide MATLAB code for solving zipping actuator force-displacement problem, a full set of masks for making the device, and a detailed process flow.

Chapter 2

Design and Modeling

This chapter describes the design and modeling of the electrostatic zipping actuators and a MEMS relay actuated by two such actuators. Section 2.1 first introduces three types of electrostatic actuators and compares their force-displacement characteristics when fabricated using DRIE. Section 2.2 then addresses conventional zipping actuators that move in both the vertical and lateral directions. A new type of laterally-moving zipping actuator with a compliant starting cantilever is presented in order to reduce the initial pull-in voltage. Next, Section 2.3 describes numerical, analytical and FEA analyses for the zipping actuators. Finally, Section 2.4 shows the design process for the whole relay based on these analyses.

2.1 Introduction to electrostatic actuators

Electrostatic actuation relies on the coulombic attraction of oppositely charged objects. As an indication of the amount of work that the actuator can perform, the energy stored in the actuator is

$$\Xi = \frac{1}{2}CU^2 = \frac{1}{2}\frac{\varepsilon_0 A U^2}{d} \tag{2.1}$$

where C is the capacitance of the atuator, A is the overlap area of the two objects, U is the actuation voltage, ε_0 is the permittivity of free space and d is the distance

between the energized objects. The energy density according to Equation 2.1 is then

$$\xi = \frac{\Xi}{Ad} = \frac{1}{2}\frac{\varepsilon_0 U^2}{d^2} \qquad (2.2)$$

and the attraction force is

$$F = -\frac{\partial \Xi}{\partial d} = \frac{1}{2}\frac{\varepsilon_0 A U^2}{d^2} \qquad (2.3)$$

As the device is scaled down, electrostatic enrgy density becomes larger as the distance d becomes smaller, assuming that the gap does not break down at constant actuation voltage. Therefore, while electrostatic actuation is not practical in macro machines, MEMS devices can redily take advantage of electrostatic forces. Moreover, power consumption in electrostatic actuation is minimal because only leakage electric current need to be supplied during actuation. Additionally, the electrostatic devices do not require any extra materials and hence the process is comparably easy. Finally, the electrostatic actuation speed can be very high.

However, it is difficult to design an electrostatic actuator with both high actuation force and large displacement. Many devices such as inchworm motors [27] have been designed to overcome this challenge but they suffer from complicated fabrication processes and low yield. To achieve large displacement and high force with relatively simple fabrication process, curved-electrode zipping actuators have been developed.

To demonstrate the advantage of zipping actuators, the geometries and operating principles of comb drive, parallel plate and zipping actuators are shown in Figures 2-1, 2-2 and 2-3, respectively. As shown in Figure 2-1, a comb drive utilizes two sets of interdigitated fingers. Neglecting fringing effects, the capacitance between the electrodes is estimated as

$$C_{comb} = N_{comb}\frac{2\varepsilon_0 \delta b}{g_{min}} = \frac{L}{t + g_{min}}\frac{\varepsilon_0 \delta b}{g_{min}} \qquad (2.4)$$

where N_{comb} is the number of comb pairs in a length of L. The electrostatic attraction force is then calculated by differentiating the total capacitance with respect to the
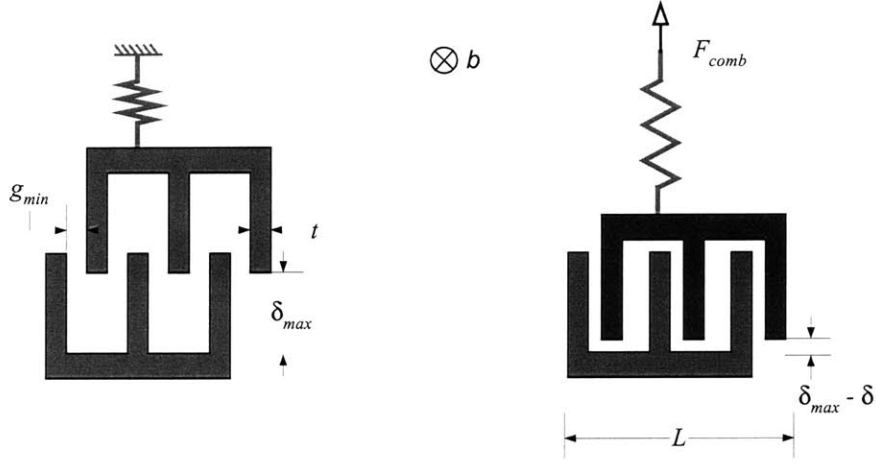
Figure 2-1: comb drive.

displacement δ to obtain

$$F_{comb} = \frac{U^2}{2} \frac{dC_{comb}}{d\delta} = \frac{\varepsilon_0 U^2 bL}{2g_{min}(t + g_{min})} \qquad (2.5)$$

The comb drive actuation force comes from electrostatic shear force and is therefore small. On the other hand, according to Equation 2.5, the force is independent of the displacement δ. Due to these properties, comb drives are commonly used where large displacement is more important [28] than high actuation force.

For a certain device length, voltage and depth, Equation 2.5 also implies that the comb drive becomes more forceful when the gap g_{min} and beam thickness t are smaller. However, for DRIE, the achievable smallest dimensions are constrained by the etching aspect ratio, which is on the order of 5% [29]. A practical minimum dimension for a DRIE through-etch process in a 300 μm wafer, for example, is $t = g_{min} = 15\mu$m. Assume an etching aspect ratio $R_{etching} = b/g_{min}$, where b is the wafer thickness. Equation 2.5 can be written as

$$F_{comb} = \frac{\varepsilon_0 U^2 L}{2(t + b/R_{etching})} \qquad (2.6)$$

In a DRIE through-etch, as used in this thesis, the wafer thickness b is on the order of 300 μm. The comb drive actuation force, according to Equation 2.6, is smaller when

31
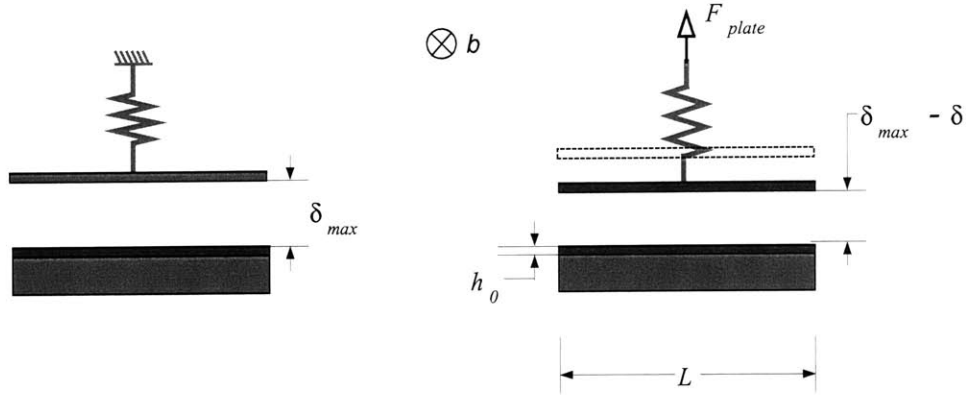
Figure 2-2: parallel plate actuator.

b increases. As a result, comb drives are in general not suitable to manufacture using DRIE.

Parallel plate actuators are shown in Figure 2-2, they have two opposite plates attracting each other and hence create force through the major field lines. Parallel plate actuators are used for many applications, including force rebalance in accelerometers [30] [31], deformable optics [32], relays [33], and valves [34]. To avoid short circuits, an insulation layer of thickness h_0 and relative permittivitty ε_r is built in between the two electrodes. The force is given by

$$F_{plate} = \frac{\varepsilon_0 b L U^2}{2(\delta_{max} - \delta + h_0/\varepsilon_r)^2} \tag{2.7}$$

When the gap between two electrodes is large, as can be concluded from Equation 2.7, the attraction force is very small. this implies that parallel plate actuator can get a relative large force only when the stroke is small.

As shown in Figure 2-3, curved electrode zipping actuators utilize one bendable beam opposite a fixed electrode with an insulation layer in between to prevent a short circuit. When electrified, one end of the beam will be pulled-in to the electrode and a high force can be created at the other end. Large displacements can be achieved with high force.

To compare the characteristics of the three different types of actuators, their force-displacement curves are plotted in Figure 2-4. The forces of the comb drives
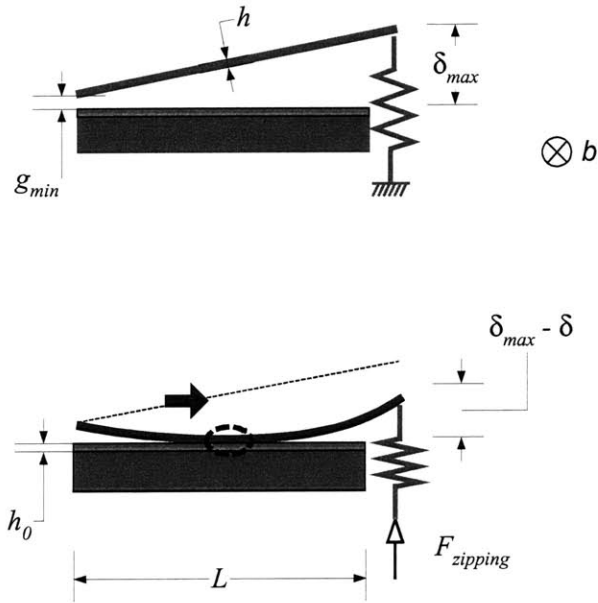
Figure 2-3: zipping actuator.

and parallel plate actuators are based on Equations 2.5 and 2.7. The zipping actuator force is generated from the numerical and analytical analyses described in Section 2.3. The dimensions of the actuators are listed in Table 2.1. Here the DRIE aspect ratio has been considered so that the minimum gap is assumed to be $g_{min} = 15 \ \mu$m. As can be seen, the comb drive outputs a force of approximately 0.3 mN over the full range of actuation. Parallel plates generate very small forces (~ 0.01 mN) at the beginning but become much stronger in the last 10 μm of displacement. As expected, a zipping actuator is much more forceful: it provides from 3 to 10 mN over the full range: the zipping beam acts lke a force integrator. Hence, curved electrode zipping actuators are good candidates for actuating relays and other MEMS devices intended for heavy load.

It is worth noting that the calculation of the zipping actuator actuation force assumes pull-in already happens. However, this may not be true, especially if the minimum gap distance between the two electrodes is large. If the pull-in voltage is higher than the assumed actuation voltage (150 V in this case) or even higher than the acceptable voltage (e.g., 200 V for the relay), one can not design such an actuator assuming the characteristics shown in Figure 2-4. The pull-in voltage is discussed in

33

Symbol (units)	Name	Value
U (volts)	Actuation voltage	150
ε_0 (F/m)	Permittivity of free space	8.85×10^{-12}
ε_r	Relative permittivity of S_iO_2	3.8
$b(\mu m)$	Wafer depth	300
$L(\mu m)$	Device length	4500
g_{min} (μm)	Minimum gap	15
t (μm)	Minimum beam thickness	10
h (μm)	Bending beam thickness	20
δ (μm)	Displacement	$0 \sim 80$
δ_{max} (μm)	Maximum displacement	80
h_0 (μm)	Insulation layer thickness	0.4

Table 2.1: dimensions of the actuators as shown in Figures 2-1, 2-2 and 2-3.

details in Section 2.2 and a new design is then employed to overcome this challenge.

2.2 Design

2.2.1 Conventional zipping actuators

The idea of using a flexible zipping cantilever to provide actuation force was first presented in the early 1990's by Bonne [35] et al. Since then, many curved electrode zipping actuators have been reported. They have demonstrated high force and/or large displacement in both vertical and lateral directions.

In [3], an S-shaped film was sandwiched in two electrodes to obtain a vertical displacement of 220 μm by zipping along the two electrodes. In [18], a zipping cantilever was used to actuate a micro relay vertically and a contact force of 0.28 mN was achieved at 19 V by the cantilever. In [36], vertically moving zipping actuators were employed to deform micro mirrors with a displacement of more than 6 μm and actuation force of 100 μN at 150 V. Vertical curved electrodes were formed utilizing RIE lag [37] and membrane buckling [38]; membranes were then bonded against the curved electrodes to form the actuator and achieve relatively large displacement.

While vertical zipping actuators can be made using wafer bonding, lateral zipping actuators can be etched with one mask step and therefore simplify the fabrication

34
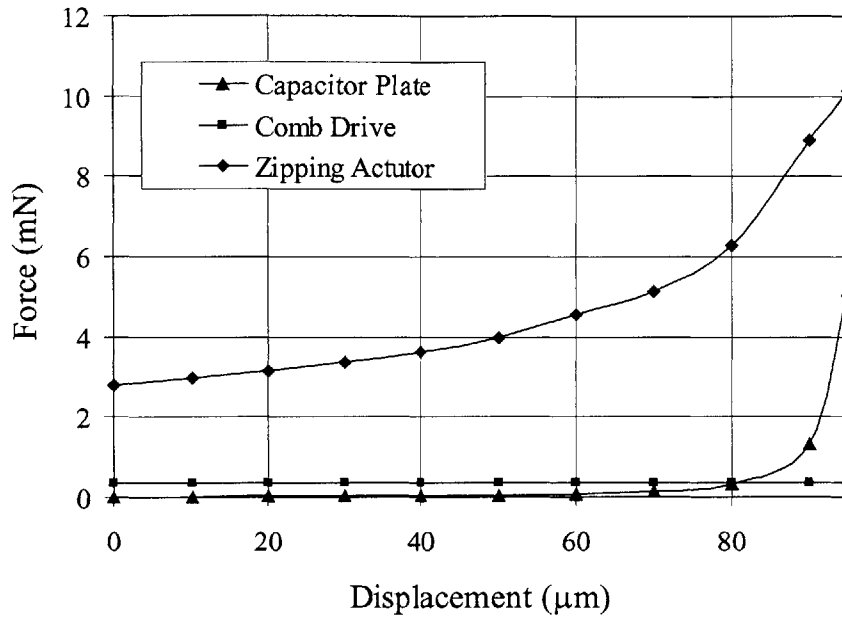
Figure 2-4: force-displacement curves of comb drive, parallel plate and curved electrode zipping actuator with the same dimensions as listed in Table 2.1.

process. In [4], a laterally compliant curved-electrode actuator was first demonstrated and a semi-analytical model based on the Rayleigh-Ritz method was developed. Finite element analysis (FEA) was also employed using MEMCAD™. Laterally moving large displacement curved electrode actuators have been utilized to actuate optical shutters [39], switch mirrors [17] and control fluid flow [40] where large displacements are important. A curved electrode actuator using KOH etching and bonding technology was proposed in [41] to achieve high force and lateral large displacement. In [42], DRIE etched laterally moving zipping actuators were fabricated; experimental data showed that zipping actuators have larger force and displacement than either comb drives or electro-thermal actuators with the same volume. To analyze the pull-in voltage, force and displacement characteristics of curved electrode zipping actuators, semi-analytical models developed in [4] and/or FEA is typically applied.

2.2.2 Pull-in voltage

As described in 2.1, with parallel plate and comb drive type actuators, pull-in must be prevented in order to stabilize the actuation. For zipping actuators, however, pull-in is required at the left end of the bending beam (as shown in Figure 2-3) to start the actuation. However, the pull-in voltage is influenced by the minimum gap between the two electrode. It was observed in [42] [43] [44]that zipping actuators work well only if the two electrodes are very close at the edge from the very beginning. Increase of the initial gap can dramatically increase the functional voltage as experimentally presented in [18].

In vertically moving actuators, the initial gap can be very thin by utilizing a thin sacrificial layer [44] or nearly zero by bonding two electrodes [3] (as shown in 2-5) [37] [38]. As a result, pull-in voltage can be relatively low.

In laterally moving actuators [4] [39] [40] [42], however, the initial gap is limited by the DRIE etching aspect ratio [42], which creates a kerf. Hence the depths of these actuators are generally very small. For laterally moving zipping actuators, since the attraction force is proportional to the elctrode area, i.e. the depth, the force capabilities of these actuators are very small. Figure 2-6 shows a lateral actuator [4] that has a depth of 5 μm. The calculation showed that the pull-in voltage was approximately 50 V and the actuation force on the order was 10 μN at 200 V. If the depth increases to the whole depth of a wafer, e.g. 300 μm, the force would be 60 times larger. To etch through 300 μm, an aspect ratio of 5% leads to a minimu gap of 15 μm and calculation shows that the pull-in voltage for a device with 4.5 mm of length and 80 μm of stroke is 250 V, which is much higher than the acceptible value of the MEMS relay to be built.

2.2.3 Compliant starting cantilever

To overcome the limitation described above and thus lower the pull-in voltage, a compliant starting zone is designed as shown in Figure 2-7. A flexible actuator cantilever is clamped at one end and the other end is attached to the device to be actuated. At
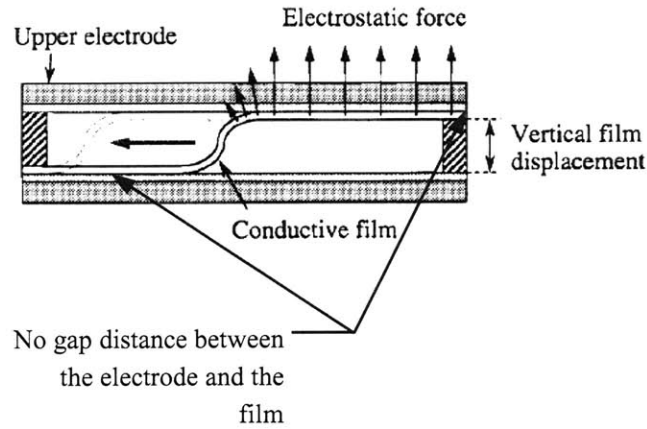
Figure 2-5: a vertically moving curved electrode zipping actuator [3]. The initial gap is eliminated by bonding the conductive film to the elctrode at its two ends.
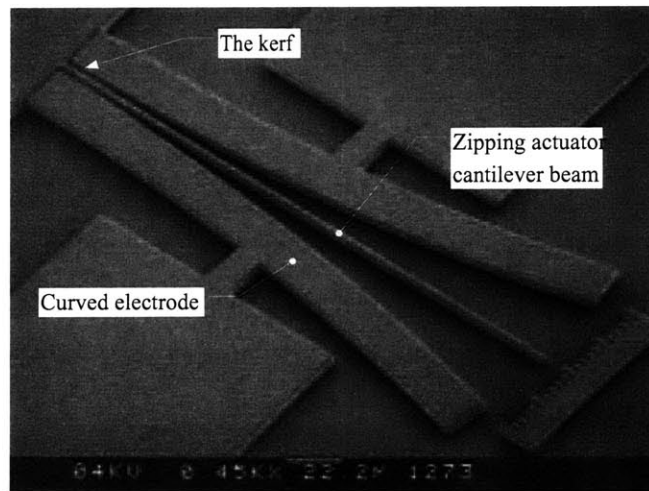
Figure 2-6: a laterally moving curved electrode zipping actuator [4]. The kerf created due to etching aspect ratio results in a relatively high initial pull-in voltage.

the anchored base of the actuator cantilever, the electrode has a very compliant start-ing cantilever. The gap between the actuator cantilever and the electrode increases along the length. The initial gap is limited by device depth and etching aspect ratio. As described above, this gap would normally result in a very high starting (pull-in) voltage of the actuator. However, here as a voltage is applied, the compliant starting cantilever is first easily attracted to the opposing actuator cantilever and the gap between the two electrodes closes. In other words, the compliant starting cantilever pulls-in to the actuator cantilever at low voltage and the electrode shape is modified by the initial voltage to eliminate the kerf. Once the compliant starting cantilever makes contact, the electrostatic forces strongly increase and the actuator cantilever can begin to zip. As the actuator cantilever zips along the electrode, the right end of the cantilever moves down with the device being actuated with a relatively low voltage as the actuation force continually increases. The motion of the actuator is parallel to the wafer plane and this device can be fabricated using DRIE with one single mask. To prevent an electrical short circuit between actuator cantilever and the electrode, a dielectric layer such as thermal oxide is used. Although this design is shown essentially as a 2-D structure, the idea of a compliant starting electrode can be also applied to 3-D structures such as membranes or valves, as will be described in Chatper 5.

Early attempts to utilize a zipping electrostatic actuator for a bistable relay were thwarted by the high pull-in voltages that would be required. The observation that the starting region contributes little to the final force generated, and application of the philosophy of reversal and self-help [45] led to the idea of cutting away the portion of the electrode that does not really contribute much to the total net force to make it compliant in the starting region.

Two curved-electrode zipping actuators with compliant starting cantilevers are designed to actuate a bistable MEMS relay. The relay beam is designed as two pre-curved beams clamped to each other at the middle to achieve bistability without pre-stress [23]. In order to achieve high off-state resistance and low on-state resistance, the relay beam requires a large stroke of 120 μm and a high actuation force on the order
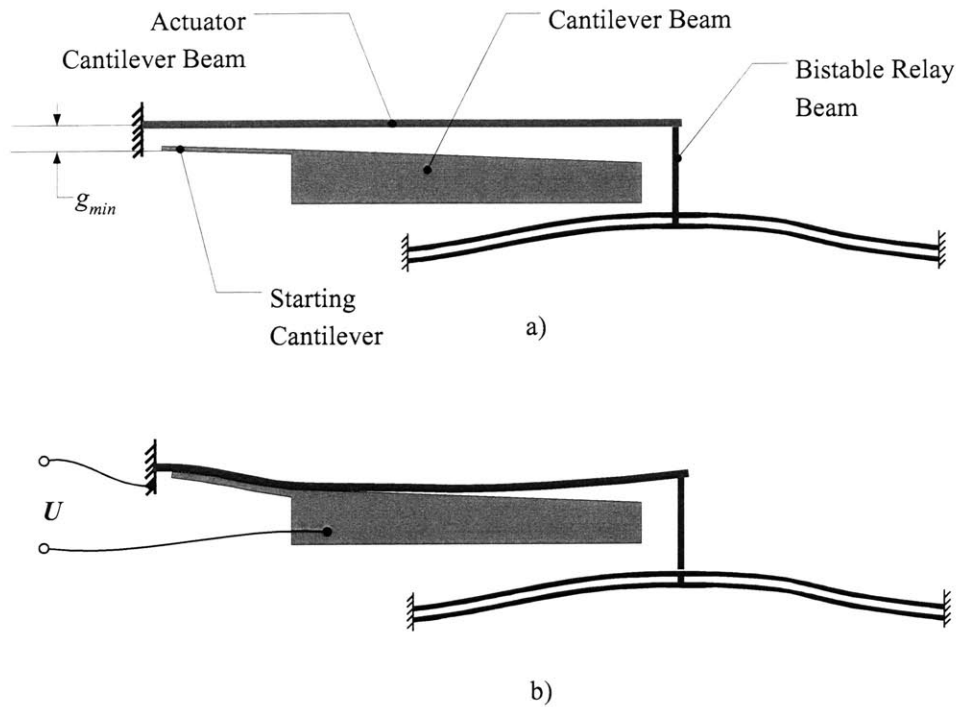
Figure 2-7: compliant starting zone

of $5 \sim 10$ mN. This relay beam is also numerically optimized to achieve the highest contact force by modulating the beam thickness with the position along the length [46] [47]. Figure 2-8a shows the relay beam (11) ready to be actuated by the actuator cantilevers (3 and 7) through a T-bar (6). As shown in Figure 2-8b, the compliant starting cantilevers (2 and 9) are attracted and pulled in to the corresponding actuator cantilevers when electrified. The gap is closed and a very high electric field and force is created. The actuator cantilevers then zip along the fixed electrodes (1 and 10) at the same relatively low voltage to actuate the bistable relay beam through the T-bar as shown in Figure 2-8c. Finally, electrode (5) with its two compliant starting cantilevers (4 and 8) is used to pull the relay beam back to the initial position as shown in Figure 2-8d.
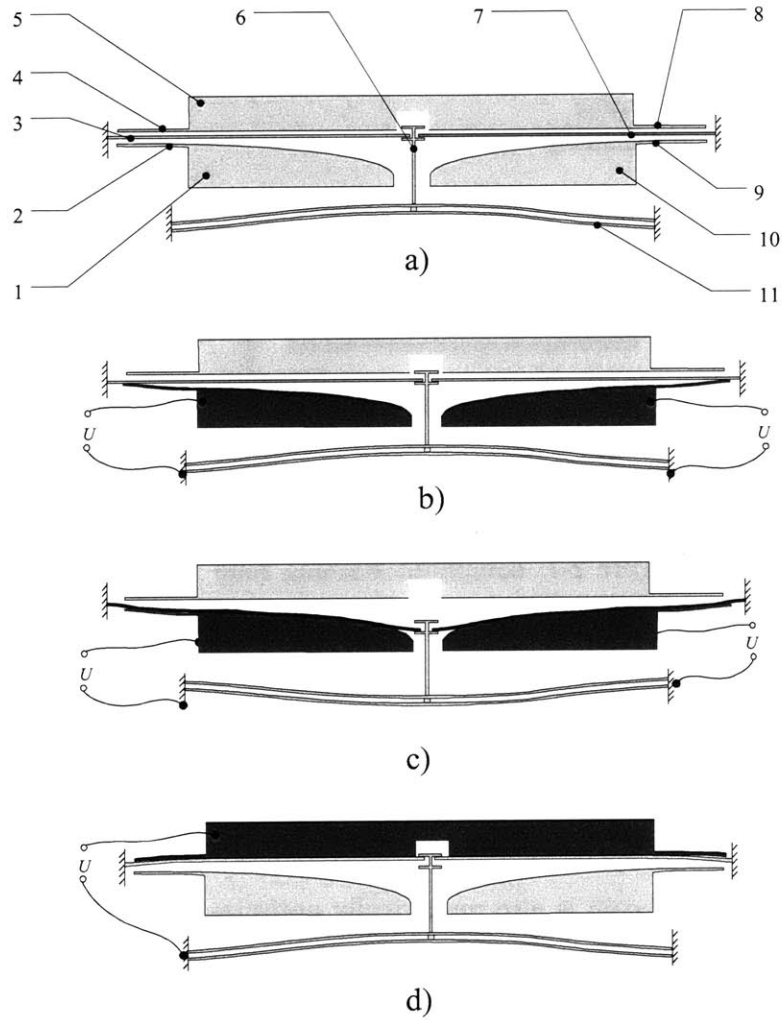
Figure 2-8: schematic view of the actuator at four different voltage excitation states. Figure a) has zero applied voltage. Figure b) has a low applied voltage that bends the starting cantilevers up to close the kerf. Figure c) has a higher voltage that zips the actuator to toggle the relay beam. Figure d) has voltage applied to the upper electrode to return the relay beam to its initial position.
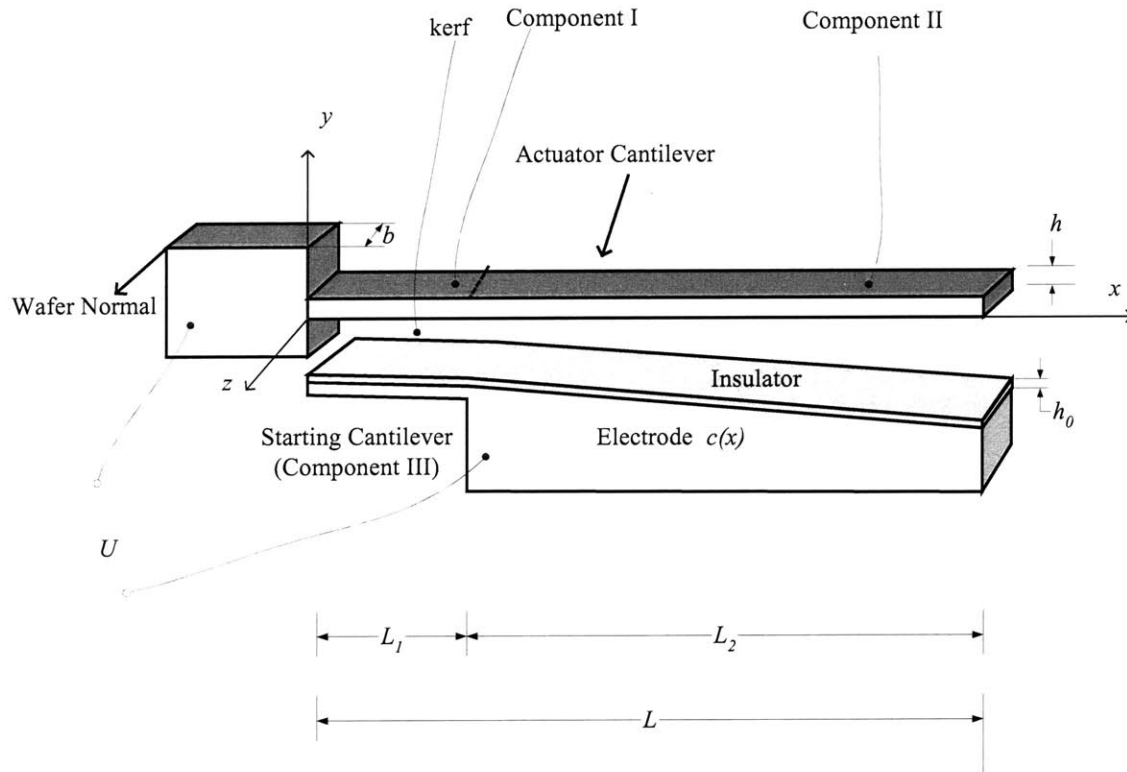
Figure 2-9: actuator model.

2.3   Modeling

In [4], a Rayleigh-Ritz analysis based on total potential energy and small deflection theory is developed to analyze the behavior of zipping actuators. Here, we develop an analytical method using a 2D perturbation method and an alternative numerical analysis. This gives more understanding of the parameters that influence the actuation force and makes the design easier.

2.3.1   Numerical analysis

There are two stages of the operation for zipping actuators: before and after pull-in. These stages are discussed separately below.

41

	Component I	Component II	Component III
Displacement	$y_1(0) = 0$	$y_1(L_1) = y_2(L_1)$, $y_2(L) = 0$	$y_3(L_1) = c(L_1)$
Slope	$y_1'(0) = 0$	$y_1'(L_1) = y_2'(L_1)$	$y_3'(L_1) = c'(L_1)$
Moment	$y_1''(L_1) = y_2''(L_1)$	$y_2''(L) = 0$	$y_3''(0) = 0$
Shear	$y_1'''(L_1) = y_2'''(L_1)$		$y_3'''(0) = 0$

Table 2.2: boundary conditions for the three components. Because components I and II are jointed at point $x = L_1$, the values and the 1st - 3rd order derivatives of y_1 are equal to those of y_2 at L_1. Similarly, since component III is connected to the fixed electrode at $x = L_1$, the value and 1st order derivative of y_3 are equal to those of the electrode function $c(x)$ at $x = L_1$.

Before pull-in

Prior to pull-in, the actuator is modeled as a device with three components as shown in Figure 2-9. The first component is the left part of the actuator cantilever with length L_1 that faces the starting cantilever. The second component is the right part of the actuator cantilever with length L_2 that faces the fixed electrode. The third component is the compliant starting cantilever on the electrode. Each component is modeled as a deformable beam with rectangular cross section. These components deflect due to the electrostatic force when the actuation voltage U is applied across the free-space air gap and insulation layer of relative permittivity ε_r. $y_1(x)$, $y_2(x)$ and $y_3(x)$ are the profile functions of the three components, respectively. Note here, as defined in the coordinate system in Figure 2-9, that $y_1(x)$ and $y_2(x)$ are initially zero and become negative when the beam is deformed by the electrostatic force during actuation. The differential equations for their one-dimensional motions are then

$$
\begin{cases}
E(I_1(x)y_1(x)'')'' = -\dfrac{\varepsilon_0 U^2 b}{2(y_1(x) - y_3(x) + h_0/\varepsilon_r)^2} \\[2mm]
E(I_2(x)y_2(x)'')'' = -\dfrac{\varepsilon_0 U^2 b}{2(y_2(x) - c(x) + h_0/\varepsilon_r)^2} \\[2mm]
E(I_3(x)y_3(x)'')'' = \dfrac{\varepsilon_0 U^2 b}{2(y_1(x) - y_3(x) + h_0/\varepsilon_r)^2}
\end{cases}
\tag{2.8}
$$

where E is the Young's modulus of silicon, $I_1(x)$, $I_2(x)$ and $I_3(x)$ are respectively the moments of inertia of the three components, b is the wafer thickness, $c(x)$ is the

electrode shape function and h_0 is the thickness of the insulation layer. Component *I* is clamped at its left end and connected with Component *II* at its right end. Component *II* is connected with Component *I* at its left end while constrained at its right end. Component *III*, the starting cantilever, is free at its left end while clamped into the fixed electrode at its right end. Accordingly, the boundary conditions before pull-in are as shown in Table 2.2. Although the device can be optimized by varying the thickness of the actuator cantilever [46] [47], in the analysis presented in this thesis, the actuator cantilever and the starting cantilever thicknesses are uniform.

The thicknesses of the three components are h_1, h_2 and h_3; here, let $h_1 = h_2 = h$. The variables are first normalized as

$$\tilde{X} = \frac{x}{L}, \quad \tilde{Y} = \frac{y}{h}, \quad \tilde{C} = \frac{c}{h}, \quad H_0 = \frac{h_0}{h} \tag{2.9}$$

and

$$\begin{cases} \gamma_1 = \frac{6\varepsilon_0 U^2 L^4}{E{h_1}^6} \\ \gamma_1 = \frac{6\varepsilon_0 U^2 L^4}{E{h_2}^6} \\ \gamma_3 = \frac{6\varepsilon_0 U^2 L^4}{E{h_3}^6} \end{cases} \tag{2.10}$$

Then, equation 2.8 can be written as:

$$\begin{cases} \tilde{Y}_1''''(\tilde{X}) = -\frac{\gamma_1}{(\tilde{Y}_1(\tilde{X}) - \tilde{Y}_3(\tilde{X}) + H_0/\varepsilon_r)^2} \\ \tilde{Y}_2''''(\tilde{X}) = -\frac{\gamma_2}{(\tilde{Y}_2(\tilde{X}) - \tilde{C}(\tilde{X}) + H_0/\varepsilon_r)^2} \\ \tilde{Y}_3''''(\tilde{X}) = \frac{\gamma_3}{(\tilde{Y}_1(\tilde{X}) - \tilde{Y}_3(\tilde{X}) + H_0/\varepsilon_r)^2} \end{cases} \tag{2.11}$$

The normalized boundary conditions are shown in Table 2.3. The equations are then solved simultaneously using MATLAB$^{\text{TM}}$. (The code is shown in Appendix A) Actuation forces can be calculated as

$$F_{right} = EI y_2'''(L) \tag{2.12}$$

By increasing the voltage in small steps from zero until the solution diverges, pull-in voltages can also be predicted. For example, consider a silicon actuator cantilever

	Component I	Component II	Component III
Displacement	$\tilde{Y}_1(0) = 0$	$\tilde{Y}_1(L_1/L) = \tilde{Y}_2(L_1/L)$, $\tilde{Y}_2(1) = 0$	$\tilde{Y}_3(L_1/L) = \tilde{C}(L_1/L)$
Slope	$\tilde{Y}_1'(0) = 0$	$\tilde{Y}_1'(L_1/L) = \tilde{Y}_2'(L_1)$	$\tilde{Y}_3'(L_1/L) = C'(L_1/L)$
Moment	$\tilde{Y}_1''(L_1/L) = \tilde{Y}_2''(L_1/L)$	$\tilde{Y}_2''(1) = 0$	$\tilde{Y}_3''(0) = 0$
Shear	$\tilde{Y}_1'''(L_1/L) = \tilde{Y}_2'''(L_1/L)$		$Y_3'''(0) = 0$

Table 2.3: normalized boundary conditions for the three components.

Symbol (units)	Name	Value
E (Pa)	Youn'g modulus	160×10^9
ε_0 (F/m)	Permittivity of free space	8.85×10^{-12}
ε_r	Relative permittivity of S_iO_2	3.8
b (μm)	Wafer depth	300
$L\ (= L_1 + L_2)$ (μm)	Actuator cantilever length	4500
g_{min} (μm)	Minimum gap	10
t (μm)	Minimum beam thickness	10
h (μm)	Actuator cantilever thickness	20
h_3 (μm)	Starting cantilever thickness	20
δ (μm)	Displacement	$0 \sim 80$
δ_{max} (μm)	Maximum displacement	80
h_0 (μm)	Insulation layer thickness	0.4

Table 2.4: dimensions of the actuator.

with parameters listed in Table 2.4, the pull-in voltages are listed in Table 2.5 with respect to the length of starting cantilever. As can be seen, the use of a starting cantilever considerably reduces the pull-in voltage V_{pi} and the function voltage V_{act}.

After pull-in

After the cantilever beam is pulled in to the electrode, the actuator is remodeled as shown in Figure 2-10. Since the electrostatic force is highly nonlinear, there is not a closed-form solution of the actuation force F_{right}. A semi-analytical model based on energy methods was therefore presented in [4]. An admissible trial function of the deflection profile of the actuator cantilever beam shape was first assumed with two

44

Length of Starting Cantilever L_1 (mm)	Pull-in voltage V_{pi} (V)	Relay function voltage V_{act}
2	50	145
1.5	65	145
1	90	145
0.5	145	145
0	245	245

Table 2.5: calculated pull-in and functin voltage versus starting cantilever lengths.

unknowns. By setting the first variations of the total potential energy with respect to the unknowns to be zero, the beam deflection profile was determined and the force is calculated.

A numerical method to calculate the actuation force is developed here. The beam bending equation is first written as:

$$E(I(x)y''(x))'' = -\frac{\varepsilon_0 U^2 b}{2(y(x) - c(x) + h_0/\varepsilon_r)^2} \quad s \le x \le L \qquad (2.13)$$

where $I(x)$ is the moment of inertia and $y(x)$ is the deflection of the actuator cantilever. (Here the actuator cantilever is not considered as two components hence $y_1(x)$ and $y_2(x)$ are not used.) s is the x location of contact departure between the electrode and the actuator cantilever. The right end of the actuator cantilever beam is constrained at position δ and not rotation limited, as is intended for the application of the actuation. Accordingly, the boundary conditions are

$$y(s) = c(s), \; y'(x) = c'(s), \; y''(s) = c''(s), \; y(L) = \delta, \; y''(L) = 0 \qquad (2.14)$$

It is worth noting that, because there is no moment acting on the actuator cantilever at the departure point, the curvature $y''(x)$ at $x = s$ must be continuous and thus equal $c''(s)$.

With Equation 2.9 and

$$\gamma = \frac{6\varepsilon_0 U^2 L^4}{Eh^6} \qquad (2.15)$$
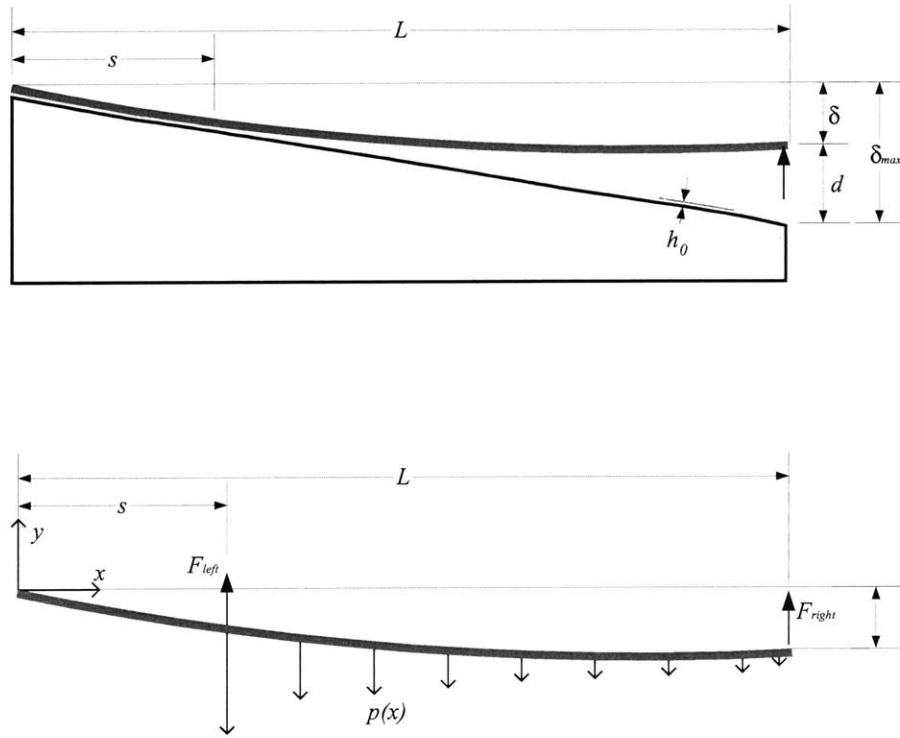
Figure 2-10: model of the actuator cantilever after pull-in.

Equation 2.13 can be first normalized as

$$\tilde{Y}''''(\tilde{X}) = -\frac{\gamma}{(\tilde{Y}(\tilde{X}) - \tilde{C}(\tilde{X}) + \frac{H_0}{\varepsilon_r})^2} \quad S \leq \tilde{X} \leq L \tag{2.16}$$

When voltage increases, the boundary S moves as the actuator beam zips along the fixed electrode. To simplify this situation, Equation 2.16 is further normalized with definition

$$X = \frac{\tilde{X} - S}{1 - S} \quad \lambda = 1 - S \tag{2.17}$$

such that Equation 2.16 is finally normalized as

$$Y''''(X) = -\frac{\gamma\lambda^4}{(Y(X) - C(X) + H_0/\varepsilon_r)^2} \quad 0 \leq X \leq L \tag{2.18}$$

The normalized boundary conditions for Equations 2.16 and 2.18 are shown in Table 2.6. Equation 2.18 is solved numerically using MATLAB$^{\text{TM}}$. (The code is shown in Appendix B.) The actuation force is a function of actuation voltage U,

	Left end		Right end	
	$\tilde{X} = S$	$X = 0$	$\tilde{X} = 1$	$X = 1$
Displacement	$\tilde{Y}(S) = \tilde{C}(S)$	$Y(0) = C(0)$	$\tilde{Y}(1) = 0$	$Y(1) = 0$
Slope	$\tilde{Y}'(S) = \tilde{C}'(S)$	$Y'(0) = C'(0)$		
Moment	$\tilde{Y}''(S) = \tilde{C}''(S)$	$Y''(0) = C''(0)$	$\tilde{Y}''(1) = 0$	$Y''(1) = 0$

Table 2.6: normalized boundary conditions for equations 2.16 and 2.18.

actuator cantilever thickness h, insulator thickness h_0 and tip deflection δ. With the parameters shown in Table 2.4 and a straight electrode, Figure 2-11 shows the actuator cantilever profiles at different displacements with the same actuation voltage $U = 120$ V. As can be seen, the zipped length s increases as the actuator displaces at its right end. Figure 2-12 shows the actuator cantilever profiles at various voltages while the displacement is fixed at $\delta = 0\mu$m. As shown, the zipped length s increases as the actuation voltage is increased.

The actuation force is also calculated using Equation 2.12. With the same dimensions listed in Table 2.4, Figure 2-13 shows the actuation force as a function of voltage for different tip deflections; Figure 2-14 shows the actuation force as a function of voltage for different cantilever thicknesses and Figure 2-15 shows the actuation force as a function of voltage for different insulation layer thicknesses.

2.3.2 Analytical method

As can be seen from the numerical analysis described above, parameters h, h_0, L and δ_{max} must be chosen to properly design an electrostatic zipping actuator. Because of the inherent non-linearity of electrostatic force and the moving contact point, it is time-consuming to compute the actuation force numerically. Additionally, the numerical method does not provide any information about the influence of the parameters. Therefore it is also desirable to develop an analytical method to analyze the force-displacement character of the actuator after pull-in in order to design the actuator more efficiently. To do so, let

$$\bar{y}(x) = y(x) - c(x) \tag{2.19}$$

47
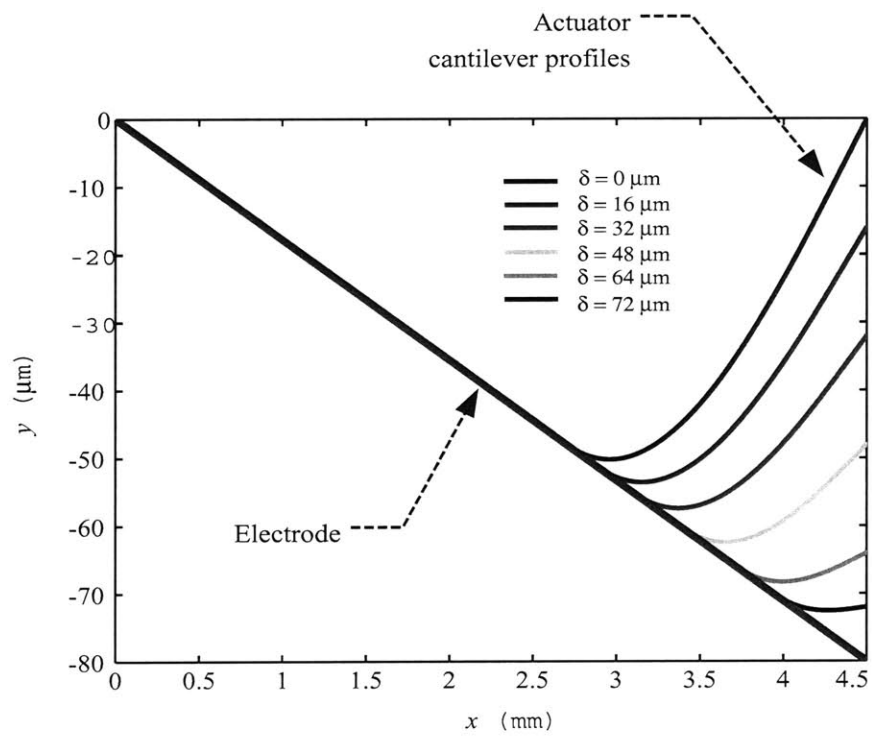
Figure 2-11: actuator cantilever profiles at various displacements. The actuation voltage is $U = 120\ V$.
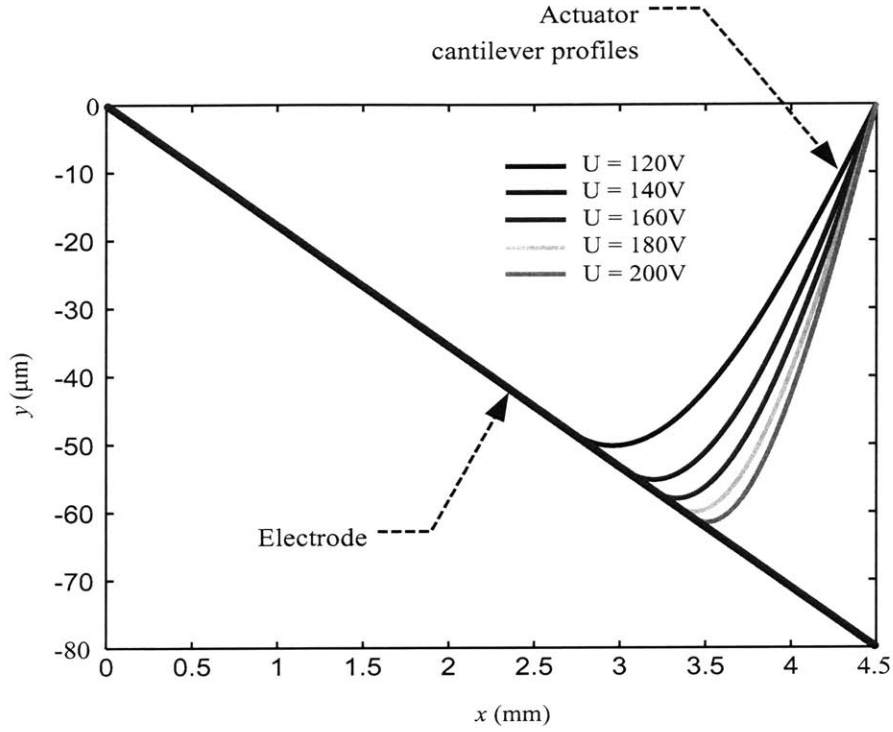
Figure 2-12: actuator cantilever profiles at various actuation voltages. The displacement is fixed at $\delta = 0 \ \mu$m.
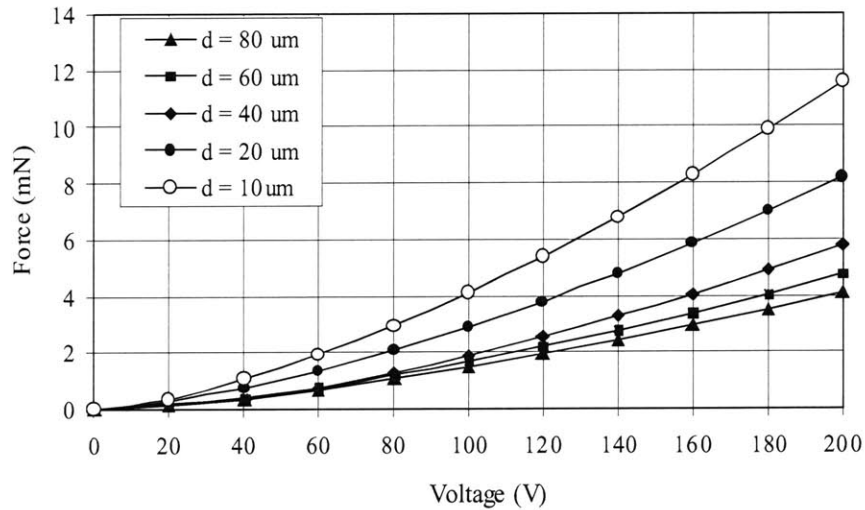
Figure 2-13: theoretical actuator forces as a function of voltage for various tip positions $\delta \ (= \delta_{max} - d)$. The actuator cantilever thickness is $h = 20 \ \mu$m, the oxide insulator thickness is $h_0 = 0.4 \ \mu$m, the maximum tip deflection is $\delta_{max} = 80 \ \mu$m, and the wafer thickness is $b = 300 \ \mu$m.
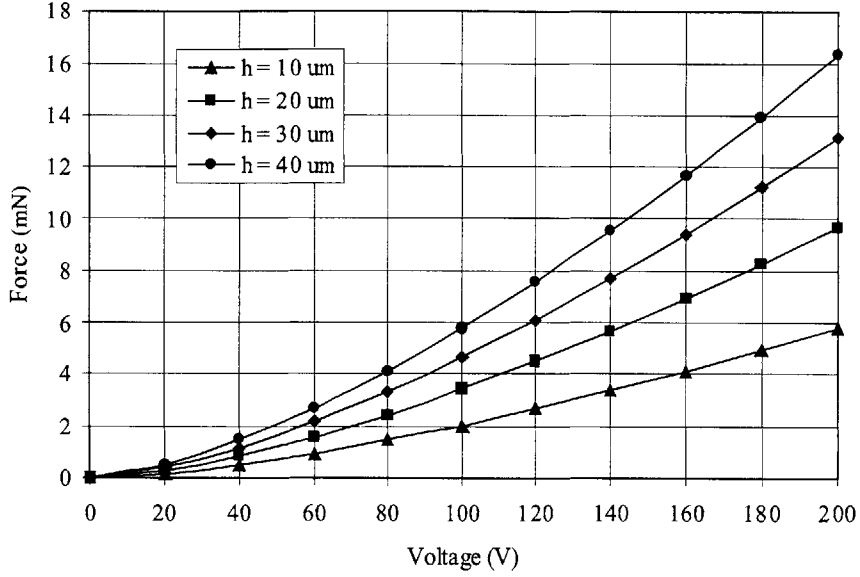
Figure 2-14: theoretical actuator forces as a function of voltages for various actuator thicknesses h. The tip position is $\delta = 0$ μm, the oxide insulator thickness is $h_0 = 0.4$ μm, the maximum tip deflection is $\delta_{max} = 80$ μm and the wafer thickness is $b = 300$ μm.

$$\Gamma = \frac{\varepsilon_0 U^2 b}{2} \tag{2.20}$$

and

$$\beta = \frac{h_0}{\varepsilon_r} \tag{2.21}$$

Next the bending beam Equation 2.13 is rewritten as:

$$EI\bar{y}''''(x) = p(x) = -\frac{\Gamma}{(\bar{y}(x) + \beta)^2} \qquad s \leq x \leq L \tag{2.22}$$

with boundary conditions

$$\bar{y}(s) = 0, \ \bar{y}'(s) = 0, \ \bar{y}''(s) = 0, \ \bar{y}(L) = -\delta, \ \bar{y}''(L) = 0 \tag{2.23}$$
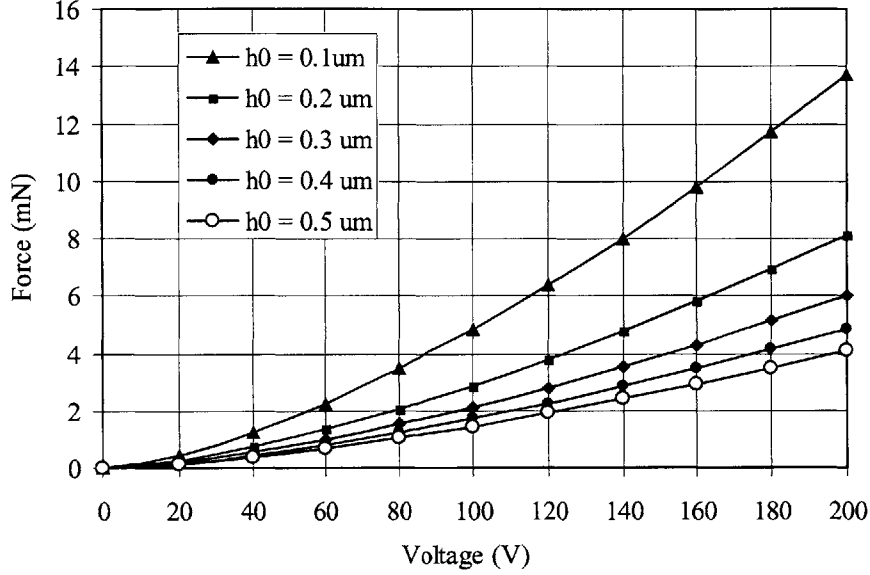
Figure 2-15: theoretical actuator forces as a function of voltages for various insulator thicknesses h_0. The tip position is $\delta = 0$ μm, the actuator cantilever thickness is $h = 20$ μm, the maximum tip deflection is $\delta_{max} = 80$ μm and the wafer thickness is $b = 300$ μm.

To find the actuation force, the force acting on the beam at the left end as shown in Figure 2-10 is

$$F_{left} = \frac{1}{L-s} \int_s^L -p(x)[(L-s)-x]dx = \frac{1}{L-s} \int_0^L \frac{\Gamma[(L-s)-x]}{(\bar{y}(x)+\beta)^2}dx \qquad (2.24)$$

The force acting at the right end of the actuator cantilever, which is also the actuation force, is determined from

$$F_{right} = \frac{1}{L-s} \int_0^L p(x)(x-s)dx = \frac{1}{L-s} \int_0^L \frac{\Gamma(x-s)}{(\bar{y}(x)+\beta)^2}xdx \qquad (2.25)$$

Near $x = s$, applying Equations 2.22 and 2.23 yields

$$\bar{y}(x) = -\frac{\Gamma}{24EI\beta^2}(x-s)^4 + A_1(x-s)^3 \qquad (2.26)$$

51

where A_1 is a parameter to be determined. Taking the third derivative of $\bar{y}(x)$ at $x = 0$ according to Equation 2.26 gives

$$F_{left} = EI\bar{y}'''(x) = 6EIA \tag{2.27}$$

Now, since $\bar{y}(x)$ increases quickly away from the electrode, the integrands are localized near $x = s$. If we denote x^* as

$$\bar{y}(x^*) = \beta \tag{2.28}$$

and substitute Equation 2.28 into Equations 2.24 and 2.25

$$F_{left} \sim \frac{1}{L-s} \int_s^{x^*} \frac{\Gamma}{\beta^2}[(L-s) - x]dx \sim \frac{\Gamma(x^* - s)}{\beta^2} \tag{2.29}$$

$$F_{right} \sim \frac{1}{L-s} \int_s^{x^*} (x - s)dx \sim \frac{\Gamma(x^* - s)^2}{\beta^2(L-s)} \tag{2.30}$$

Here, we have made the approximation/simplification that most of the elctric force acting on the actuator cantilevers occurs over $s \leq x \leq x^*$.

Equations 2.26, 2.29 and 2.30 imply

$$\beta = \bar{y}(x^*) = A_1(x^* - s)^3 - \frac{\Gamma(x^* - s)^4}{24EI\beta^2} \sim \frac{F_{left}(x^* - s)^3}{6EI} \tag{2.31}$$

Putting Equations 2.29 and 2.31 together yields

$$(x^* - s) \sim \left(\frac{EI\beta^3}{\Gamma}\right)^4 \tag{2.32}$$

and the actuation force can be calculated by substituting Equation 2.32 into Equation 2.30

$$F_{right} \sim \frac{1}{L-s}\sqrt{\frac{EI\Gamma}{\beta}} \tag{2.33}$$

Now we have the equation for actuation force except that $(L - s)$ is still unknown. To relate $(L-s)$ to other known parameters, note that far from $x = s$, the electrostatic

force is very small, so that

$$\bar{y}(x) \approx A_2(x - s)^2 \quad x > s \tag{2.34}$$

where A_2 is another parameter to be determined. Therefore the tip deflection is given approximately by

$$d \approx A_2(L - s)^2 \tag{2.35}$$

This has been observed in numerical results as well. Near $x = x^*$, the deflection profile must be continuous so that Equations 2.31, 2.34 and 2.32 imply

$$A_2 \sim \frac{\Gamma}{2EI\beta^2}(x^* - s)^2 \sim \frac{\Gamma}{2EI\beta^2}\sqrt{\frac{EI\beta^3}{\Gamma}} \sim \sqrt{\frac{\Gamma}{EI\beta}} \tag{2.36}$$

Next substitute Equation 2.36 into Equation 2.35 to get $(L - s)$ in terms of known parameters

$$(L - s) \sim \left(\frac{EI\beta}{\Gamma}\right)^{1/4}\sqrt{d} \tag{2.37}$$

Next, substitute 2.37 into 2.33 and get the actuation force

$$F_{right} \sim \frac{1}{\sqrt{d}}(EI)^{1/4}\left(\frac{\Gamma}{\beta}\right)^{3/4} \tag{2.38}$$

From Equations 2.20, 2.21 and the definition of $I = bh^3/12$, the force can be estimated as

$$F_{right} \sim \frac{E^{1/4}b}{\sqrt{d}}\left(\frac{\varepsilon_0\varepsilon_r U^2 h}{h_0}\right)^{3/4} \tag{2.39}$$

Equation 2.39 describes the relation between the force and all design parameters. In order to calculate the force accurately, however, we still need the factor A_3 by which

$$F_{right} \approx A_3\frac{E^{1/4}b}{\sqrt{d}}\left(\frac{\varepsilon_0\varepsilon_r U^2 h}{h_0}\right)^{3/4} \tag{2.40}$$

To obtain it, one actuation force is calculated first using numerical methods described above. Consider parameters listed in Table 2.4, at a gap $d = \delta_{max} = 80$ μm and actuation voltage $U = 200$ V, the actuation force is numerically calculated to be

53
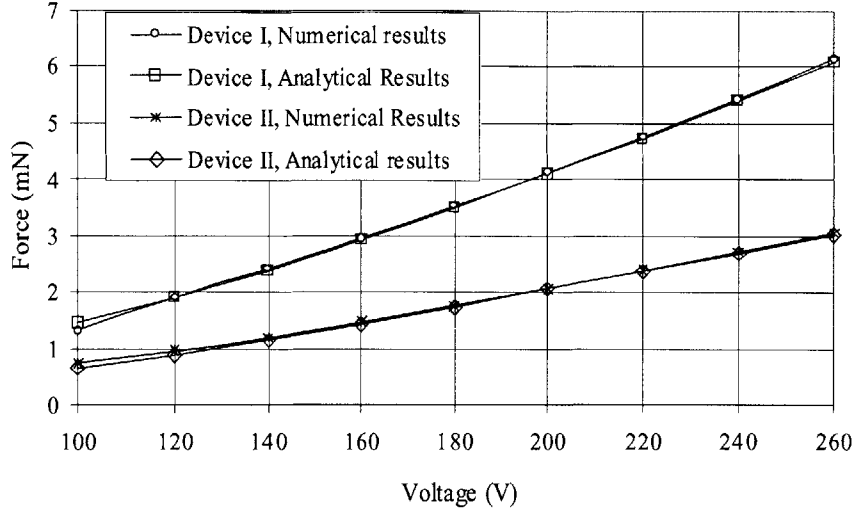
Figure 2-16: theoretical actuator forces versus voltages for two devices using numerical/analytical methods. The parameters for device I are: $h = 20$ μm, $h_0 = 0.5$ μm and $\delta = 0$ μm, while the parameters for device II are $h = 10$ μm, $h_0 = 1$ μm and $\delta = 40$ μm. For both devices, $b = 300$ μm and $\delta_{max} = 80$ μm.

$F_{right} = 4.84$ mN. A_3 is then calculated by substituting the actuation force and the parameters into Equation 2.40 to obtain

$$A_3 \approx 0.307 \tag{2.41}$$

Putting A_3 into Equation 2.40 yields

$$F_{right} \approx 0.307 \frac{E^{1/4}b}{\sqrt{d}}(\frac{\varepsilon_0\varepsilon_r U^2 h}{h_0})^{3/4} \tag{2.42}$$

Note here that all the parameters in Equation 2.42 are in International Units (SI).

In order to compare the results from the numerical method and from Equation 2.42, actuation forces for two different actuators have been calculated using numerical and analytical analyses, respectively. The forces are plotted with respect to actuation voltage as shown in Figure 2-16. It can be seen that the two methods agree with each other very well.

54

2.3.3 Actuation force

With Equation 2.42, it is now possible to discuss the influences of each parameter on the actuation force and design the actuator efficiently.

Young's modulus E

$$F_{right} \sim E^{1/4}$$

The Young's modulus is determined by the materials of the cantilever beam. In this thesis, the actuator is built in bulk silicon. For general design, using a material with larger Young's modulus would increase the actuation force only slightly.

Device width b

$$F_{right} \sim b$$

The actuation force is proportional to the device width, which is also the wafer depth in this thesis. However, the minimum gap is also proportional to b and hence the pull-in voltage increases with increasing the wafer depth. Moreover, the DRIE etch cost is proportional to the wafer depth. In this thesis, a 300-μm thick wafer is chosen based on these considerations.

Actuation voltage U

$$F_{right} \sim U^{3/2}$$

Although the electrostatic pressure is proportional to U^2, the actuation force here is proportional to $U^{3/2}$. This is because the unzipped length decreases with increasing voltage and therefore the total force diminishes.

Insulator thickness h_0

$$F \sim h_0^{-3/4}$$

From this relation, the thinner the insulator, the higher the actuation force. However, the highest acceptable actuation voltage U is also constrained by the insulator

thickness h_0. The breakdown voltage is determined by:

$$U_{breakdown} = R_{breakdown} h_0 \tag{2.43}$$

where $R_{breakdown}$ is the dielectric strength of the insulator material. For thermal oxide, this ratio is [48] $R_{breakdown,oxide} = 1 \times 10^7 \ V/cm$. Substituting Equation 2.43 yields

$$F \sim R_{breakdown}{}^{3/4} U^{3/4} = R_{breakdown}{}^{3/2} h_0^{3/4} \tag{2.44}$$

Equation 2.44 implies that, applying the highest acceptable actuation voltage, the actuation force increases with increasing the insulator thickness.

In this thesis, however, the highest voltage is constrained to be $U_{max} = 200V$ and the oxide insulation layer is chosen to be

$$h_0 = \frac{U_{max}}{R_{breakdown,oxide}} \times 2 = 0.4 \ \mu m \tag{2.45}$$

where 2 is the safety factor. Because the oxide is grown on both sides of the actuator, 0.2 μm of oxide is needed to achieve the $0.4\mu m$ of insulation layer. The process time for growing 0.2 μm of oxide is approximately 4 hours, including the time taken to ramp up/down the oven temperature.

Actuator cantilever thickness h

$F \sim h^{3/4}$

Increasing actuator cantilever thickness would increase the actuation force. However, the pull-in voltage would also increase substantially. In this thesis, the pull-in voltage is found using the numerical method in Section 2.3.1. An analytical method for calculating pull-in voltage without the starting cantilever is given in [49]. Optimization of the cantilever thickness can be done using that method and Equation 2.42.

Insulator relative permittivity ε_r

$$F \sim \varepsilon_r \tag{2.46}$$

	ε_r	$R_{breakdown}(V/cm)$
LPCVD Silicon nitride	7.8 ~ 7.9	1×10^9
PECVD Silicon nitride	7.8 ~ 7.9	1×10^8
Silicon oxide	3.8	1×10^9

Table 2.7: relative permittivity and breakdown voltage/thickness ratio of different materials.

Using an insulator with a higher relative permittivity would result in higher actuation force. On the other hand, the dielectric strength $R_{breakdown}$ varies with different materials. Equations 2.46 and 2.44 lead to

$$F \sim \varepsilon_r R_{breakdown}^{3/4} U^{3/4} \tag{2.47}$$

Therefore, at a certain actuation voltage, the actuation force can be increased by choosing a material with higher value of $\varepsilon_r R_{breakdown}^{3/4}$. Table 2.7 lists the properties of different materials. It can be concluded that LPCVD silicon nitride insulation layer would result in the highest actuation force. In this thesis, however, because a silicon wafer after DRIE may not go into the tube to deposit nitride, oxide is chosen.

Gap distance d

$$F \sim d^{-1/2}$$

The actuation force becomes higher as the actuator approches the electrode. When designing the actuaor, the initial gap distance should be as small as possible, in order to get the highest actuation force. In this thesis, the required stroke of the actuator is 80 μm and thus the initial gap is designed to be 85 μm to accomodate the fabrication variation.

2.3.4   Optimization of the relay beam

The bistable switch beam, (11) in Figure 1-1, was developed by Qiu et al [23]. The mechanism consists of two parallel cosine-curved clamped-clamped beams that are also clamped together at their centers. An FEA model of the mechanism is shown

in Figure 2-20a. The bistability does not rely on internal stress or hinges hence it is suitable for microfabrication. Analytical methods have been developed to calculate the force-displacement character of the mechanism. The analysis indicates that the force-displacement characteristic is not symmetric for beams with uniform thickness. Therefore the ratio of the push and pull forces is approximately 2:1 as shown by FEA force-displacement curve in Figure 2-21. If the bistable structure is used as a switch beam, as shown in Figure 2-8, the actuation force to close the relay (7.5 mN) is more than two times the contact force (2.8 mN). Because the relay contact resistance becomes lower as the contact force increases, a goal of the design is to generate the highest contact force for a given actuation force. Alternatively, it is desired to reduce the actuation force for a required contact force. This leads to an optimization of the push/pull force ratio of the bistable structure [47] [46].

The optimization focuses on the unstable transition state connecting the two stable equilibrium states. It is shown that, although the force displacement characteristics of the switch are highly nonlinear, the properties of this transition state depend only on the linear modes of the structures comprising the switch. Therefore the optimization reduces to a linear problem. It is first found that the push/pull force ratio of the relay beam is given by [47]

$$R_{push/pull} \approx 1 - \frac{1}{1 - (\tau_2/\tau_0)^2} \tag{2.48}$$

where τ_2 and τ_0 are the two free eigenvalues for the relay beam bending equation

$$E(I(x)y''(x))'' + Ty''(x) = 0 \tag{2.49}$$

where $T = \tau^2$ is the axial compression force, $I(x)$ is the moment of inertia and $y(x)$ is the profile of the relay beam.

It can be derived from Equation 2.48 that

$$R_{push/pull} \approx \frac{1}{1 - (\tau_0/\tau_2)^2} \tag{2.50}$$

The force ration $R_{push/pull}$ is now by reducing the cost function $C_R = \tau_0/\tau_2$. To do so, the variation of the cost function is first written as

$$\delta C_R = \frac{\delta \tau_0}{\tau_2} - \frac{\tau_0}{(\tau_2)^2}\delta \tau_2 \qquad (2.51)$$

It is therefore possible to minimize the cost function by setting δC_R to be negative and iterate the process, until reaching a satisfactory value of $R_{push/pull}$. This can be done by modifying the variations of the eigenvalues $\delta \tau_i$. To obtain the variations $\delta \tau_0$ and $\delta \tau_2$, Equation 2.49 is first modified as

$$(EI(x)\delta y_i'')'' + T_i^2 \delta y_i'' = -\delta T_i y_i'' - (E\delta I y_i'')'' \qquad (2.52)$$

where y_i and δy_i represent the ith eigenfunction and its variation, and T_i and δT_i represent the ith eigenvalue and its variation. According to the Fredholm alternative [50], the right side of Equation 2.52 must be orthogonal to any "null solution" of the left side of Equation 2.51, therefore

$$\int (\delta T_i y_i'' + (E\delta I y_i'')'')y_i'' dx = 0 \qquad (2.53)$$

Equation 2.53 yields

$$\delta T_i = \frac{\int (E\delta I y_i'')'' y_i dx}{\int \delta y_i'' y_i dx} \qquad (2.54)$$

Integrating Equation 2.54 by part generates

$$\delta T_i = E\frac{\int \delta I (y_i'')^2 dx}{\int (y_i')^2 dx} \qquad (2.55)$$

Next, sustituting Equation 2.55 into Equation 2.51

$$\delta C = E \int \delta I [\frac{1}{\tau_2}\frac{(y_0'')^2}{\int (y_0')^2 dx} - \frac{\tau_0}{\tau_2^2}\frac{(y_2''^2)}{\int y_2'^2 dx}]dx = E\int \Lambda(\tau_0, \tau_2, y_0, y_2)dx \qquad (2.56)$$

Therefore, δC_R can be set to be negative by setting the integrand $\Lambda(\tau_0, \tau_2, y_0, y_2)$ to be negative.
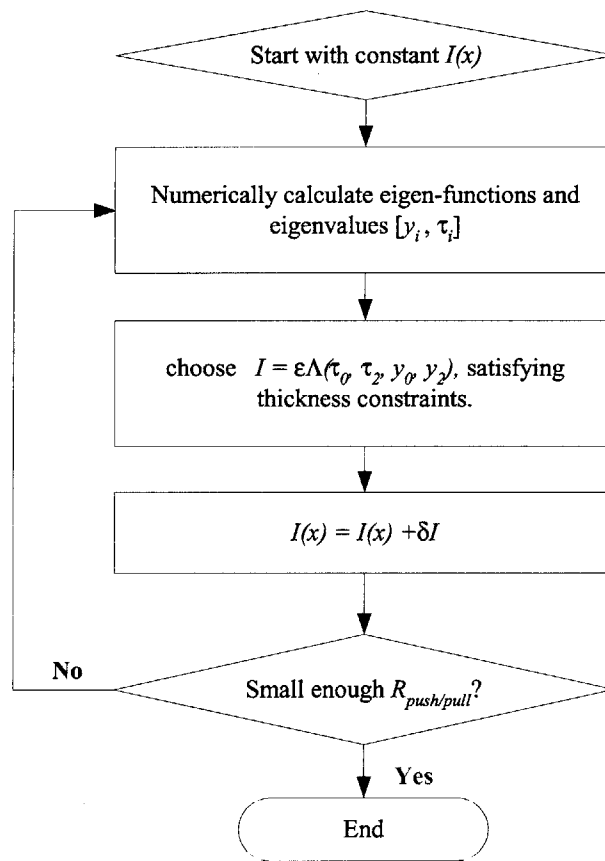
Figure 2-17: relay beam optimization flow chart.
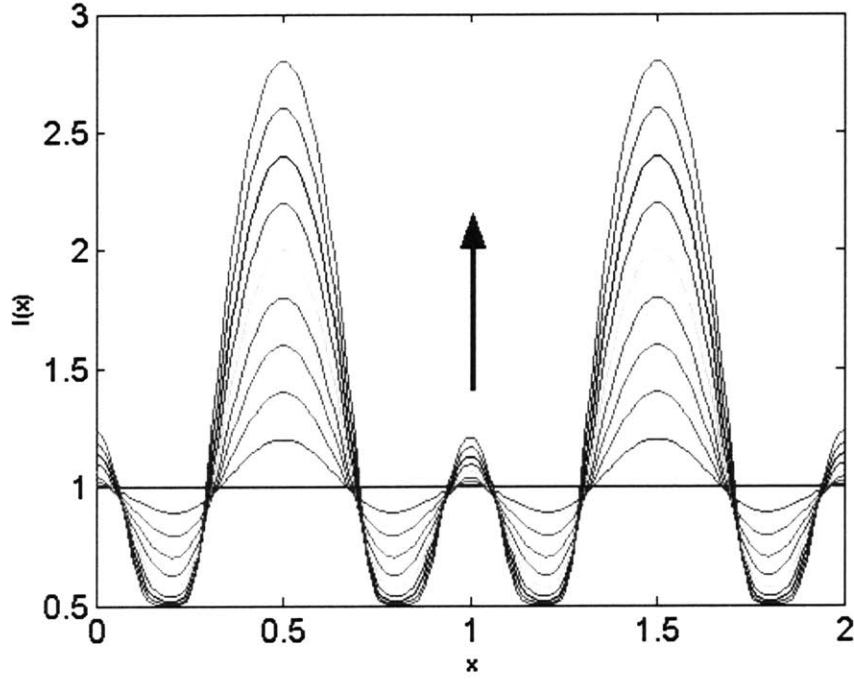
Figure 2-18: variation in the moment of inertia $I(x)$ of the relay beam with iteration number. The arrow indicates the direction of optimization.

Figure 2-17 shows the flow chart of the optimization process and the MATLAB code is presented in Appendix C. It starts with a relay beam having uniform thickness $I(x) = I_0$. The eigenfunctions and eigenvalues $[y_i, \tau_i]$ are then calculated numerically in MATLAB and the integrand $\Lambda(\tau_0, \tau_2, y_0, y_2)$ is caculated. Next the variation of moment of inertia is set to be

$$\delta I = \epsilon \Lambda(\tau_0, \tau_2, y_0, y_2) \tag{2.57}$$

where ϵ is a small negative number to keep the beam thickness larger than or equal to the minimum allowable value in fabrication. The moment of inertia of the relay beam is then modified to be

$$I(x) = I(x) + \delta I \tag{2.58}$$

Now the force ratio $R_{push/pull}$ is slightly less than the initial value. By iterating the process as shown in Figure 2-17 until the minimum allowable thickness is reached, the force ratio can be optimized. Figure 2-18 shows the variation in the moment of

61
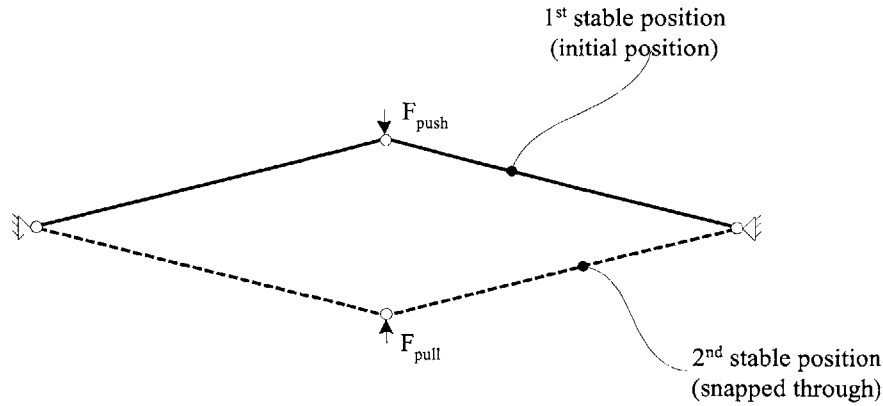
Figure 2-19: a bistable mechanism with hinges

inertia $I(x)$ of the beam with iteration number. The arrow indicates the direction of optimization. By using the optimzed shape as shown in the outside profile shown in Figure 2-18, the force ratio is reduced from 2.5:1 to 1.5:1.

The thin-thick-thin-thick-thin profile of the switch beam recalls the configuration as shown in Figure 2-19, which has two bars hinged to the wall and are hinged together in the middle. The symmetry of the structure at the two stable positions yields symmetric force-displacement curve, i.e., the push/pull force ration is 1:1. However, it is very difficult to implement a perfect hinge for MEMS fabrication. As can be seen from Figure 2-18, the profile approaches the configuration shown in Figure 2-19 when iteration number increases.

2.3.5   Finite element analysis

To analyze the force-displacement characteristic of the relay beam, a 2-D model is developed using the Algor^{TM} finite element analysis package. The relay beam shapes are shown in Figure 2-20. Figure 2-20a shows the relay beam with uniform thickness and Figure 2-20b shows the beam with varying thickness optimized using numerical methods described in Section 2.3.4. The force-displacement curves of the two relay beams analyzed by FEA are shown in Figure 2-21. As can be seen, both of the relay beams realize 2.8 mN of contact force. However, to actuate the relay beam, 7.2 mN peak force is needed for the uniformly thick beam while only 4.5 mN is needed for
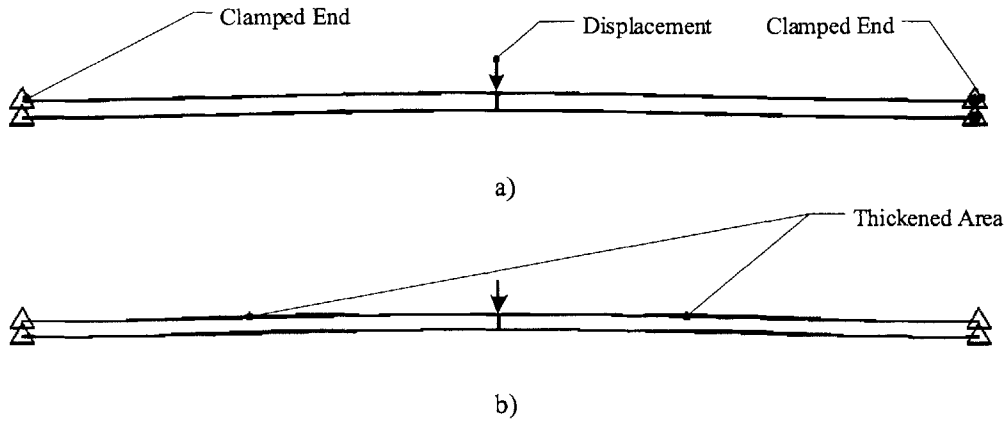
Figure 2-20: FEA model of the relay beam with uniform thickness a) and optimized shape b).

the optimized beam. With the optimization, the force required from the actuator has been reduced by 33%.

2.3.6 Dynamic analysis

As a rule of thumb, to safely fabricate the device, its lowest mechanical resonant frequency should be above 1 kHz. The moving components in the relay are the relay beam and the free standing cantilevers, the relay beam is constrained at both ends and is much stiffer than the two cantilevers. Therefore either the actuator cantilever or the starting cantilever has the lowest resonant frequency. The actuator cantilever is clamped at its left end and free at its right end. But the T-bar at its right end constrains its movement in a range of 20 μm. Hence it is appropriate to model the actuator cantilever as constrained at its right end as shown in Figure 2-22a. Then the 1st-mode resonant frequency of the actuator cantilever beam is calculated as [51]

$$f_1 = \frac{1}{2\pi} \frac{3.92^2}{L_1^2} \sqrt{\frac{EI}{\rho b h_1}} = \frac{2.44 h_1}{L_1^2} \sqrt{\frac{E}{12\rho}} \tag{2.59}$$

63
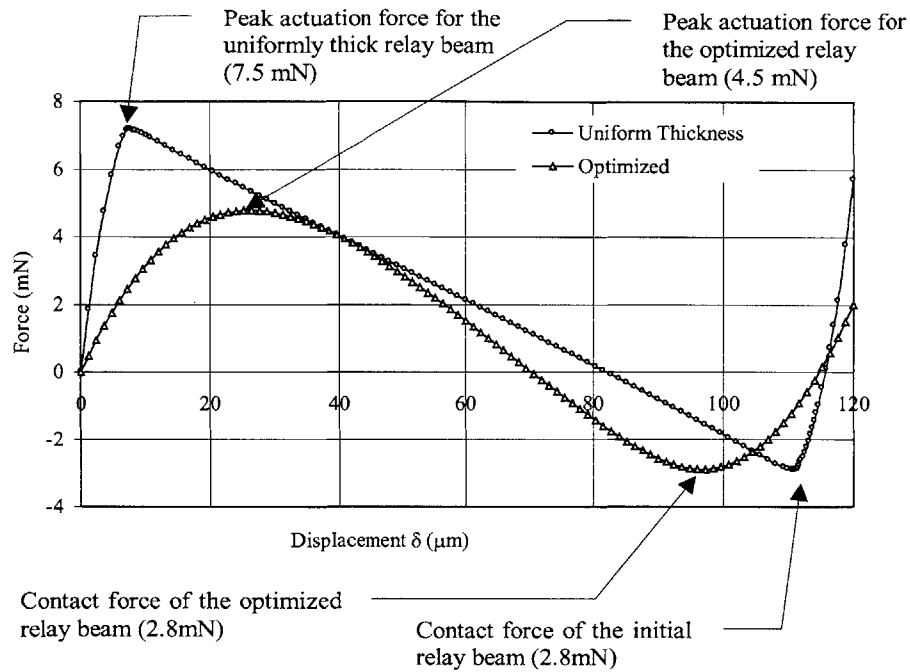
Figure 2-21: force-displacement FEA results for relay beam with uniform and varying (optimized) thickness. The two relay beams have the same contact force of about 3 mN but the actuation force of the optimized beam (4.5 mN) is only approximately 60% of that of the uniformly thick beam (7.5 mN).
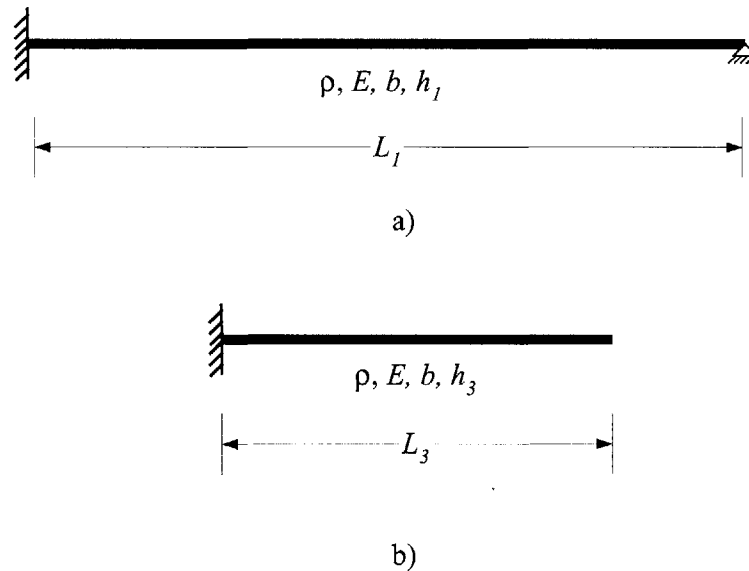
Figure 2-22: dynamic model of the actuator cantilever beam a) and the starting cantilever b.

where ρ is the density of silicon. As an example, we take $\rho = 2.33 \times 10^3 \ kg/m^3$ and substitute the design parameters listed in Table 2.8 into Equation 2.60 to obtain

$$f_1 = 5.73kHz \tag{2.60}$$

Through 2.60, assuming the same parameters, we can also calculate the smallest allowable thickness of the actuator cantilever is

$$h_{1,smallest} = \frac{1 \times 10^3 (Hz) L_1^{\ 2}}{2.44} \sqrt{12\rho E} = 3.46\mu m \tag{2.61}$$

The starting cantilever beam is modeled as shown in Figure 2-22b and the 1st-mode resonant frequency is calculated by

$$f_1 = \frac{1}{2\pi} \frac{1.88^2}{L_1^2} \sqrt{\frac{EI}{\rho b h_1}} \tag{2.62}$$

Substituting parameters in Table 2.8 into Equation 2.62 yields

$$f_1 = 11.74kHz \tag{2.63}$$

The resonant frequencies of the cantilevers are above 1 kHz and therefore the system is safe in fabrication.

2.4   Design of the complete device

With the analyses described in Section 2.3, it is now possible to design the full relay system. A switch beam is first designed and optimized according to functional requirements listed in Table 1.2. The switch beam force-displacement data are generated using finite element analysis. To design the actuators, the stroke is first determined by the character of the switch beam. Numerical analysis and Equation 2.39 are both used to calculate the pull-in voltage and the actuation force-displacement data for different design parameters such as beam thickness, insulation layer thickness and

65

Parameters (units)	Name	Value
U(volts)	Actuation voltage	140
ε_0 (F/m)	Permittivity of free space	8.85×10^{-12}
ε_r	Relative permittivity of S_iO_2	3.8
$b(\mu\text{m})$	Wafer depth	300
$L(\mu\text{m})$	Device length	4500
$L_1(\mu\text{m})$	Starting cantilever length	1500
$L_2(\mu\text{m})$	Electrode length	3000
g_{min} (μm)	Minimum gap	10
h_1 (μm)	Actuator beam thickness	20
δ_{max} (μm)	Maximum displacement	80
h_0 (μm)	Insulation layer thickness	0.4

Table 2.8: design parameters of the complete device.

beam length. The parameters are also constrained by fabrication capabilities. Finally matching the force-displacement curves of the switch beam and the actuators leads to a balanced design.

One design is shown in Figure 2-24, the contact force of the switch beam is 2.8 mN and the actuation force is optimized to be 4.5 mN. The stroke of the switch beam is determined to be 120 μm. The FEA results of the switch beam then indicate a transient position at 80 μm at which the required actuation force is zero. This implies a smallest stroke of 80 μm for the actuator. Since both the pull-in voltage and the force increases as actuator cantilever thickness increases, the actuator cantilever thickness is designed to be 20 μm. The starting cantilever is designed so that the pull-in voltage is less than an actuation voltage of 200 V, and the insulation layer thickness is determined to be 0.4 μm. The force-displacement curves of the actuator are plotted in Figure 2-24 at various voltages. As can be seen, the function voltage V_{act} is approximately 140 V. The final design parameters for the actuator are listed in Table 2.8.

```
                    ┌─────────────────────────────┐
                    │     Design requirements     │
                    └─────────────────────────────┘
                                  │
                                  ▼
                    ┌─────────────────────────────┐
                    │         Relay beam          │
                    └─────────────────────────────┘
                                  │
                                  ▼
                ┌─────────────────────────────────────┐
                │  Optimization of switch beam (minimum│
                │  thickness > 10 μm), F-D curve using FEA│
                └─────────────────────────────────────┘
                                  │
                                  ▼
                ┌─────────────────────────────────────┐
                │       Zipping actuator stroke       │
                └─────────────────────────────────────┘
                                  │
                                  ▼
        ┌─────────────────────────────────────────────────────┐
        │ Zipping actuator cantilever length (<5 mm)/thickness (>10 μm),│
        │ insulation layer thickness, starting cantilever thickness (>10 μm)/│
        │                        length.                      │
        └─────────────────────────────────────────────────────┘
                                  │
                                  ▼
                            ╱─────────────╲
                    N      ╱ Pull-in voltage ╲
            ◄───────────── ╲   < 200 V?     ╱
                            ╲─────────────╱
                                  │ Y
                                  ▼
                            ╱─────────────╲
                           ╱Working voltage ╲        N
                           ╲  < 200 V?      ╱ ──────────►
                           ╲(Enough force?)╱
                            ╲─────────────╱
                                  │ Y
                                  ▼
                    ┌─────────────────────────────┐
                    │             End             │
                    └─────────────────────────────┘
```
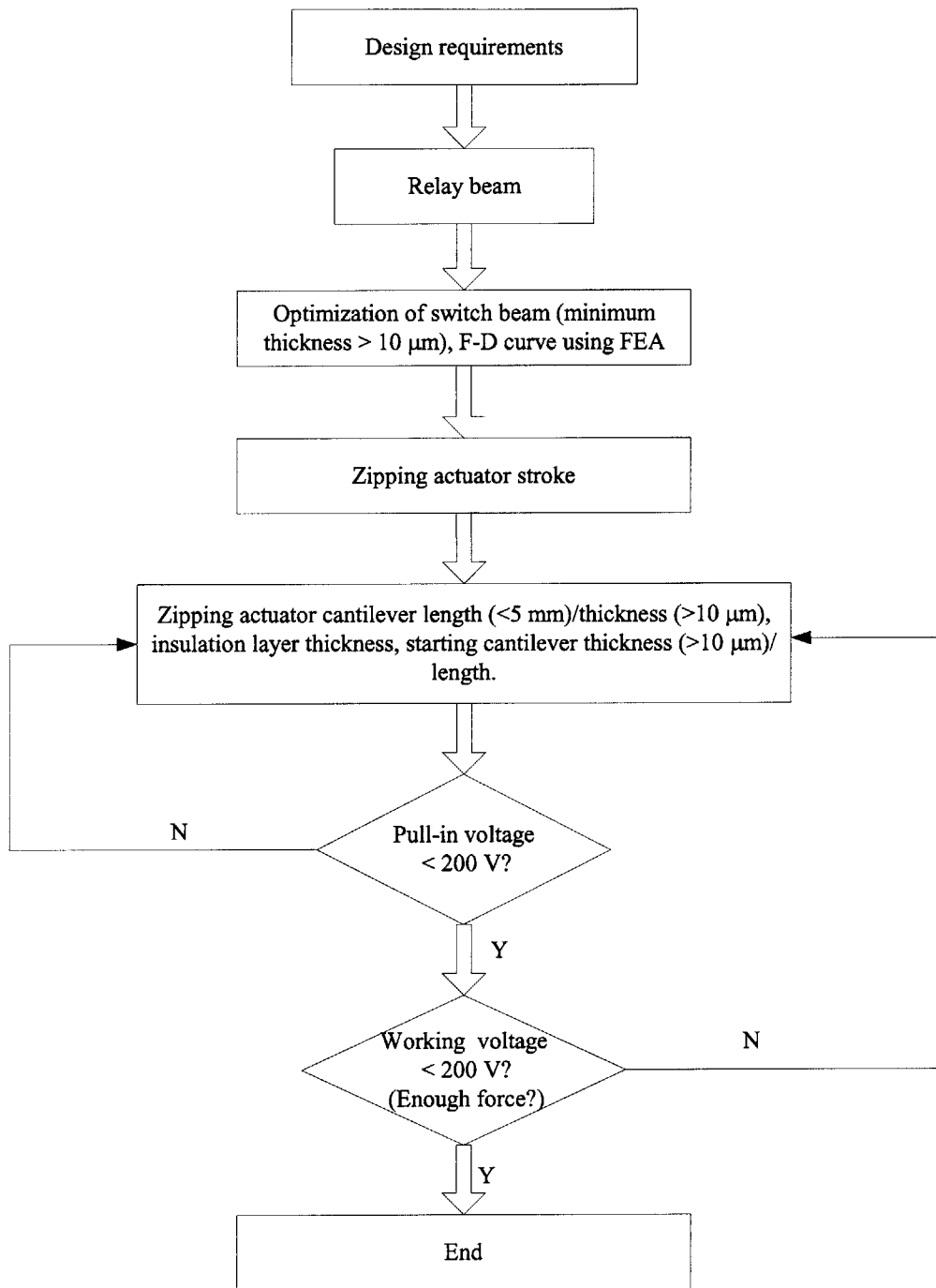
Figure 2-23: device design flow chart.
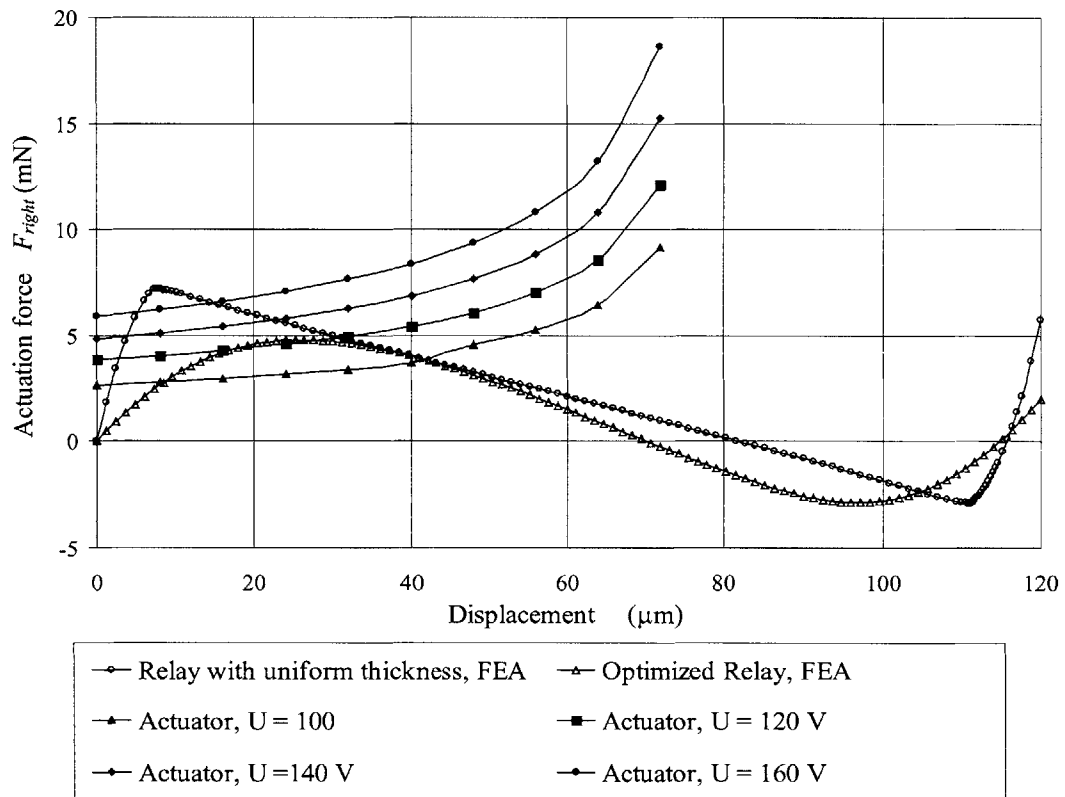
Figure 2-24: force-displacement FEA results for relay beam and actuators at various voltages. An actuation voltage of $U \approx 130$ V is needed to toggle the switch as implied from the curves.

Chapter 3

Fabrication and Measurement

To test the actuators and finally build the MEMS relays for power applications, a device consisting of a relay beam and two zipping actuators is fabricated in a 4" $\langle 100 \rangle$ silicon wafer as shown in Figure 2-8. This chapter describes the fabrication and measurement of this device. Section 3.1 addresses the fabrication process for the device that is carried out at MIT in the Microsystems Technology Laboratory (MTL). Section 3.2 then presents the fabrication results. Finally, measurement results are shown in Section 3.3 and compared to the theoretical predictions presented in Chapter 2.

3.1   Process flow

The fabrication process for the device involves three wafers. The device is first built in a silicon wafer using a DRIE through etch. To selectively remove the insulation layer on top of the device wafer, another silicon shadow wafer is etched using DRIE. The third wafer is a Pyrex 7740 wafer that is bonded to the device wafer as a handle. The fabrication processes for the three wafers are discussed respectively as follows.

69
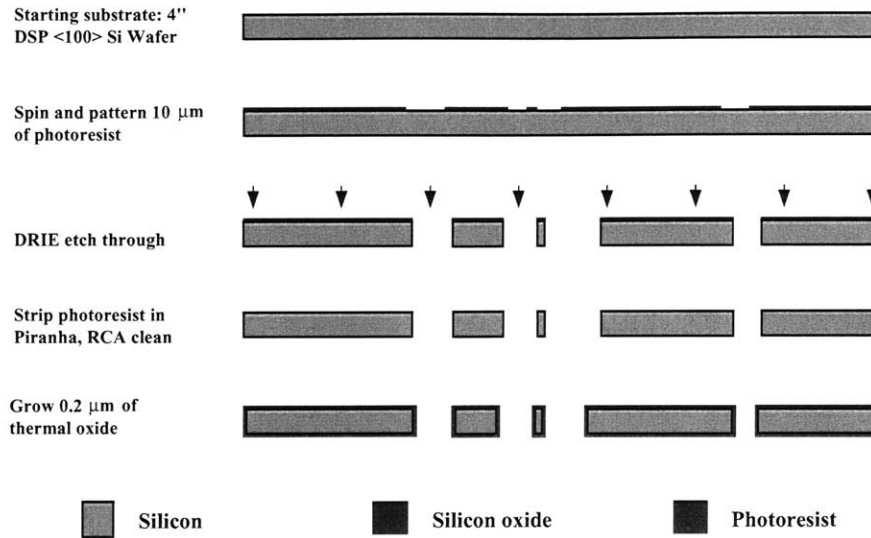
Figure 3-1: device wafer process.

3.1.1 Device wafer

As shown in Figure 3-1, the device wafer starts as a 4-inch double-side-polished low-resistivity ($0.008 \sim 0.015$ Ωcm) $\langle 100 \rangle$ n-type silicon wafer with a thickness of 300 μm. The wafer is first coated with approximately 10 μm of AZ4620 thick photoresist that is later exposed by a chrome mask for 12 s. After developing the photoresist in AZ440 for approximately 2 min, the wafer is temporarily mounted to a quartz handle wafer using photoresist. Next, DRIE is used to etch through the silicon wafer using an STS ICP etcher loacated in the Technology Research Laboratory (TRL) in the MTL. The recipe $"MIT39A"$ developed in the MTL was used due to its experimentally proven capablity of generating straight cross section beam profiles, which is desirable for the electrostatic actuator. The total time taken to etch through 300 μm is approximately 150 min. The silicon wafer is then cleaned in Piranha and separated from the quartz wafer. Next, after an RCA cleaning process, a 200-nm layer of oxide is grown on the device wafer by wet oxidation at 1000 °C using Tube A2 in TRL. This oxide layer is grown on both the surfaces and sidewalls, and provides a 400 nm electrical insulation layer between the actuator cantilever and the curved electrode and starting cantilever. The masks are shown in Appendix D.

To make the etch mask, transparency masks are used because they are very in-

70
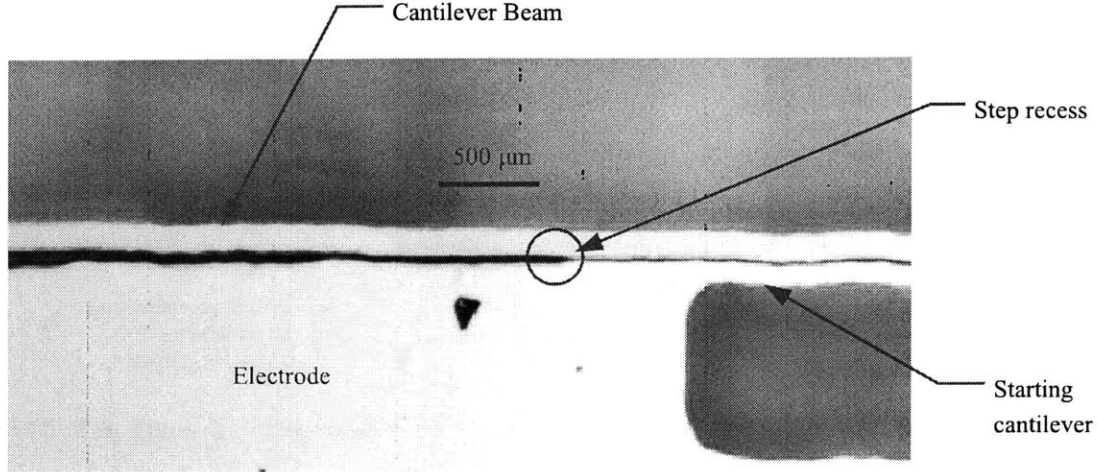
Figure 3-2: microscope photograph of the device made directly by transparency mask.

expensive and have quick turnaround, compared to conventional masks. To make a transparency mask, the device pattern is first printed on a transparency film that has a resolution of $\sim 5\ \mu$m. Next, the transparency film is used to expose a chrome mask that can be used later to pattern the device wafer. However, transparency masks can only be used for non-critical features due to their low resolution. Figure 3-2 shows the microscopic view of one device made directly by transparency mask. As the actuator cantilever zips along the electrode, the step recess on the electrode caused by low-resolution printing results in a large gap distance between two electrodes. Hence the electrostatic force is reduced significantly and the cantilever stops zipping.

In this thesis, in order to achieve higher resolution photolithography while taking advantage of the low-cost and quick-turnaround transparency masks, a process is developed as shown in Figure 3-3. The device features are first magnified 10 times and printed on a transparency film. The transparency film is next used to expose a chrome mask plate. Finally, the chrome mask is used in a 10:1 reduction stepper (SVG8800) to photolithographically pattern a resist mask on the silicon wafer. Figure 3-4 shows a device made by transparency mask and stepper. Apparently the roughness is much smaller than as shown in Figure 3-2. As a result, the actuator cantilever zips along the electrode smoothly when testing, as will be discussed in Section 3.3.

The $10\times$ transparency mask is shown in Appendix D. In order to achieve uniform

Print 10x MEMS feature on transparency film.

Expose 5" chrome mask.

Pattern photoresist on 4" wafer using 10:1 reduction stepper.
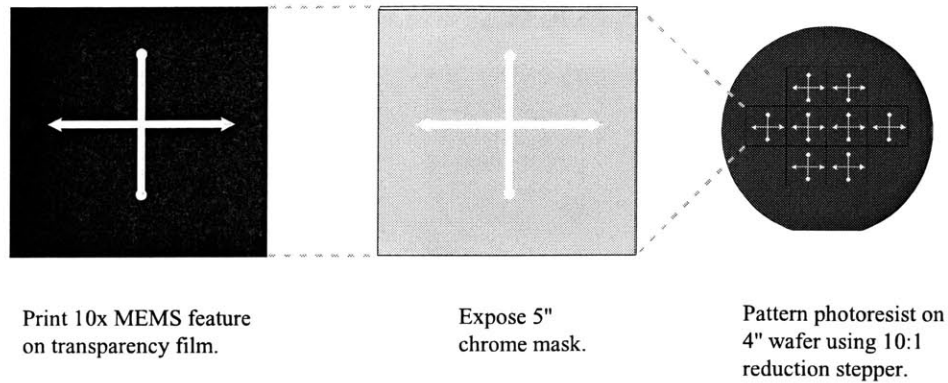
Figure 3-3: the process for making devices using $10\times$ transparency mask and 10:1 reduction stepper.

Cantilever Beam

Electrode

Starting cantilever
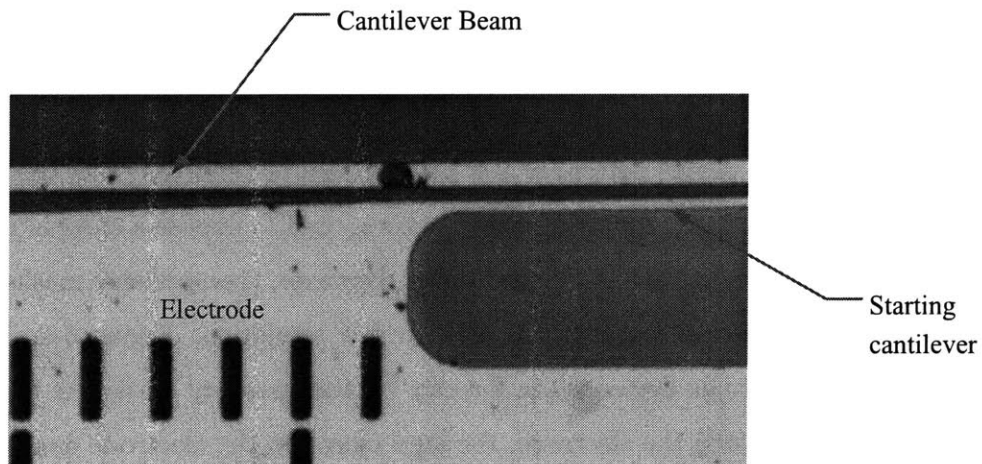
Figure 3-4: microscope photograph of the device made by $10\times$ transparency mask and 10:1 stepper, compared to the device shown in Figure 3-2.

etch rates throughout the wafer, the device mask is haloed everywhere so that the etch space has uniform width. Break-off tabs are used to attach all isolated parts to the wafer so that the devices remains in one piece after etching and prior to bonding to a pyrex substrate.

3.1.2 Shadow wafer

to provide electrode isolation, oxide is grown over both the surface and the side walls of the features etched into the device wafer. To open electrodes so as to permit good electrical contact, a shadow wafer is used to selectively etch oxide from the top surface

72
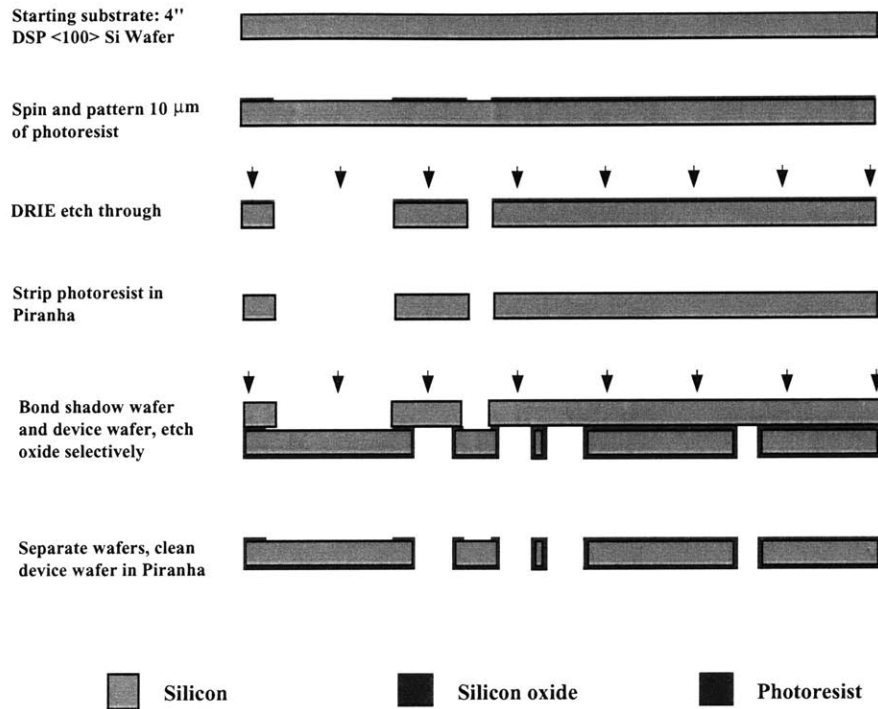
Figure 3-5: shadow wafer process and electrode etching.

of the electrodes. The shadow wafer is also etched using DRIE as shown in Figure 3-5. The etch mask for the shadow wafer is shown in Appendix D. Although the shadow wafer is etched using DRIE in this thesis, it can also be etched using KOH, which would reduce the fabrication cost.

The shadow wafer is then aligned and mounted on the device wafer using photoresist, and the oxide is selectively etched off using RIE. Finally the wafers are separated and cleaned in Pirahna.

3.1.3 Pyrex handle wafer

Next, the device wafer is bonded to a Pyrex 7740 handle wafer. To allow the device wafer parts to translate, the handle wafer receives a 50 μm shallow etch with 49% HF for 8 min to define relief zones. It is known that photoresist does not adhere to Pyrex well and therefore peels off easily in HF [52] [53]. Therefore, to make the etch mask in HF, an adhesion layer consisting of a layer of Ti (50 Å) beneath a layer of Cr (300 Å) is first coated on the pyrex wafer using metal evaporation. Photoresist is then spun

73

Starting substrate: 4"
Pyrex 7740 wafer, 500
μm thick

Deposite 0.005 μm Ti,
0.03 μm Cr

Spin and pattern
photoresist

Pattern Cr in CR-7

Etch Pyrex 50 μm in
49% HF

Clean wafer in Piranha,
then CR-7, then Piranha

Bond device wafer to
Pyrex wafer at 800 V
and 350 degree C

Sputter Au on relay
contacts

Silicon	**Silicon oxide**	**Photoresist**
Titanium	**Chromium**	**Gold**
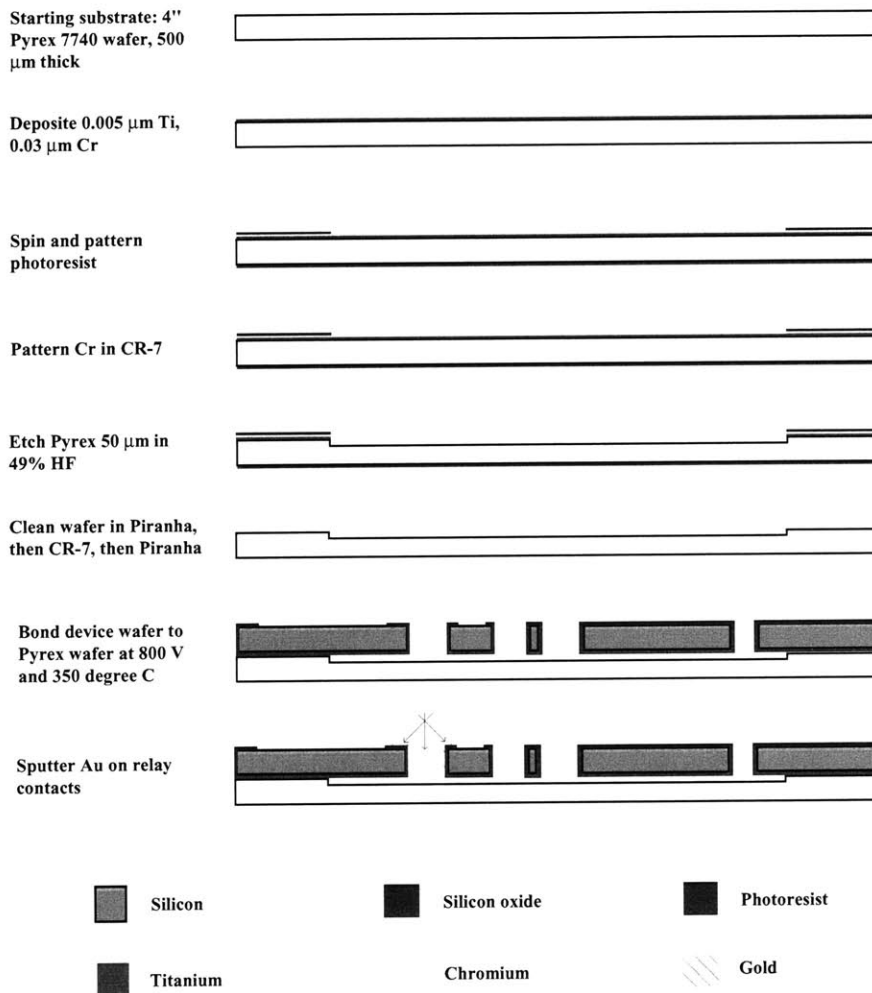
Figure 3-6: handle wafer process and anodic bonding.

and patterned on top of the adhesion layer. The Cr layer is next patterned using *CR-7* chromium etchant before the wafer is etched in HF. After stripping the metal mask and photoresist, the handle wafer is anodically bonded to the device wafer at 350 °C and 800 V for 30 *min*. As a last step, contact metalization can be applied by sputtering through the shadow wafer to achieve low resistance relay contacts [25].

3.2 Fabrication results

Devices are fabricated using the process described in Seciton 3.1. Figure 3-7a shows an optical micrograph of two actuators with starting cantilevers fabricated into a

74
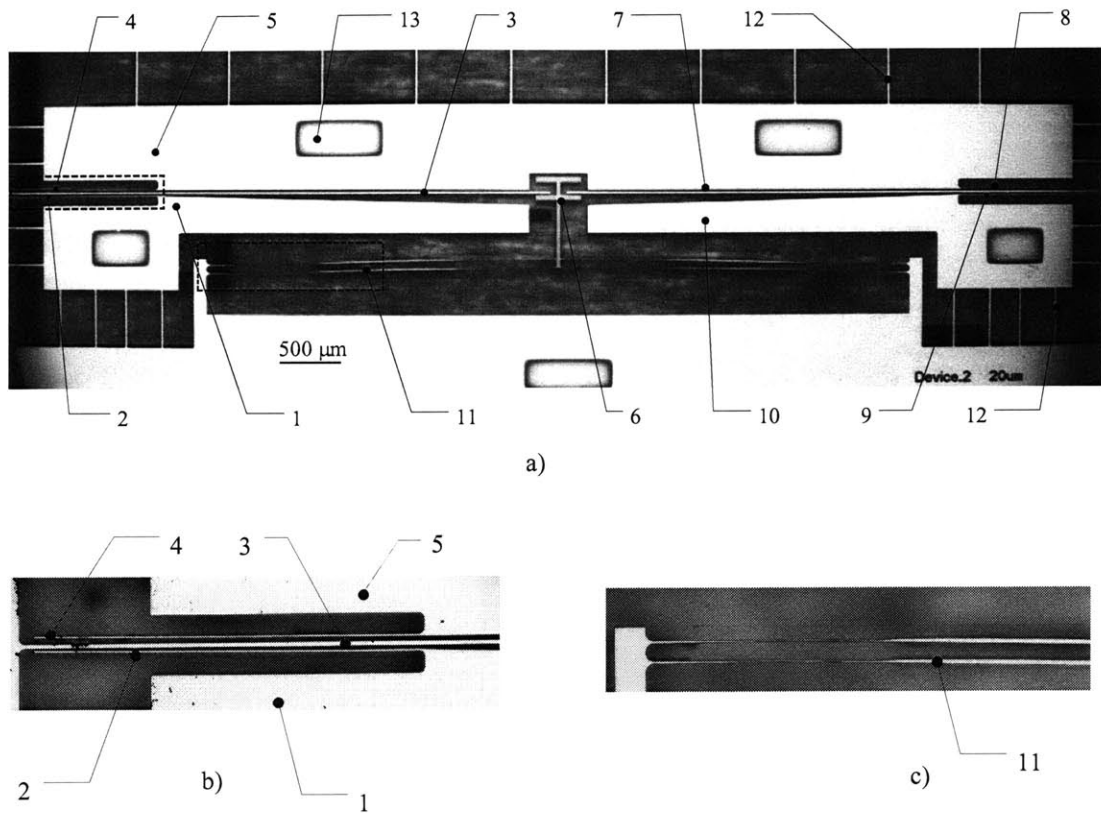
Figure 3-7: microscope photographs of the relay. Figure a) shows the relay as fabricated. Figure b) is the zoomed in picture of the starting cantilever and figure c) shows one end of the switch beam with varying thickness.

bistable relay. The design parameters for actuator cantilever are as listed in Table 2.8. The number labels are as used in Figure 2-8 with the addition of (12) for the break off tabs. The overall size of one device is approximately $9mm \times 2mm \times 0.8mm$. This is much smaller than the required value listed in Table 1.2. Moreover, when making a real device, the break-off tabs can be avoided and the contact pad size can be very small. The overall size can be shrunk to $\sim 9mm \times 0.5mm \times 0.8mm$. This would make it possible to stack more actuators laterally and achieve higher actuation force with reasonable device volume.

The starting cantilever (3) is shown in Figure 3-7b and the left end of the relay beam (11) is show in Figure 3-7c. It can be seen that the relay beam thickness varies along the length very smoothly.
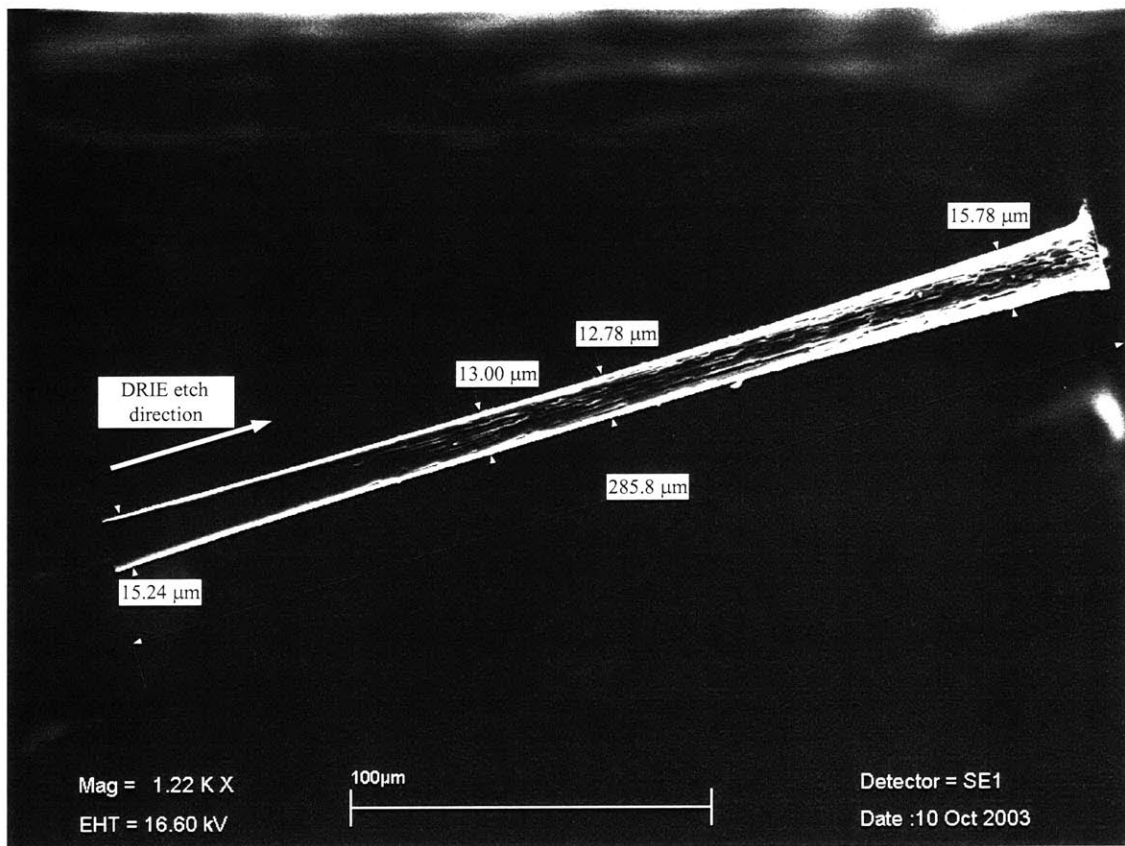
Figure 3-8: SEM picture of the cross section of one actuator cantilever beam.

Cross section profile

The cross section profile is very important for actuator and relay performance. Figure 3-8 shows an SEM picture of an actuator cantilever beam. To compare, the cantilever beam as drawn on the mask was 20 μm thick. After DRIE etching, the thickness was substantially reduced to approximately 13 μm in the middle and 16 μm on the top and bottom. The footing effect was also noticed on the bottom side. The wafer thickness was also measured to be 285 μm, instead of 300 μm as specified. Figure 3-9 shows the sidewall surface etched in DRIE, which has a roughness of $\sim 1\mu$m.

The reduction of beam thickness and width, the thick-thin-thick beam shape and the rough contact surface would cause a significant reduction of both the actuator force and relay reaction force, as will be discussed in Section 3.3.

It is believed that these fabrication variations resulted from the DRIE etching
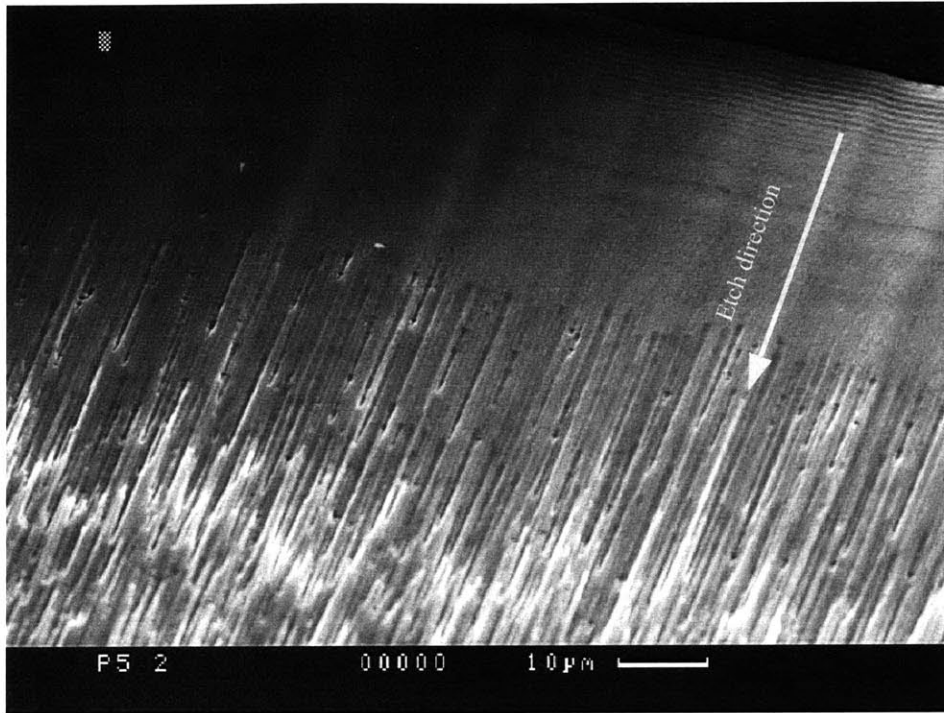
Figure 3-9: SEM picture of the DRIE-etched sidewall of one actuator cantilever beam. The rough surface is caused by BOSCH process passivation.

BOSCH process, which uses a fluorine-based plasma chemistry to etch the silicon, combined with a fluorocarbon plasma process to provide sidewall passivation and improve selectivity to masking materials. The profile, etch rate and selectivity to the mask material can be controlled by adjusting the etch step efficiency, the deposition step or the ratio fo times of the two steps, and so on.

The rough surface comes from the BOSCH process passivation cycles, which is generally on the order of 0.5 μm and produces approximately 1 μm of gap when the two electrodes touch.

A straight cross section profile, as demonstrated in [54], can be achieved by controlling several variables such as coil and electrode power, the duration of the etching and passivating cycles, and chamber pressure. The smallest achieved variation over an etch depth of 300 μm is approximately 2 μm (L. Ho et al, MIT internal report), which is close to the result in this thesis.

In order to etch the sidewall straightly and more smoothly, a Cryogenic process
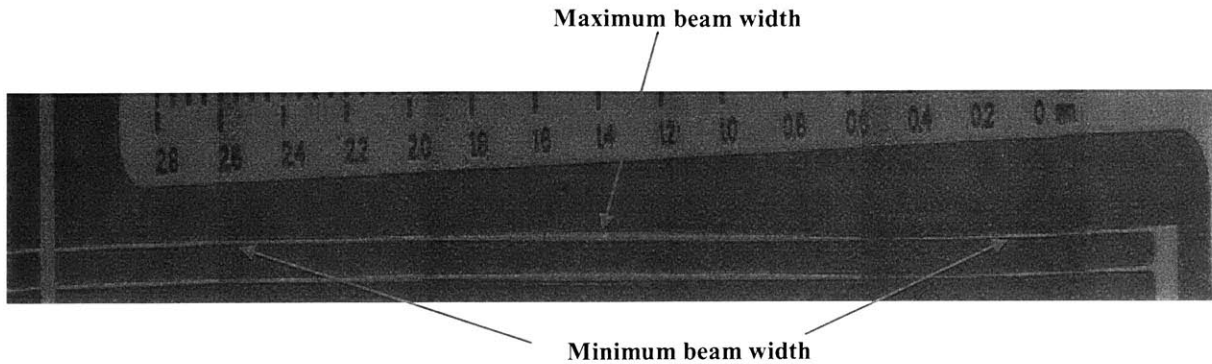
Figure 3-10: the minimum and maximum thicknesses on the relay beam.

can be employed [55]. Rather than using passivating fluorocarbon polymer film as in BOSCH process, the Cryo process forms a blocking layer of oxide/fluoride (SiO_xF_y) on the sidewalls (around $10 \sim 20$ nm thick), together with cryogenic temperatures preventing attack on this passivation layer by the fluorine radicals. The low temperature operation also helps to reduce the etch rate of the photoresist or silicon oxide mask. Because the passivation cycles are avoided in the Cryo process, sidewall roughness is reported to be very small compared to BOSCH process. In addition, the etch rate and mask selectivitity of Cryo process are higher than BOSCH Process. These advantages of Cryo process make it a good candidate for fabricating the electrostatic actuators with a anisotropic profile and smooth side wall, although, due to the facility constraints, the Cryo process was not utilized in this research.

Uniformity

In order to investigate the uniformity of DRIE etching, the minimum and maximum thicknesses on the relay beam to surface, as shown in Figure 3-10, are measured over several devices at various postions on one wafer. Figures 3-11 and 3-12 show the meausrement results respectively. As can be seen, the minium thicknesses vary from 4.5 μm to 6 μm while the maximum thicknesses vary from 12.8 μm to 13.8 μm. It can be concluded that the thickness variation comes mostly from the transparency mask, which has a resolution of $+/-0.5$ μm.

	1	2	3	4	5	6
A		5.6			5.2	
B						
C						
D						
E				4.5		
F		5.9				6.0
G						
H						
I					4.6	
J			4.3			
K						
L						4.7
M						
N	5.7		4.5		4.4	
O						
P						
Q						
R		5.5				

Wafer Flat

Figure 3-11: measurement results of the minimum relay beam thicknesses on various dies on one wafer.

	1	2	3	4	5	6
A						
B						
C						
D						
E						
F		13.9				13.3
G						
H						
I						
J						
K						
L						
M						
N					12.8	
O						
P						
Q						
R		13.3				

Wafer Flat

Figure 3-12: measuremnt results of the maximum relay beam thicknesses on various dies on one wafer.

3.3 Measurement

3.3.1 Static measurement

To achieve electrical isolation between electrodes, the break-off tabs were broken manually. Probes were then electrically connected to the electrodes on the wafer. As shown in Figure 3-13, the zipper cantilever was grounded and positive voltage was added on the electrode through a resistance of 20 $K\Omega$, in order to limit current in the event of a short circuit. The voltage was then ramped up from zero until the relay was actuated.

Pull-in voltage

At a voltage of approximately 80 V, the starting cantilever pulls in, as shown in Figure 3-14a and then continuously zips along the electrode, and actuates the relay beam. At ~ 140 V, the actuator zips completely as shown in Figure 3-14b and closes the relay as shown in Figure 3-14c. After the voltage is removed, the actuator cantilever separates from the electrode while the relay beam remained closed as shown in Figure 3-15. The 80 V pull-in voltage is larger than the predicted 65 V shown in Figure 2.5 because the achieved minimum gap is larger than designed gap of 10 μm according to the beam profile shown in Figure 3-8. At 14 μm of gap, the predicted pull-in voltage is calculated to be approximately 90 V.

Function voltage and force-displacement

The voltage required to toggle the relay beam is measured to be approximately 140 V, higher than the expected 120 V. To measure the force-displacement characteristics of the actuator and the relay beam, a probe was used [56] to push the device and the displacement of the probe-support flexure was magnified through a compliant leverage mechanism. An optical sensor senses the amplified displacement that was pre-calibrated to determine the force. The FEA result of the relay beam and the numerical simulation of the actuator at 140 V are also shown with the experimental data in Figure 3-17. It can be seen that the tested force of the relay beam is 30% less

The actuator cantilever is grounded

Starting cantilever bends up slightly

Electrode (S_iO_2 was etched off here)

Voltage was added through the needle

Tabs were broken to achieve insulation

The Pyrex bond pad

500 μm
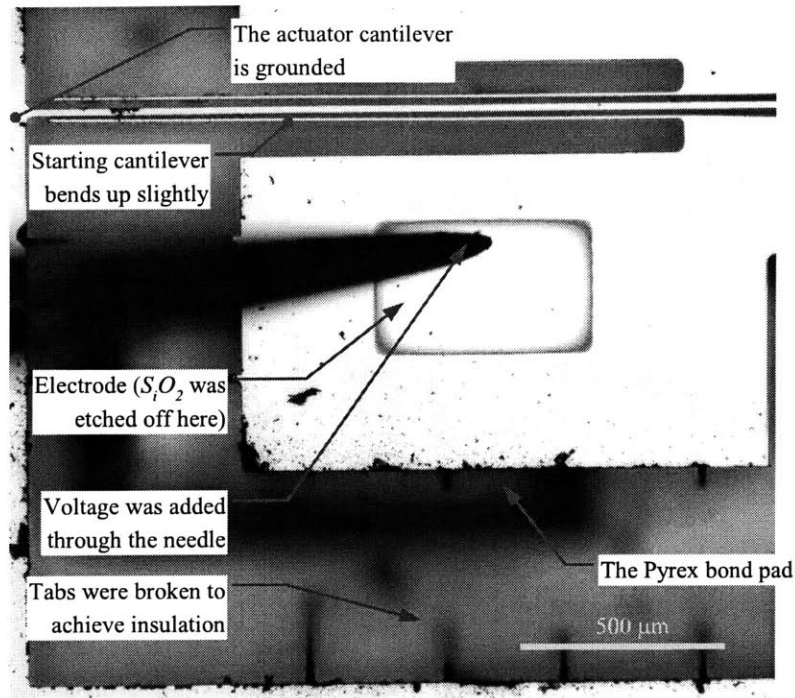
Figure 3-13: microscope photograph of the starting cnatilever when it is attracted and bends up slightly at low voltage.

than the FEA result and the tested force of the actuator is approximately half of the numerical/analytical prediction.

Due to the relay beam force shortfall due to the actuator force shortfall, the measured contact force of the relay is about 1.8 mN, which is still high enough to get a good contact resistance. The reduction of both the actuation force and the relay reaction force is believed due to the beam profile etched by DRIE as shown in Figure 3-8. Based on the analysis in Chapter 2, the actuation force is proportional to I, which results in an approximate 20% decrease in actuation force when taking an average of 14 μm for the beam thickness. Furthermore, the wafer thickness was actually 285 μm instead of 300 μm, which lowers the force by an additional 5%. Moreover, when two electrodes touch, a gap of up to 5 μm is left between the two electrodes at the contact point because the side wall shape bows in at the middle. This reduces the electrostatic actuation force further down by approximately 20%. To analyze the relay beam according to the fabrication result, a new model is analyzed

81
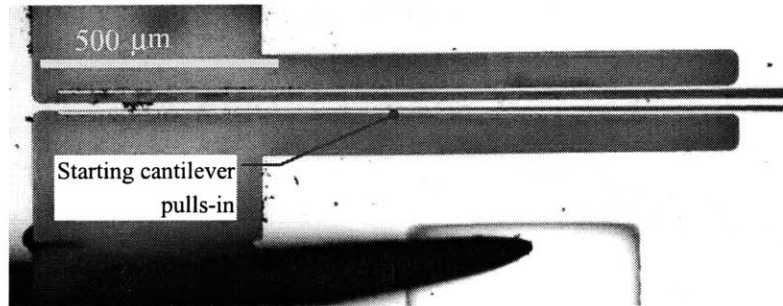
a)
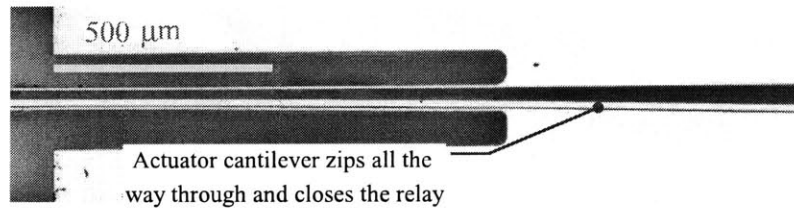
b)
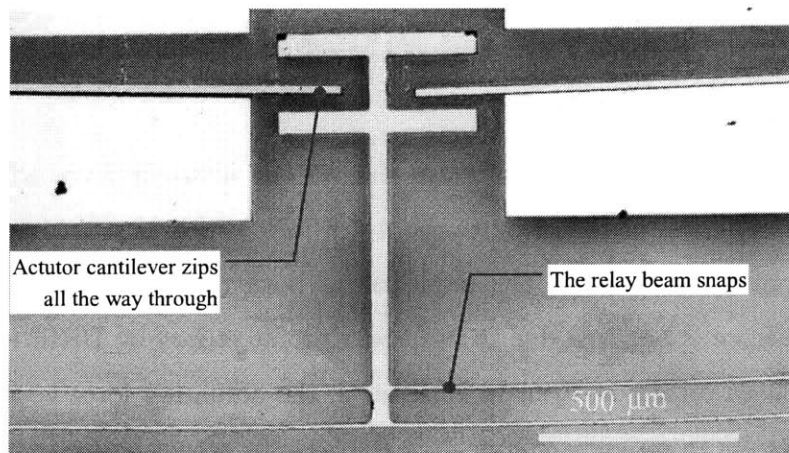
c)

Figure 3-14: microscope photographs of the relay in actuation. Figure a) shows the starting cantilever pulls in. In Figure b), the actuator cantilever zips completely to toggle the bistable relay beam as shown in Figure c).

| Actutor cantilever separates from the elctrode | The relay beam remains stable |

500 μm
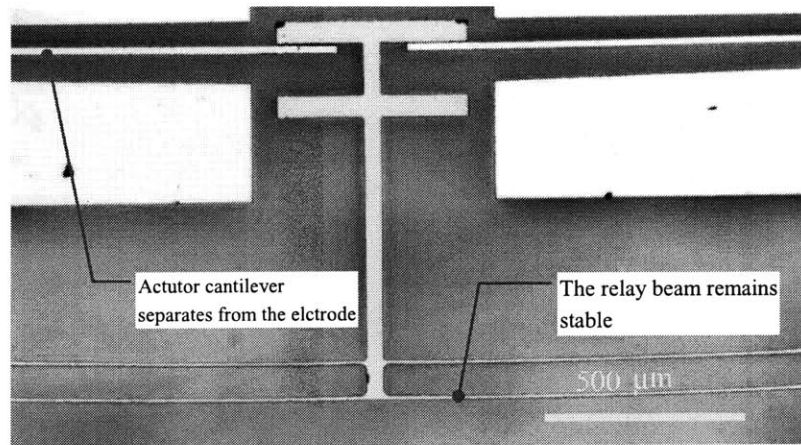
Figure 3-15: the actuation voltage is removed while the relay beam remained closed at its 2nd stable position.
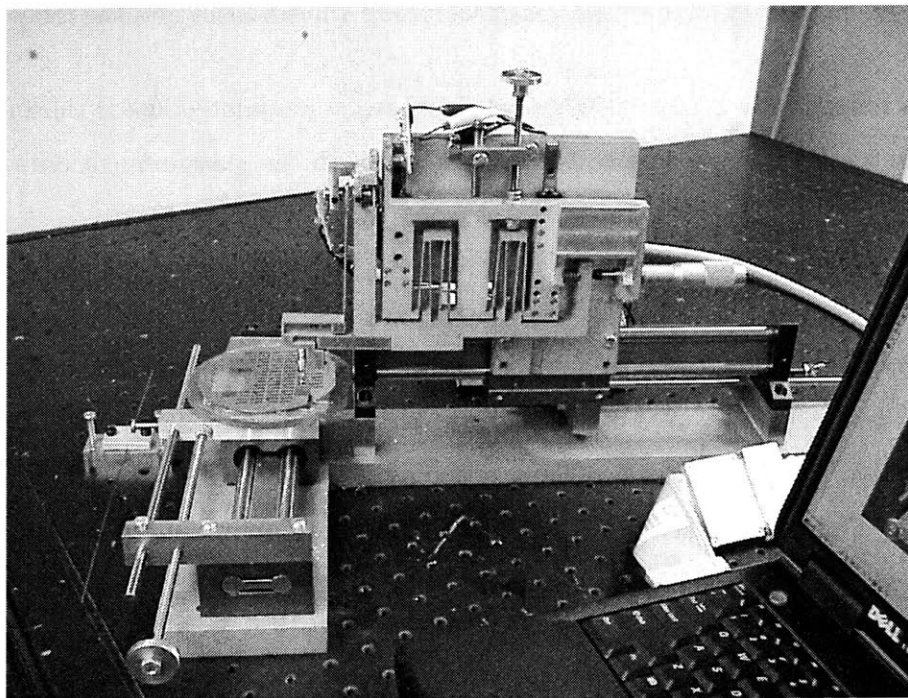
Figure 3-16: the Flextester^{TM} that measures the stiffness of the devices.
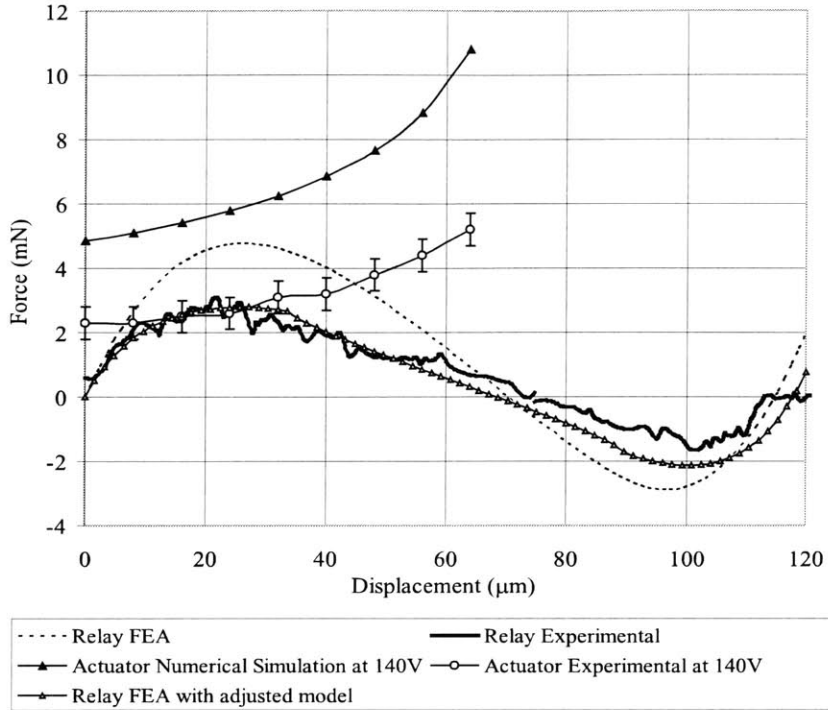
Figure 3-17: measured force-displacement curves of the actuator and the relay beam.

thickness reduction of 6 μm. (new model thickness = modulated shape thickness - 6 μm.) The result shown in Figure 3-17 agrees well with the measurement data.

Breakdown voltage

Break down voltage is tested over several devices across the whole wafer, as shown in Figure 3-18. The measured oxide thickness is approximately 200 nm and therefore the insulation layer thickness is 400nm, accounting for the two sides of the touching electrodes. This gives a theoretical breakdown voltage of approximately 400 V, given the dielectric strength of silicon oxide

$$R_{breakdown,oxide} = 1 \times 10^7 V/cm \tag{3.1}$$

However, the measured breakdown voltages are much lower than the predicted value. As can be imagined, this would lower the highest achievable actuation force and hence

However, the measured breakdown voltages are much lower than the predicted value. As can be imagined, this would lower the highest achievable actuation force and hence it is very important to achieve a higher breakdown voltage. The possible reasons for the lower breakdown voltage and their respective countermeasures are listed as follows.

1) As shown in Figure 3-19, the passivation cycles yield sharp corners on the sidewalls. Hence the electric field around these sharp corners is much higher than in other areas, which would lower the breakdown voltage. This can be improved by smoothing the sidewall during or after the DRIE. For examples, the Cryogenic process inherently smooth the sidewall; thermal oxidation can also partly diminish the sharp corners.

2) Sharp corners on the wafer surface due to the device feature and/or mask resolution. This can be improved by rounding every corner and/or using a high resolution mask.

3) Defects during oxidation that reduces the dielectric strength of the oxide. This can be improved by cleaning the wafer thoroughly before oxidation and avoiding any possible contamination during oxidation.

4) Contaminants between the two electrodes during testing. By packaging the device in vacuum, this can be avoided.

3.3.2   Dynamic measurement

Measurement setup

During static measurements, the actuator closes and opens the relay as expected at the first applied DC pulse. However, the relay cannot be closed or opened at the second pulse unless a higher voltage is applied. The voltage required to close/open the relay increases with every cycle. (Note here that the recorded measurement results in Secion 3.3.1 are all first applied voltages.) This effect, which is also called electrostatic stiction, is believed to be caused by charge accumulation on electrode surfaces [57]. To prevent this, insulation bumpers between two electrodes can be used to reduce

85
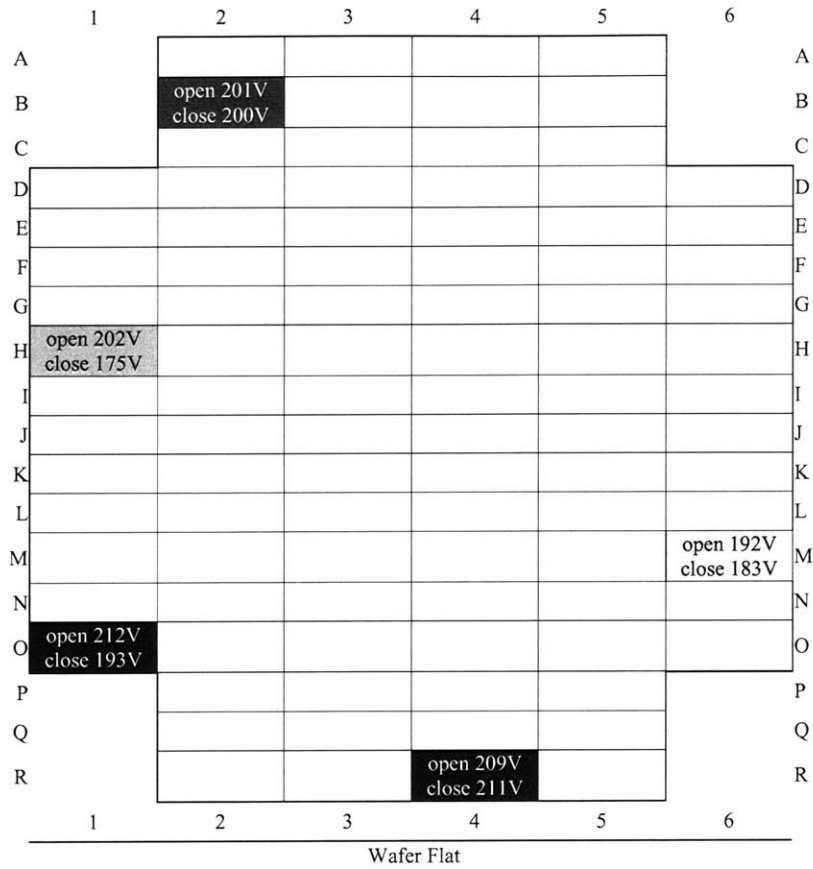
Figure 3-18: breakdown voltages of the insulation layer for various dies on one wafer. Open breakdown voltage is tested between the actuator beam and the upper electrode, while close breakdown voltage is tested between the actuator beam and the bottom electrode.
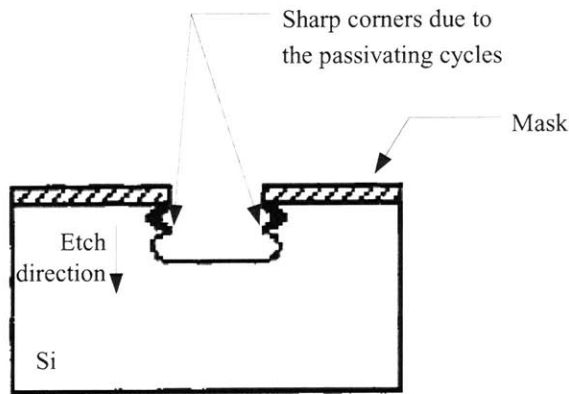
Figure 3-19: sharp corners on sidewalls caused by DRIE passivation cycles.

the contact area and thus reduce the accumulated charge; however, this increases size and reduces force producing area. Another method is to use very short excitation pulses.

In this thesis, as shown in Figure 3-20, a bipolar circuit is designed to drive the actuators. A square-wave low-voltage input signal with period of $2T$ is first modulated by a **74LS74** flipflop and then amplified to generate two signals with periods of $4T$, which are labeled as "Top electrode" and "Middle electrode" in Figure 3-21. The "Top electrode" signal is then inverted to generate a third signal labeled as "Bottom electrode". As can be seen, there is a phase difference of $\pi/2$ between "Top electrode" and "Middle electrode" and a phase difference of π between the "Top electrode" and "Bottom electrode". To actuate the device, the "Middle electrode" is added to the actuator cantilever beam and the other two signals are added to top and bottom electrodes respectively, as shown in Figure 3-20. The actuator cantilever can then be switched between the two electrodes and toggle the relay beam. As can be imagined, for every two consecutive cycles between the middle and top/bottom electrode, the actuation polarity is reversed; hence the accumulated charge from the last cycle is canceled out. Electrostatic stiction can be avoided by these means.

Fracture cycles

Using the bipolar drive, the relays were operated at 100 Hz for over 120 hours through more than 40 million cycles without any observed stiction or mechanical fatigue.

Excitation voltage pulse

The relays have been switched with voltage pulses as short as 400 μs.

Switching speed

The recorded highest frequency of the input signal was approximately 160 Hz. Since the relay closes/opens within half of the period of the input signal, it can be calculated
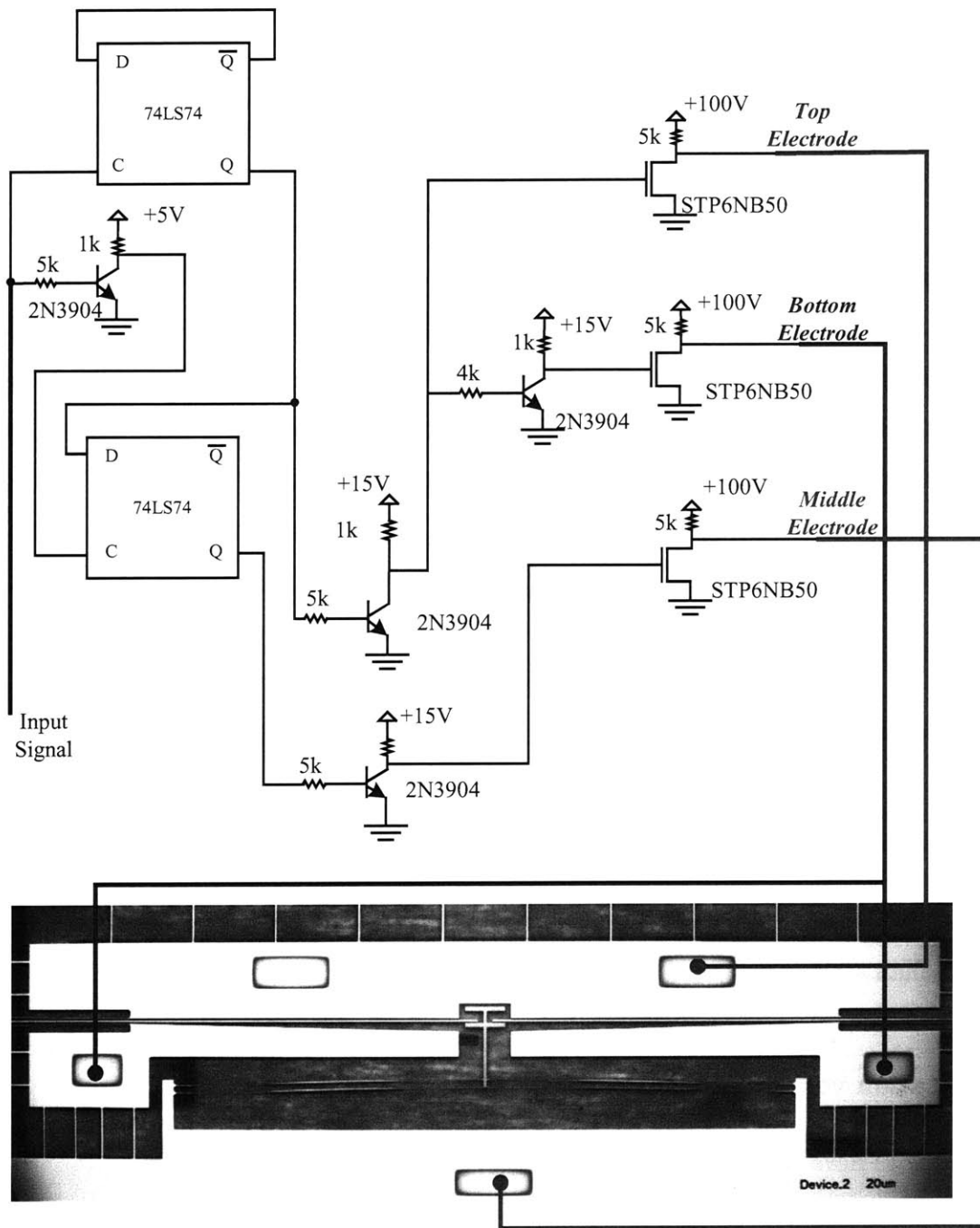
Figure 3-20: dynamic measurement setup.
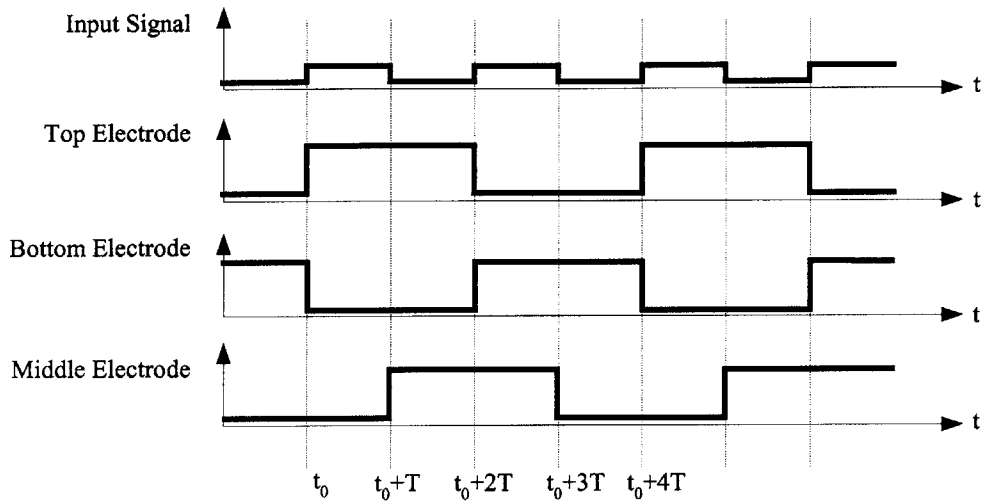
Figure 3-21: bipolar drive signals.

that the response time of the relay is

$$t_{response} = \frac{1}{2f_{input}} = 3.1 \; ms \tag{3.2}$$

This was also proved by counting the delay time between the switching cycles and the switched signal. To do this, two relay contacts were designed and fabricated into the system, as will be discussed in details in Chapter 4. Using the same setup described above, the voltages on the middle electrode (i.e., the actuator cantilever) and the contact are monitored and recorded as shown in Figure 3-22. In the first half of the recorded cycle, both of the middle and bottom electrode are connected to a high voltage (140 V in this case). The contact is isolated and the voltage is measured to be zero. When the bottom electrode is changed to low voltage, the actuator cantilever closes the relay beam. The contact is then connected to the middle elctrode which is on a high voltage. The delay between the switching of contact voltage and the electrode voltage is then the switching time, which is approximately 2.8 ms as shown in Figure 3-22.

89
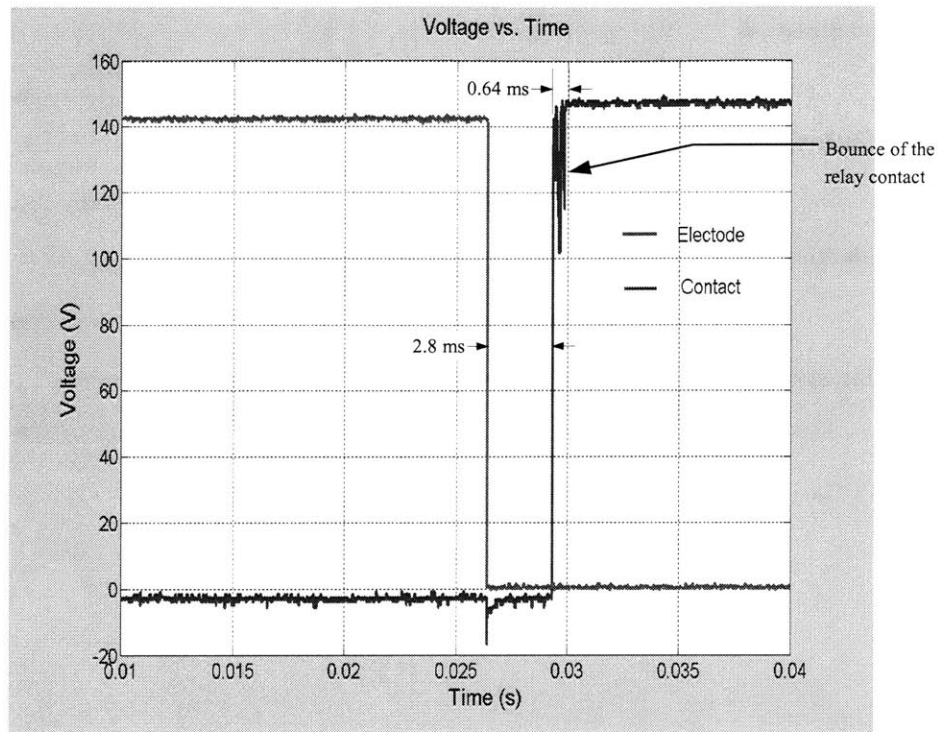
Figure 3-22: switching speed of the relay.

Relay contact bounce

Relay contact bounce is also observed in Figure 3-22 and the bounce time is measured to be 0.64 ms. A zoomed in view of the bounce is shown in Figure 3-23.

A dynamic model

The switching time includes 1) the time taken for the cantilever to zip along the elctrode until enough force is developed to actuate the relay and 2) the response time of the relay beam from one stable postion to the other. To calculate the switching speed of the system, it is desirable to analyze the dynamic behavior of the cantilever beam in actuation. Numerical analyses were developed in [58] and [59] for electrostatic actuators before pull-in. With the analysis described in Chapter 2.2, it is now possible to generate a dynamic model for numerical analysis after the actuator cantilever is pulled-in. A numerical model is proposed here. To begin, the Euler beam equation

90
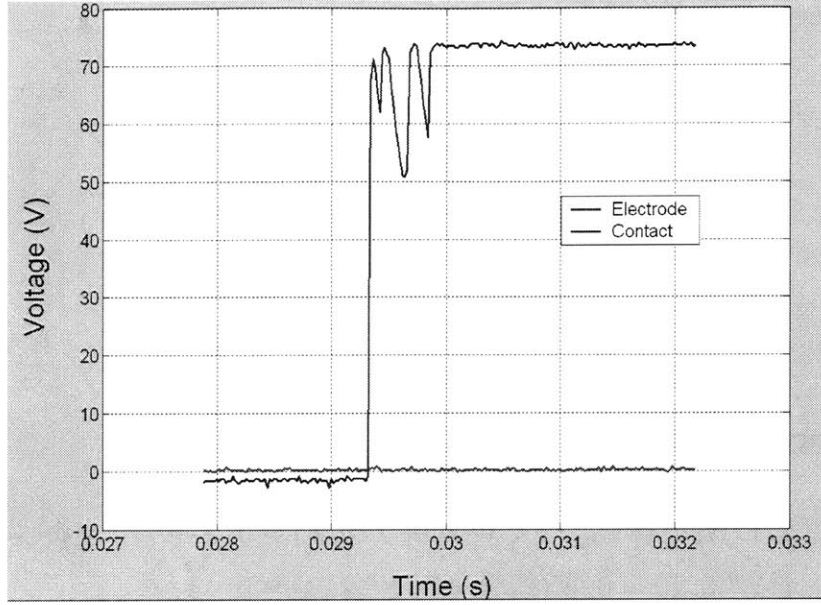
Figure 3-23: relay contact bounce.

is first written as

$$\rho b h \ddot{y} = -\frac{\varepsilon_0 U^2 b}{2(y - c(x) + h_0/\varepsilon_r)^2} - EIy'''' - p_f^* \quad s \le x \le L \quad (3.3)$$

where

$$\ddot{y} = \frac{\partial^2 y}{\partial t^2}, \quad y'''' = \frac{\partial^4 y}{\partial x^4}.$$

and p_f^* is the force per unit length provided by the squeeze-film between the actuator cantilever and the curved electrode. Assume the actuator cantilever has a velocity of 0 at $t = 0$, the boundary conditions are

$$\begin{cases} y(x,0) = y_0, \ y(x,0) = 0, \ y(s,t) = C(s), \ y'(s,t) = C'(s) \\ y''(s,t) = 0, \ y(L,t) = 0, \ y''(L,t) = 0 \end{cases} \quad (3.4)$$

where y_0 is the initial profile function of the actuator cantilever. y_0 can be solved as described in Section 2.3.1

91

To normalize Equation 3.3, let

$$
\begin{cases}
Y = y/h - c/h, \ X = \frac{x/L - s/L}{1 - s/L}, \ \lambda = 1 - s/L \\
T = t/t_0, \ P_f^* = \frac{p_f^* t_0^2}{\rho h^2} \\
\alpha = \frac{\varepsilon_0 U^2 t_0^2}{2\rho h^4}, \ \beta = \frac{h_0}{\varepsilon_r}, \ \theta = \frac{E h^2 t_0^2}{12\rho L^4}
\end{cases}
\tag{3.5}
$$

to get

$$
\ddot{Y} = -\frac{\alpha}{(Y + \beta/\varepsilon_r)^2} - \theta \lambda^4 Y'''' - P_f^*
\tag{3.6}
$$

with boundary conditions

$$
\begin{cases}
Y(X,0) = Y_0, \ \dot{Y}(X,0) = 0, \ Y(0,T) = 0, \ Y'(0,T) = 0 \\
Y''(0,T) = 0, \ Y(T,1) = 0, \ Y''(T,1) = 0
\end{cases}
\tag{3.7}
$$

Equation 3.6 can be solved using standard central finite difference approximations

$$
\ddot{Y}_n = \frac{Y_n^{i+1} - 2Y_n^i + Y_n^{i-1}}{\Delta_t^2}
\tag{3.8}
$$

and

$$
Y_n'''' = \frac{Y_{n+2}^i - 4Y_{n+1}^i + 6Y_n^i - 4Y_{n-1}^i + Y_{n-2}^i}{\Delta_x^2}
\tag{3.9}
$$

where Δ_t and Δ_x are the time and location incremental steps, respectively. By assuming

$$
\xi = \Delta_t^2 / \Delta_x^4
\tag{3.10}
$$

and substituting Equations 3.8 and 3.9 into 3.6

$$
Y_n^{i+1} = \xi\theta\lambda^4(Y_{n+2}^i - 4Y_{n+1}^i - 4Y_{n-1}^i + Y_{n-2}^i) + 6\xi\theta\lambda^4 Y_n^i - Y_n^{i-1} - \frac{\alpha\Delta_t^2}{Y_n^i + \beta/\varepsilon_r} + P_{f\,n}^{*i}
\tag{3.11}
$$

The squeeze-film pressure can be solved using Renolds equation [60]

$$
\frac{\partial}{\partial x}\left(\frac{\rho_a y^3}{12\mu_a}\frac{\partial p_f}{\partial x}\right) + \frac{\partial}{\partial z}\left(\frac{\rho_a y^3}{12\mu_a}\frac{\partial p_f}{\partial z}\right) = \frac{\partial(\rho_a y)}{\partial t}
\tag{3.12}
$$

where μ_a and ρ_a are the viscosity and density of air respectively. Equation 3.12 can

be simplified by assuming that the pressure $p(x, z)$ is a separable function of x and z

$$p_f(x, z) = P_f(x)(1 - \frac{4z^2}{b^2})$$ (3.13)

where $P_f(x)$ is the squeeze film pressure acting on the beam at $z = 0$. Substituting Equation 3.13 into 3.12 yields

$$(1 - \frac{4z^2}{b^2})\frac{\rho_a y^3}{12\mu_a}\frac{\partial^2 P}{\partial x^2} + \frac{\partial P_f}{\partial x}\frac{\partial y}{\partial x}(1 - \frac{4z^2}{b^2})\frac{\rho_a y^2}{4\mu_a} - \frac{\rho_a y^3}{12\mu_a}P_f\frac{8}{b^2} = \frac{\partial y}{\partial t}\rho_a$$ (3.14)

Note here that ρ, μ and y are assumed to be independent of z. Next, integrate Equation 3.14 across wafer depth b

$$2by^2\frac{\partial y}{\partial x}\frac{\partial P}{\partial x} + \frac{2by^3}{3}\frac{\partial^2 P}{\partial x^2} - \frac{8y^3}{b}P(x) = 12b\mu_a\frac{\partial y}{\partial t}$$ (3.15)

The pressure force per unit length $p_f^*(x)$ can be calculated by integrating Equation 3.13

$$p_f^*(x) = \frac{2b}{3}P(x)$$ (3.16)

Using Equations 3.15 and 3.16, the damping pressure at every node x at time "$t + \Delta_t$" can be calculated with the beam profile function $y(x, t)$ and the pressure at time "t". Putting the solved damping pressure into Equation 3.11 then solves the next beam profile function y at next time step.

Combining this model after pull-in and the model given in [58] and [59] before pull-in would then solve the displacement of zipping actuator cantilever.

Chapter 4

Relay Contact

This chapter describes the micro relay contact fabricated using DRIE and wet anisotropic KOH etching. Section 4.1 first presents the relay contact fabricated using DRIE and addresses the challenge to ahieve low contact resistance by sputtering metal on vertical DRIE-etched contact surfaces. Section 4.2 then demonstrates a new design that utilizes wet anisotropically KOH etched Si {111} planes as relay contact surfaces. Experimental devices were fabricated and very low contact resistance was achieved through the experimental device. Finally, a fabrication process is proposed to build the full relay with Si {111} contact surfaces.

4.1 Contact created using DRIE

Now that the device fabricated in Chapter 3 was shown to provide enough contact force and stroke, a full relay is designed and fabricated. As shown in Figure 4-1, a crossbar is attached to the bistable relay beam through a laterally compliant spring and two contacts are connected to the silicon base through break-off tabs. After the break-off tabs are broken, the two contacts are then electrically insulated. As the relay beam is closed by the two actuators, as shown in Figure 4-2, two contacts are elctrically connected through the crossbar. To accomodate fabrication error, the laterally compliant spring is designed such that the contact position is always located in the second positive stiffness region of the relay beam [24].

95

4.1.1 Metal deposition

As can be seen from the fabrication process, the sidewalls of the contacts and the crossbar are covered with oxide as shown in Figure 3-6. To achieve good electrical contacts, a thin layer of metal is deposited onto the crossbar and contacts through a shadow wafer, both on the surface and sidewalls. Here Au is selected as the contact metal due to its low resistivity. Because the contact surfaces are the DRIE-etched sidewalls and the connection point is on the top surface, it is necessary to put enough Au on both surface and sidewall and to cover the sharp corners in order to achieve a low contact resistance. To do so, both evaporation and sputtering processes are studied as follows.

Evaporation

For the evaporation process, there is a strong directional electric field in the chamber [61] and the wafer is far from the evaporation source. Therefore the electron beams are very directional and it is usually difficult to put metal onto vertical sidewalls. One countermeasure is to use a tilted plate to carry the wafer and rotate the plate during evaporation, which would deposit metal from different directions.

Sputtering

For sputtering process, the wafer is put $\sim$ 10 cm under a Au target that has a comparable size to the wafer. Argon ions are accelerated and hit the target with high energy. Au is then separated from the target and hits the wafer from different directions. It is showed in [24] that sputtering makes far better metal conformity than does the evaporation process.

4.1.2 Metal on sidewalls

For both evaporation and sputtering processes, however, the gap between the crossbar and the contact is very narrow ($\sim$100 μm) compared to the wafer depth (300 μm) and therefore the metal deposited on the sidewalls is much less than on the surfaces.
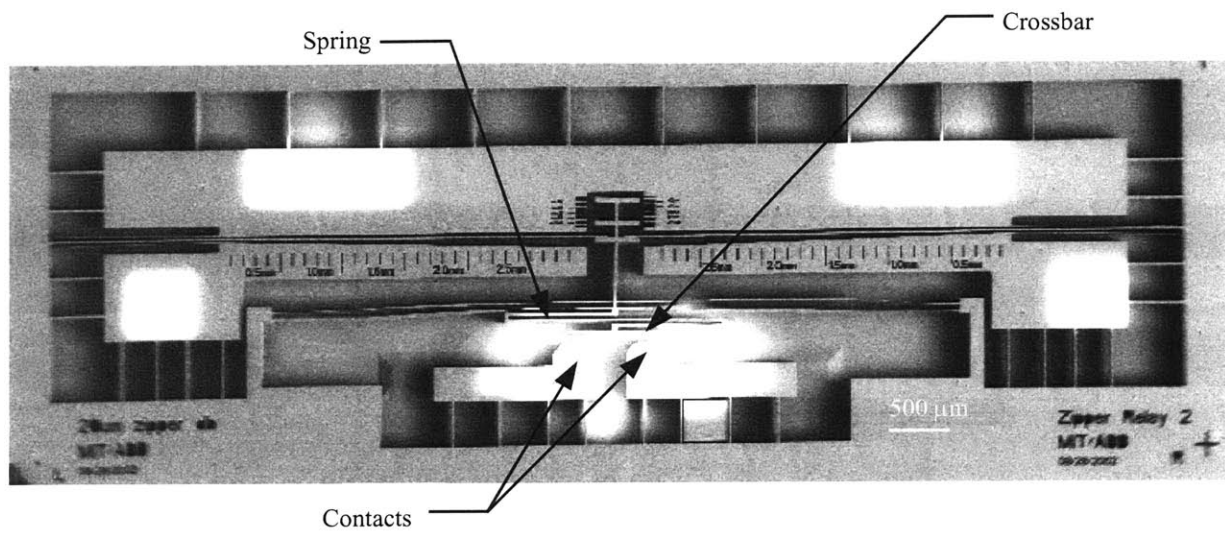
Figure 4-1: SEM picture of the relay as fabricated with crossbar and contacts. Note that the regions with white color are the probe and relay contact regions in which the isolation oxide is removed using RIE and a shadow wafer, and gold is sputtered.
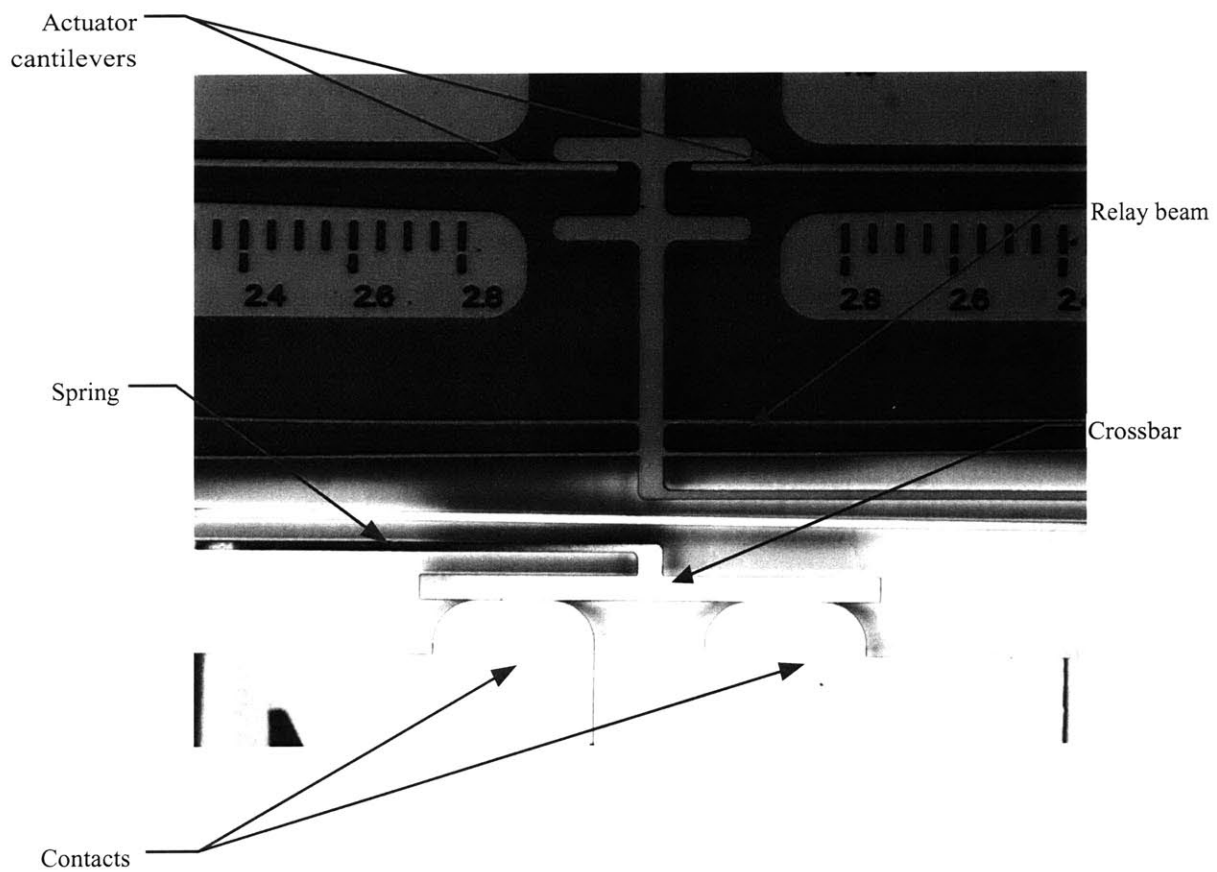
Figure 4-2: microscope photograph of the closed relay shown in Figure 4-1.
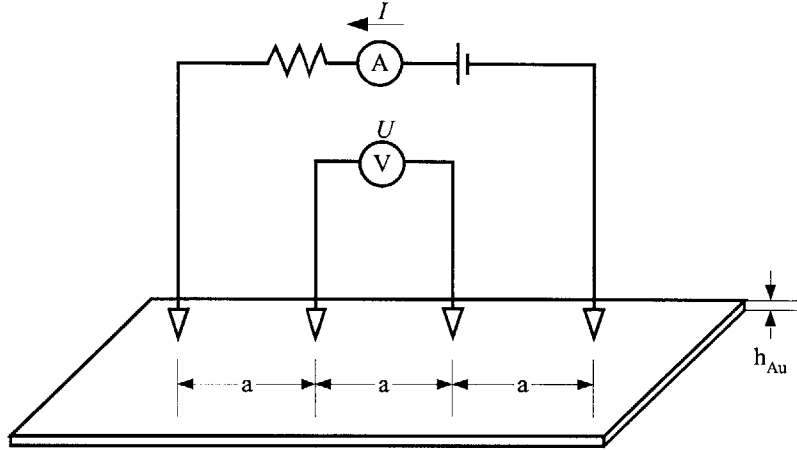
Figure 4-3: gold thickness measurement set up.

A geometric estimation shows that the sidewalls can only receive ~10% of metal on the surface with these dimensions. A 4-point-probe measurement was performed to test the thicknesses of the sputtered Au as shown in Figure 4-3. By measuring the current I and voltage U, the gold thickness can be calculated as

$$h_{Au} = \frac{\sigma I ln(2)}{U\pi} \tag{4.1}$$

where σ is the specific resistance of gold. The measurement results a 15 nm thick Au layer on the sidewall as shown in Figure 4-4a. The same measurement is performed on the wafer surface shown in Figure 4-4b and it results a thickness of approximately 90 nm.

Additionally, it is difficult to cover the straight corner with reasonable amount of metal. All these characteristics of DRIE-etched sidewalls make it difficult to achieve very low contact resistance with metal deposition. In [26], using metal sputtering, the contact resistance was measured to be approximately 1 Ω on DRIE-etched contact surfaces. In this thesis, the lowest achieved contact resistance with 0.5 μm (on the top surface) of sputtered Au is approximately 2 Ω. In [24], in order to achieve low contact resistance, a seed layer was first deposited on the DRIE-etched sidewalls using sputtering. Electroplating was then utilized to put more gold on the sidewalls and cover the straight corner. Because the electroplating process is more complicated and

<center>a)</center>

<center>b)</center>
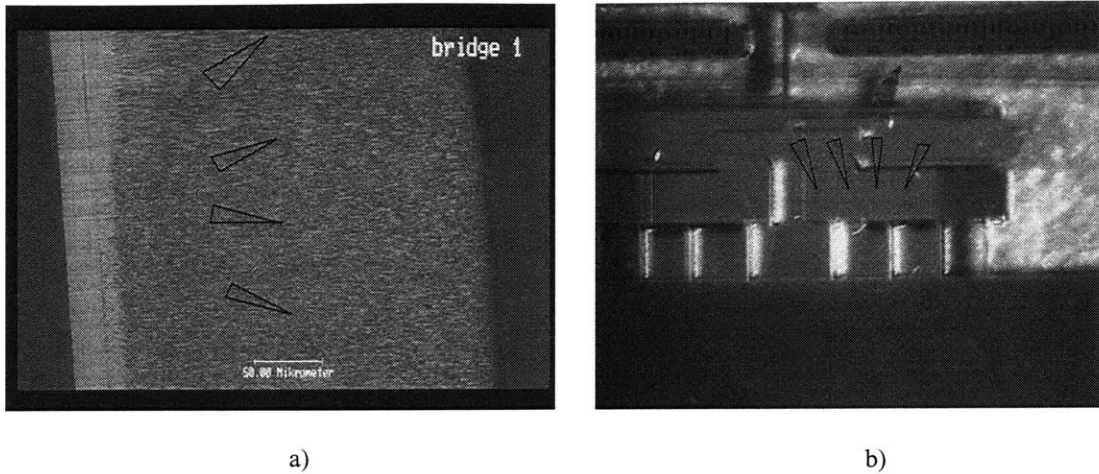
Figure 4-4: figure a) shows the tip position on the sidewalls and figure b) shows the tip positon on the wafer surface.

more expensive than metal deposition, it is still desirable to design a relay with which low contact resistance can be achieved by a simple sputtering or evaporation process.

4.2 Contact created using wet anisotropic etching

To design the new relay, the contact surfaces must not be vertical to the wafer plane and they have to be open to metal depostion. To form these kinds of surfaces, it is possible to use wet anisotropic etching that exposes slant crystal planes in Silicon.

4.2.1 Wet anisotropic etching

In addition to the traditional microelectronics fabrication methods, anisotropic wet etching is one of the most commonly used etching methods in MEMS. The wet etchants include the hydroxides of alkali metals (e.g., NaOH, KOH, etc.), tetram-ethylammonium hydroxide (TmAH), etchylene diamine pyrochatecol (EDP) and so on. For example, KOH, as the most commonly used etchant so far, etches silicon {111} planes at a rate 100 times slower than it etches {100} planes [62]. The etch direction is therefore controlled by the crystal plane angle and can be very accurate, this opens up oppportunities to fabricate three dimensional micro mechanical struc-

<center>99</center>

(a) Deposit nitride

(b) Spin and pattern photoresist

(c) Pattern nitride

(d) Strip photoresist,
KOH etch

(e) Strip nitride,
sputter Au

(f) Bring to contact
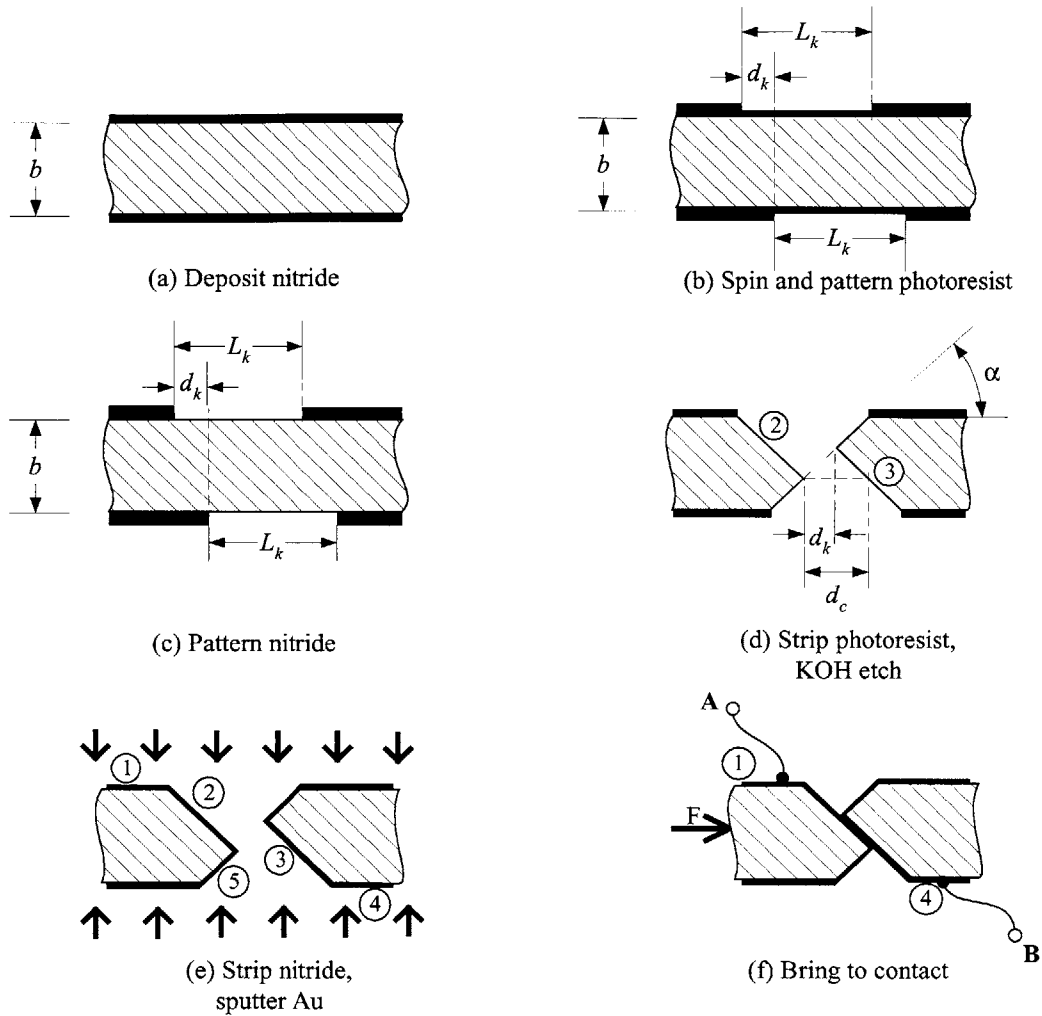
Figure 4-5: process of fabrication and operation of the KOH relay contact (C-C' view of Figure 4-8.

tures such as V grooves and trenches. More sophisticated devices were also achieved by bonding two or more stacks. In addtion, the {111} crystal planes exposed during the etching are extremely smooth and can be applied in different areas.

4.2.2 Design

Based on these characteristics of wet anisotropic ething, a micro relay contact etched using KOH is designed and fabricated as shown in Figure 4-5. A 4-inch, $\langle 100 \rangle$, n type, 300-μm thick bare silicon wafer is first cleaned in RCA. The wafer is then deposited

with 1500 Å of silicon nitride using PECVD in tube 6D in the Integrated Circuits Laboratory (ICL) at MTL. Next, a 1.5 μm of photoresist layer is coated on both sides of the wafer. The front side photoresist is then patterned using a mask as shown in Appendix E, one die of which is shown in Figure 4-8. On the back side, a second mask is used for patterning the photoresist. Note here that the back side pattern, as shown in Figure 4-5a, is shifted relative to the front side. An RIE etching is then employed to pattern the nitride in STS-1 in th Technology Research Laboratory (TRL) at MIT, using the recipe *Nitride* for 8 min. The photoresist is next stripped off in Piranha before the wafer is etched in a 30% KOH solution at 83 °C. The KOH etching is performed in the EML at MTL. To control the etching time, the wafer is inspected every 2 *min* after it is etched though until the correct structures are formed. Finally, the nitride is stripped in hot phosphoric acid (H_3PO_4) and a gold layer is sputtered from both sides as shown in Figure 4-5e.

During the KOH etching, due to the offset between the front and back side mask, the two triangles etched from both sides meet in the middle and two parallel surfaces (2) and (3) are formed as shown in Figure 4-5d. With the dimensions shown in Figure 4-5c, a straightforward geometry analysis shows that

$$L_k = d_k + \frac{b}{\tan(\alpha)} \tag{4.2}$$

and the contact gap is $d_c = 2d_k$. In our design, the wafer thickness is $b = 300$ μm and the required contact gap $d_c = 100$ μm. Given $\alpha = 54.74°$, L_k is calculated to be 262.1 μm and $d_k = 50$ μm. The contact length is

$$w_k = \frac{d_k}{\cos(\alpha)} \tag{4.3}$$

Apparently, it is now easy to deposit metal onto surfaces (2) and (3) with an angle of α, which is 54.7° for KOH etching. Assume the electron beams are anisotropic, an estimation shows that

$$h_{Au,2,3} = h_{Au,1,4} \cos(\alpha) \approx 0.58 h_{Au,1,4} \tag{4.4}$$

101
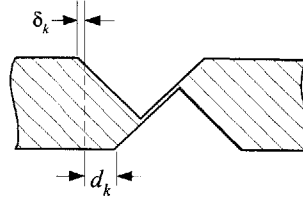
Figure 4-6: fabrication result when front-back mask shift d_k is larger than designed.

where $h_{Au,2,3}$ is the thickness of gold layer on surfaces (2) or (3), and $h_{Au,1,4}$ is the thickness on surface (1) or (4). In the sputterer, where the electron beam is isotropic, the ratio of $h_{Au,2,3}/h_{Au,1,4}$ would be even higher. Moreover, the corner is covered better than with vertical sidewalls. Additionally, when in contact, two slanted surfaces wipe each other and create smoother contact surfaces. All these features would then result a low contact resistance across surfaces (1) and (4).

4.2.3 Fabrication issues

During fabrication for this device, a small misalignment would result in a substantial change of the structure. Two possible misalignments are shown in Figures 4-6 and 4-7. If the front-to-back offset d_k is larger than the designed value, the two triangles would not meet. As a result, a thin 111 film forms as shown in Figure 4-6. Since {111} planes are etched very slowly in KOH, this film cannot be etched away and hence the contact surfaces cannot be formed. On the other hand, if d_k is smaller than the designed value, the etching from two sides meet in the middle earlier than expected so that two sharp corners are first formed as shown in Figure 4-7a. This sharp corner can be etched very fast in KOH and the parallel surfaces can finally be achieved as shown in Figure 4-7b. However, from a straightforward geometry analysis, the contact area is smaller than the theoretical value.

In this thesis, the alignment error comes from 1) mask resolution and 2) the exposure alignment. The mask resolution is 4 μm and the exposure error using Electronic Visions Model EV620 Mask Aligner is approximately 1 μm. In order to avoid a misalignment shown in Figure 4-6, the offset d_k is deliberately drawn to be 6 μm smaller than the designed value. As a penalty, the contact area is reduced.

102
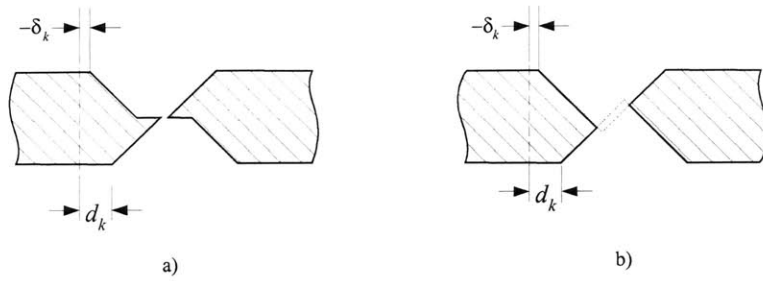
Figure 4-7: fabrication result when front-back mask shift d_k is smaller than designed. a) shows the etching from two sides just meet in the middle. b) shows the sharp corner in the middle is etched away and two parallel surfaces are formed.
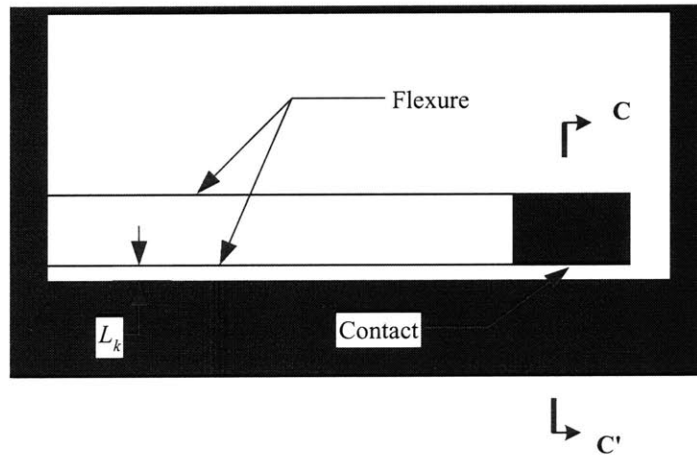
Figure 4-8: front side mask of the KOH relay contact.

4.2.4 Measurement

Experimental devices

To test the contact resistance, experimental devices are fabricated. As shown in Figure 4-8, the relay contact is attached to the solid base using two parallel flexures in order to avoid rotation of the contact when deformed. The convex corners [63] of the contact are not compensated because 1) there is no extra space between the contact and the silicon base and 2) the over etch of the convex corner would not influence the test. The front and back side mask are shown in Appendix E and the process is listed in Appendix F in details. It is worth noting that the whole experimental device, including the parallel flexure beams, is etched in KOH.

103
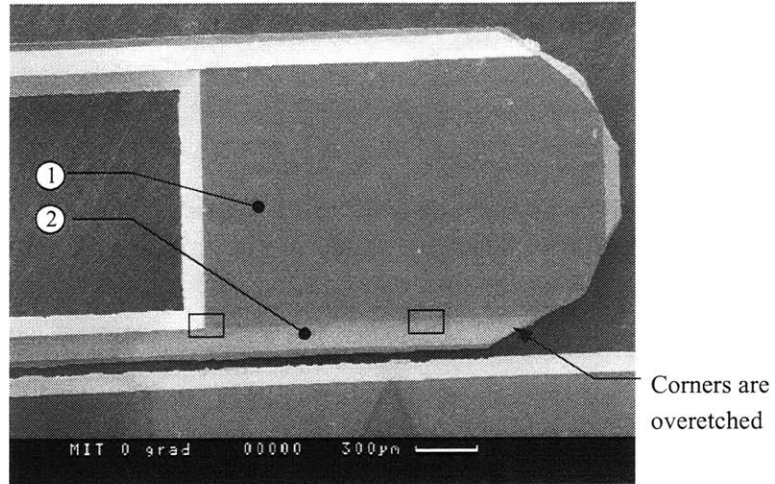
Figure 4-9: SEM picture of the KOH etched contact.
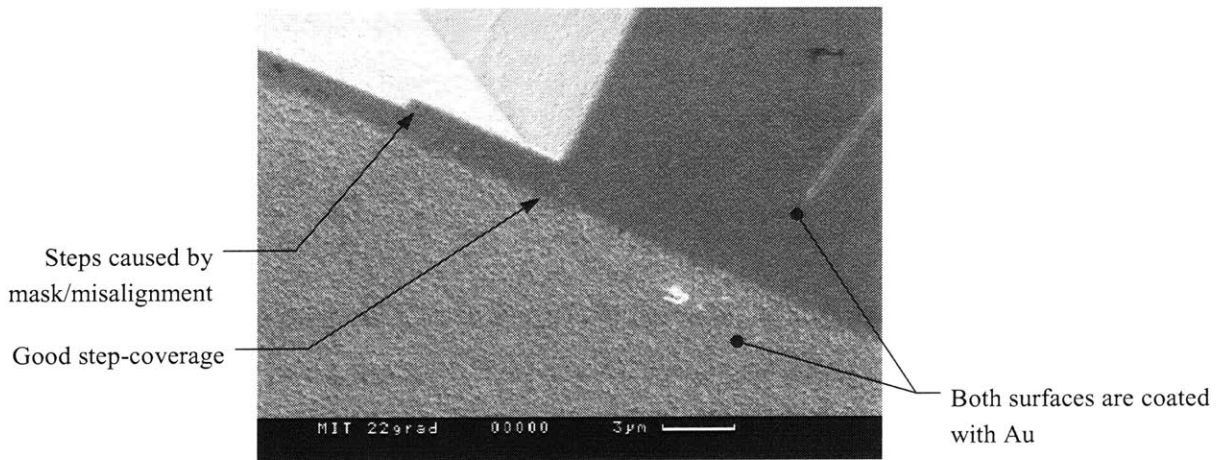
Figure 4-10: SEM picture of the KOH etched contact. This picture shows good metal step coverage and smooth surfaces.
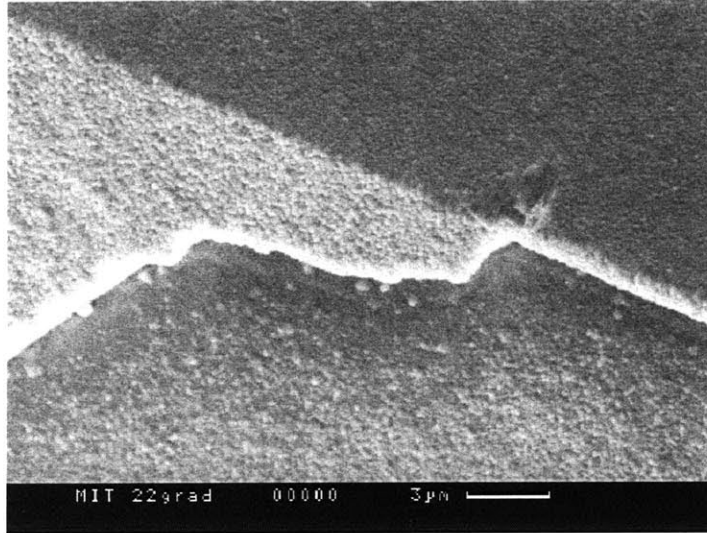
Figure 4-11: SEM picture of the KOH etched contact. This picture shows the step recess on {111} surfaces caused by misalignment to the (110) flat or low mask resolution.

Au layer thickness

The Au layer thicknesses on surfaces (1) and (2) are measured with the same setup shown in Figure 4-3. The measurement results $h_{1,Au} = 0.65$ μm and $h_{2,Au} = 0.48$ μm.

Step coverage

Figure 4-9 shows an SEM top view of the structure and the contact surfaces (2) and (3). Figure 4-10 is the zoom-in view of the gold coated corners. As can be seen, the step corner is covered smoothly. Figure 4-14 shows the cross section view of the flexure beam and Surfaces (2) and (5) are shown here as two smooth edges.

Contact resistance

Experiments have been conducted to measure the contact resistance between surfaces (1) and (4). The setup is shown in Figure 4-13. Two probes were added on the front side and two on the back side. A fifth probe was used to push the contact until it touches the silicon base. The contact force was not measurable here since the contact force is very small compared to the flexure spring force. However, 1 mN is enough to
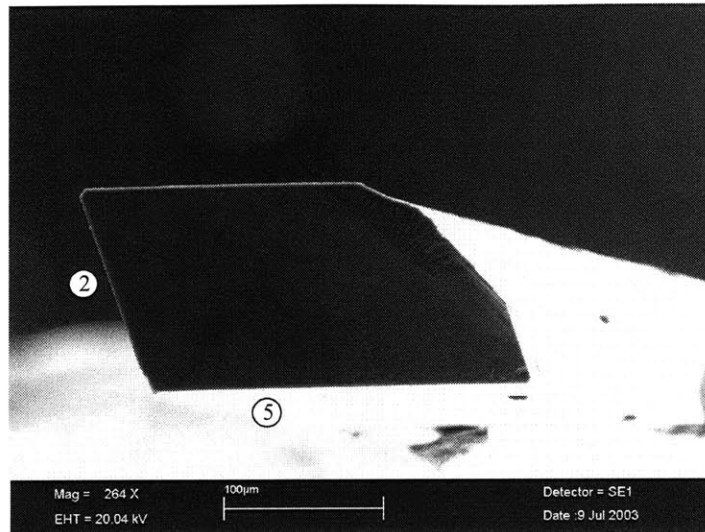
Figure 4-12: SEM picture of the cross section of the flexure beam as shown in Figure 4-8. (2) and (5) show cross section of the two surfaces (2) and (5) in Figure 4-16

achieve contact reistance as low as 1 mΩ on gold-gold surfaces. Three different dies were tested and the average contact resistance was 50 mΩ, compared to 500 mΩ in [25] and about 1 Ω in [26].

Misalignment

Figure 4-11 is the SEM picture of surface (2). A recess is observed that is believed due to the mask and/or misalignment to wafer (110) flat. This may cause a substantial increase of contact resistance and must be resolved for final devices. The low resolution transprency mask can be replaced with an e-beam mask with sub-micron resolution. In aligning with the wafer (110) plane, the wafer flat that is aligned to the wafer (110) with an error of +/- 1.5° is no longer sufficient. One method [64] [65] is to briefly etch an alignment fork that can be used to determine the misalignment of the mask used. The alignment forks are then used for aligning a subsequent mask into the correct crystallographic direction to etch the devices. Another method is to place just a drop of KOH on a wafer, and this will etch a pyramid, which then identifies the {111} planes.

106

a)   b)
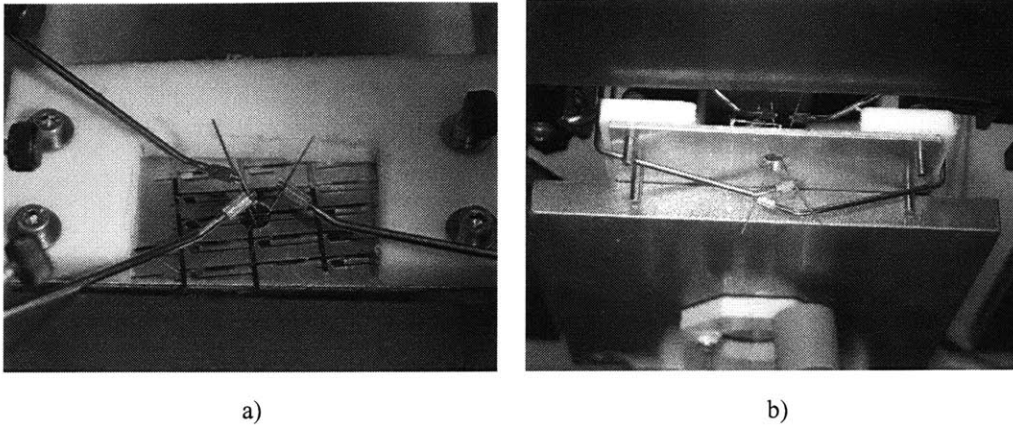
Figure 4-13: 4-point measurement setup. a) shows the probes on top side and b) shows the probes on the backside. This setup and the measurement are carried out at ABB Research.

Front-to-back offset d_k

Figure 4-14 shows SEM picture of a device cross section that has smaller front-to-back offset d_k. As discussed in Section 4.2.3, one sharp corner is formed. This sharp corner can be diminished with longer etching.

4.2.5   Proposed fabrication process

Sputter Au with shadow wafer

In the measurement described in Section 4.2.4, and as shown in Figure 4-13, two probes contact surfaces (1) and (4) from the front and back sides. When building the real device, however, the backside will be bonded to a pyrex wafer and it would be more convenient to have two contact pads on one side. A shadow wafer can be used to pattern the gold as shown in Figure 4-15a. When the two surfaces are brought together, current flows through two corners and two contacts and back to the front surface. This would enable the testing only from front side. However, the contact resistance would increase with the increased number of contact surfaces and corners.
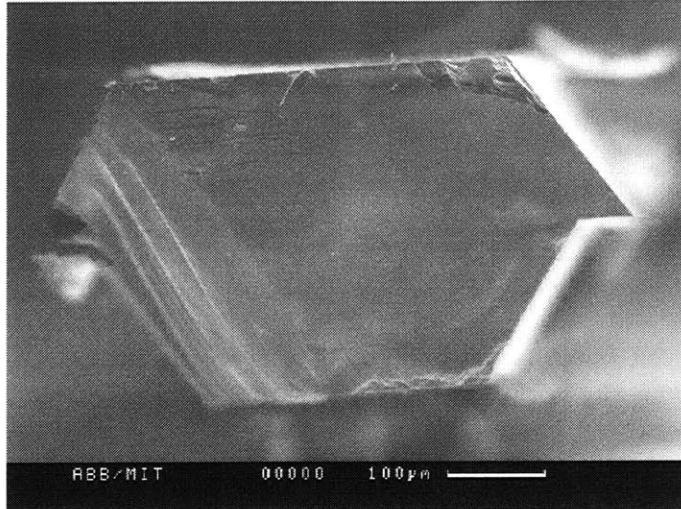
Figure 4-14: SEM picture of a device resulted from smaller off-set in alignment as shown in Figure 4-7.

Gold is patterned
using shadow mask

a)   b)
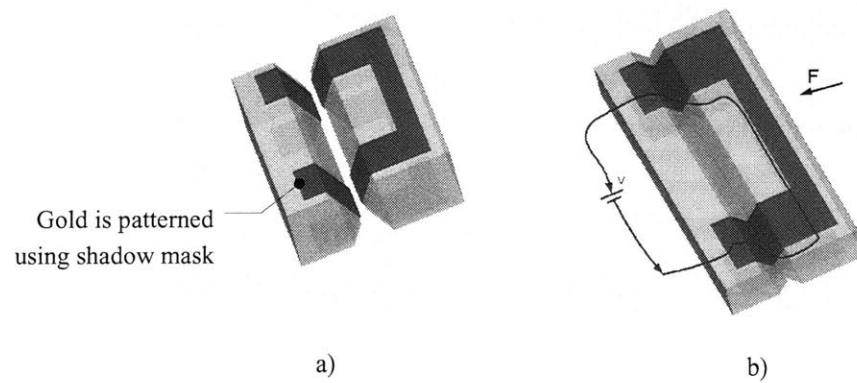
Figure 4-15: pattern gold on the contacts to avoid complicated setup as shown in 4-13.

Relay with zipping actuaors and the KOH-etched contact

A process flow shown in Figure 4-16 can be used to fabricate a {111} contacts MEMS relay actuated by an electrostatic actuator As shown in Figure 4-16, the actuator and bistable relay beam are first defined using DRIE. A thin nitride is then deposited as both insulation layer and KOH etch mask. The contacts are patterned using two shadow masks and etched in KOH. Metal is finally sputtered onto the surfaces to create low resistance contacts.

Starting substrate: 4"
DSP <100> Si Wafer

Spin and pattern 10 m
of photoresist

DRIE etch through

Strip photoresist in
Piranha, RCA clean

Deposit 0.15 m of
silicon nitride

Etch nitride using
shadow wafer

KOH etch

Open Electrode

Contacts   *Bistable Relay Beam*

Metalization
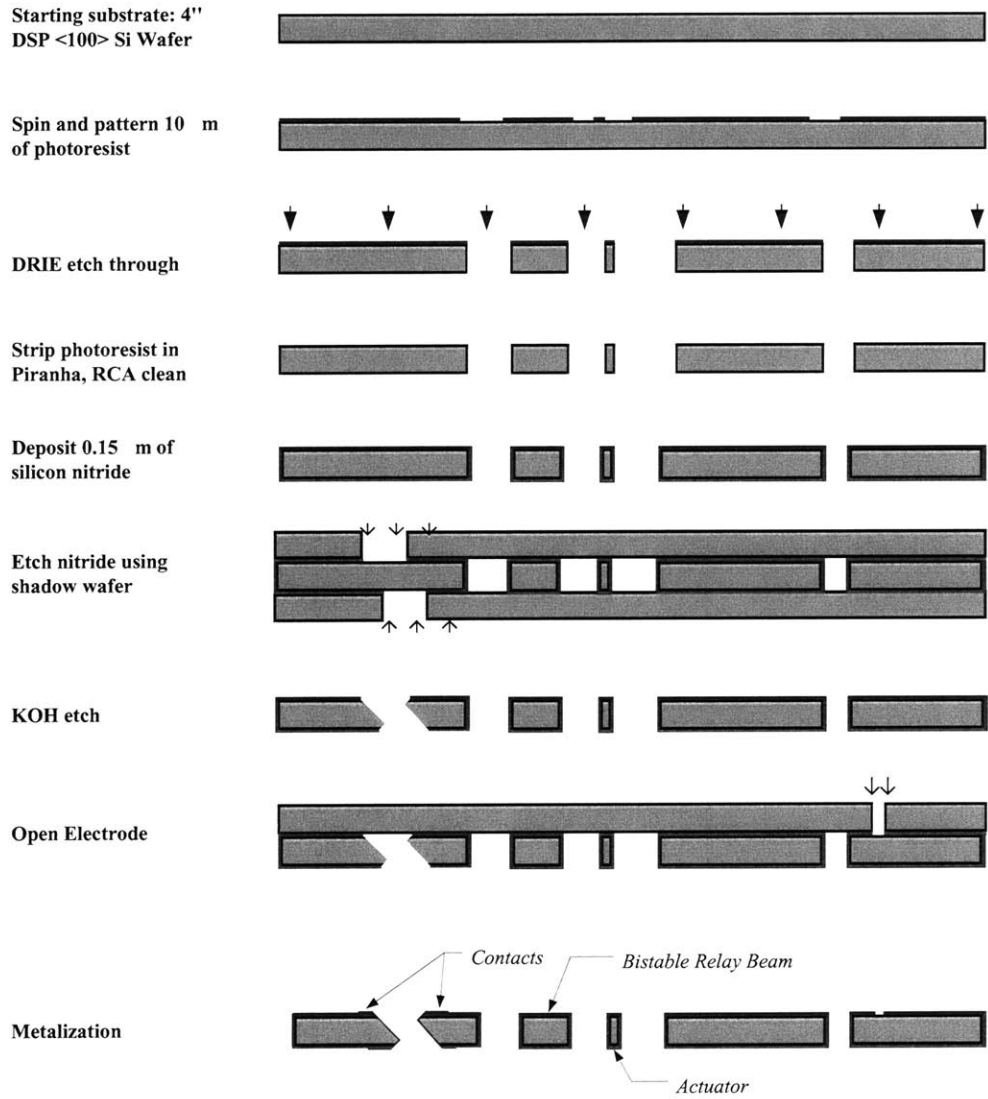
Actuator

Figure 4-16: a process to combine KOH etched contacts and DRIE etched relay.

Chapter 5

Other Applications of the Zipping Actuator

This chapter describes other applications of the zipping actuator. Section 5.1 presents a MEMS valve that utilizes a zipping actuator to switch high pressure fluids. Section 5.2 presents a nonlinear hardening spring by deflecting a flexure beam on a fixed countoured platform.

5.1 A MEMS valve using zipping actuator and compliant starting zones

In addition to in-plane MEMS actuators, the compliant starting zone can also be applied to vertically moving MEMS devices such as micro valves. Figure 5-1 shows a schematic view of a MEMS valve that utilizes a starting zone. The valve plate is sandwiched in between two electrodes and a valve seat is built on the bottom electrode. When the valve is electrified with respect to the top electrode, the electrostatic force easily pulls in the valve plate over a gap distance, as shown in Figure 5-2. The actuator cantilver can then zip along the top electrode and switch the load coming from pressure difference ΔP [66].

In some cases, the gap distance between the top electrode and the valve plate is

111
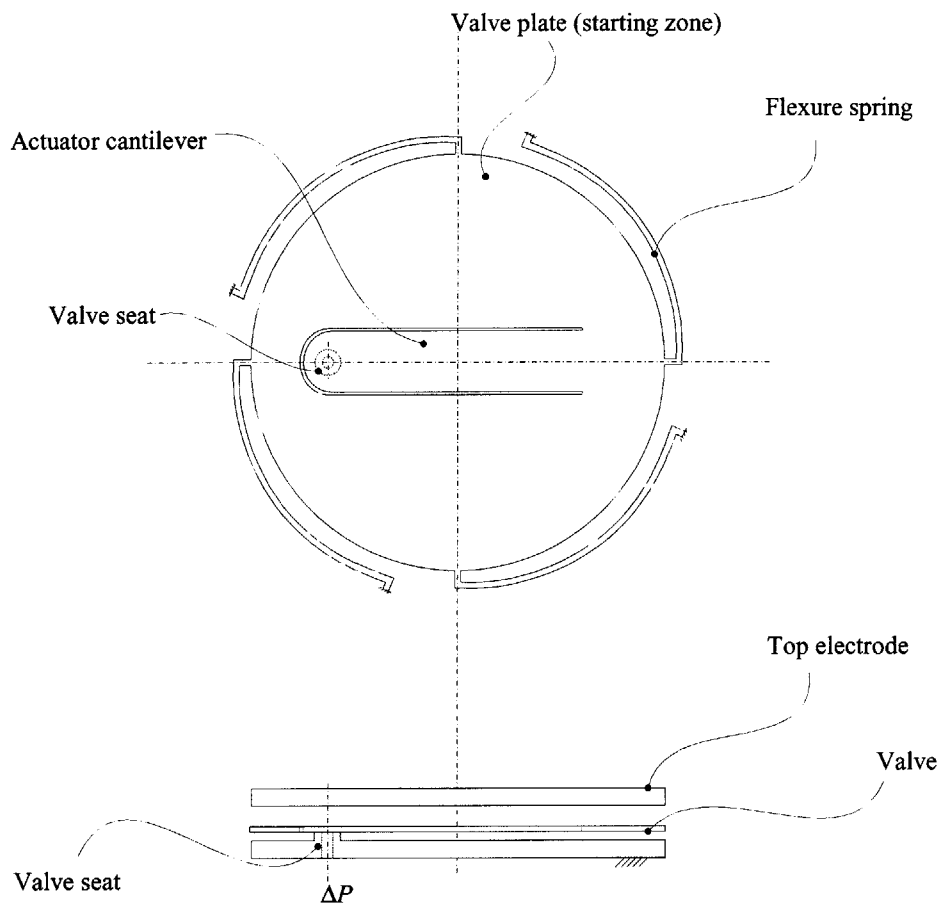
Figure 5-1: top view of a MEMS valve using zipping actuator and compliant starting zones.
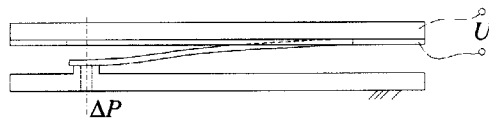
Figure 5-2: cross section view of the MEMS valve shown in Figure 5-1.
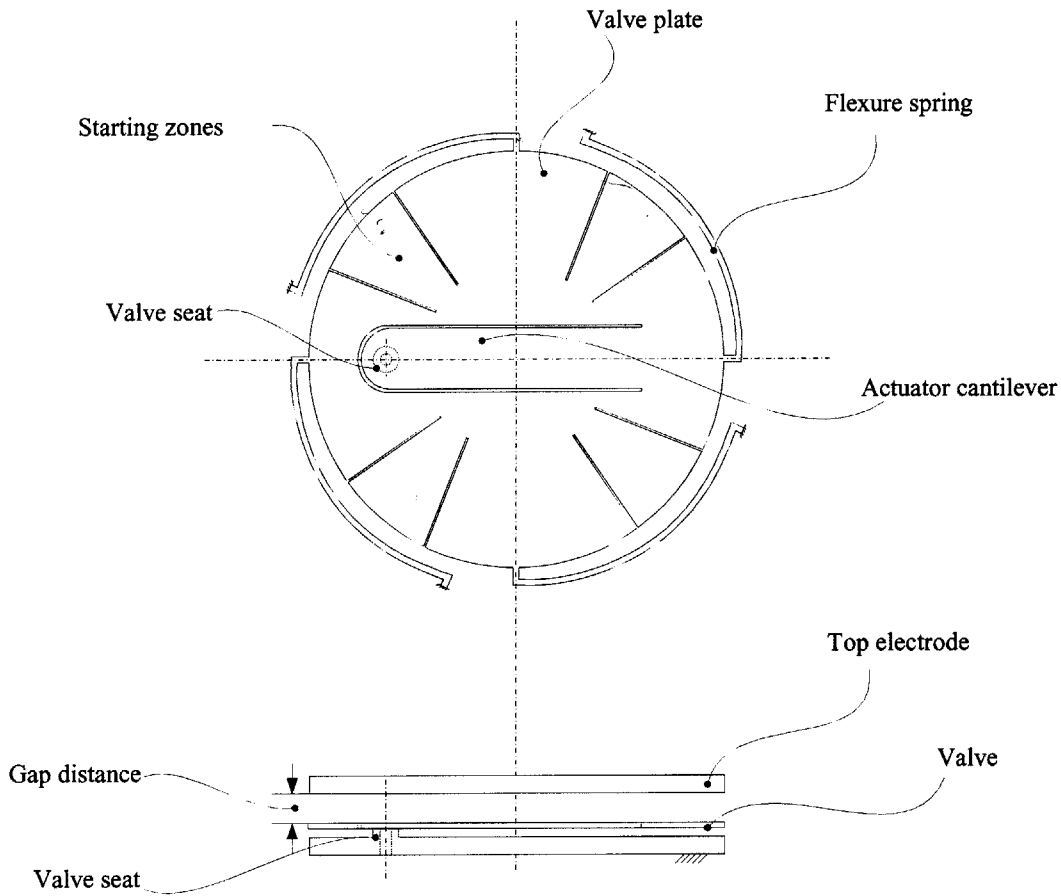
Figure 5-3: top view of a MEMS valve using zipping actuator and more compliant two-stage starting zones.

necessarily very large. To initially pull in the actuator cantilever to the top electrode, more compliant starting zones can be designed by using two or more stages. One of the configurations is shown in Figure 5-3. As a voltage U is applied between the valave plate and the top electrode, the compliant starting zones are first pulled-in to and then zips along the top electrode, lifting up the valve plate and then pulling-in the actuator cantilever.

The analytical and numerical methods described in Chapter 2 can also be applied to the vertically moving zipping actuators. For example, one device are analyzed in [66] using the analytical method in this thesis for calculating actuation force and pull-in voltages.
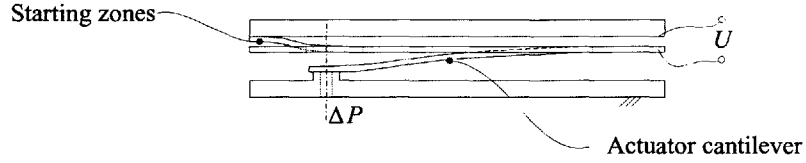
Figure 5-4: cross section view of the MEMS valve shown in Figure 5-3.

5.2 A nonlinear spring

The zipping effect can also be employed to design nonlinear springs. As shown in Figure 5-5, one beam is clamped at the left end while the right end zips along a curved support surface. As the right end moves down, the departure point moves to right and the stiffness of the beam increases. To calculate the stiffness of the beam, the bending equation is first written as:

$$EIy''(x) = N_s(x - s) + M_s \quad s \leq x \leq L \tag{5.1}$$

The compatibility condition

$$y(s) = c(s), \ y'(s) = c'(s), \ y''(s) = c''(s) \ and \ y'(L) = 0 \tag{5.2}$$

and the equillibrium

$$N_s - F = 0 \tag{5.3}$$

$$M_s - M_L - F(L - s) = 0 \tag{5.4}$$

To normalize the equation, let

$$Y = \frac{y}{h}, \ \lambda = 1 - \frac{s}{L} \ and \ X = \frac{\frac{x}{L} - (1 - \lambda)}{\lambda} \tag{5.5}$$

Substitue 5.5 and 5.5 into 5.1

$$EIY''(X)\frac{h}{L^2\lambda^2} = F\lambda LX + M_s \quad 0 \leq X \leq 1 \tag{5.6}$$

114

(a)

(b)
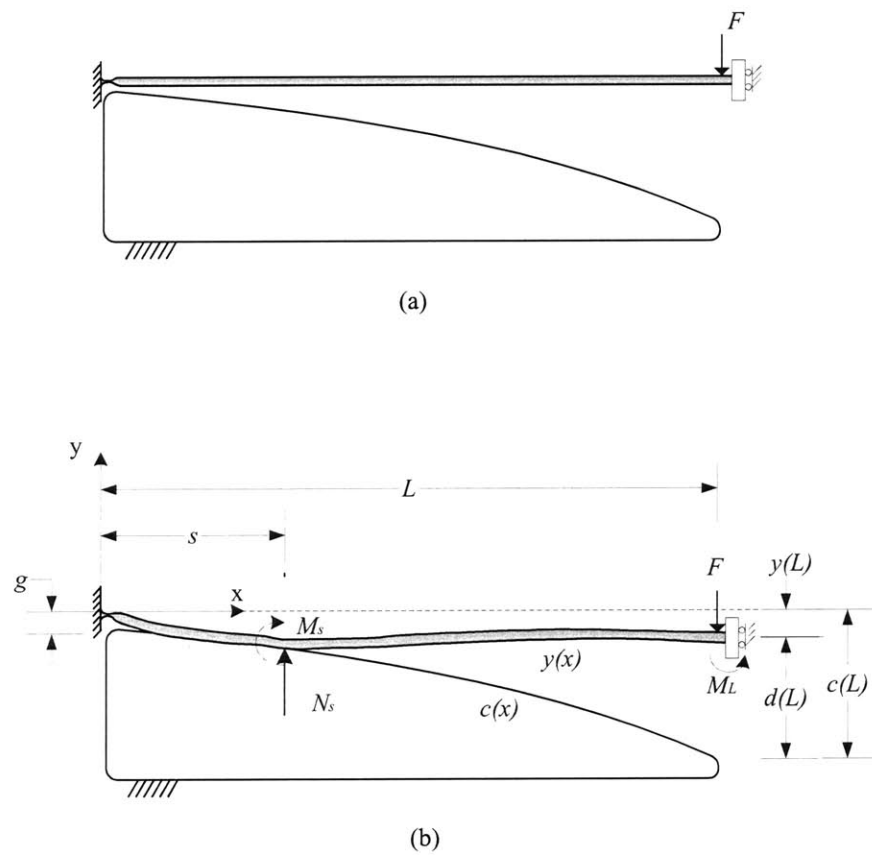
Figure 5-5: a nonlinear spring that utilized zipping beam on a curved support suface.

with boundary conditions

$$Y(0) = C(0), \ Y'(0) = C'(0), \ Y''(0) = C''(0), \ Y'(1) = 0 \tag{5.7}$$

5.6 and 5.7 imply that

$$Y''(X) = \frac{FL^3\lambda^3}{EIh}X + C''(0) \tag{5.8}$$

Integrate Equation 5.8 with respect to X using boundary conditions 5.7

$$Y'(X) = \frac{FL^3\lambda^3}{2EIh}X^2 + C''(0)X + C'(0) \tag{5.9}$$

Substituting Y'(1)=0 into Equation 5.10 yields

$$\frac{FL^3\lambda^3}{2EIh} = -(C''(0)X + C'(0)) \tag{5.10}$$

which together with Equation 5.10 leads to

$$Y'(X) = -[C''(0) + C'(0)]X^2 + C''(0)X + C'(0) \tag{5.11}$$

Integrating Equation 5.11 with respect to X, given $Y(0) = C(0)$ in Equation 5.7, yields

$$Y(X) = -\frac{[C''(0) + C'(0)]}{3}X^3 + \frac{C''(0)}{2}X^2 + C'(0)X + C(0) \tag{5.12}$$

Assume the shape function of the platform is

$$c(x) = a_2x^2 + a_1x + a_0 \tag{5.13}$$

Next, normalize Equation 5.13 by Equation 5.5

$$C(X) = \frac{a_2L^2}{h}[\lambda X + (1 - \lambda)]^2 + \frac{a_1L}{h}[\lambda X + (1 - \lambda)] + \frac{a_0}{h} \tag{5.14}$$

116

and

$$\begin{cases} C(0) = \frac{a_2 L^2}{h}(1-\lambda)^2 + \frac{a_1 L}{h}(1-\lambda) + \frac{a_0}{h} \\ C'(0) = \frac{2a_2 L^2}{h}\lambda(1-\lambda) + \frac{a_1 L}{h} \\ C''(0) = \frac{2a_2 L^2}{h}\lambda^2 \end{cases} \qquad (5.15)$$

Equation 5.12 implies that

$$Y(1) = -\frac{C'(0) + C''(0)}{3} + \frac{C''(0)}{2} + C'(0) + C(0) = \frac{C''(0)}{6} + \frac{2C'(0)}{3} + C(0) \quad (5.16)$$

Next, substitute 5.15 into 5.16

$$Y(1) = -\frac{2a_2 L^2 + a_1 L}{3h}\lambda + \frac{a_2 L^2 + a_1 L + \frac{2}{3}a_2 L + a_0}{h} \qquad (5.17)$$

To determine $Y(1)$, we need to calculate λ, which can be derived from Equations 5.10, 5.11 and 5.15 using

$$\frac{FL^3\lambda^3}{2EIh} = -[C''(0) + C'(0)] = -(\frac{2a_2 L^2}{h} + \frac{a_1 L}{h})\lambda \qquad (5.18)$$

so that

$$\lambda = \sqrt{-\frac{2EI(2a_2 L + a_1)}{FL^2}} \qquad (5.19)$$

Now, substitute 5.19 into 5.16

$$Y(1) = -\frac{2a_2 L^2 + a_1 L}{3h}\sqrt{-\frac{2EI(2a_2 L + a_1)}{FL^2}} + \frac{a_2 L^2 + a_1 L + \frac{2}{3}a_2 L + a_0}{h} \qquad (5.20)$$

The dimensional displacement at $x = L$ is

$$y(L) = Y(1)h = -(2a_2 L^2 + a_1 L)\sqrt{-\frac{2EI(2a_2 L + a_1)}{FL^2}} + a_2 L^2 + a_1 L + \frac{2}{3}a_2 L + a_0 \quad (5.21)$$

The gap between the beam and the support at the right end is then

$$d(L) = y(L) - c(L) = -(2a_2 L^2 + a_1 L)\sqrt{-\frac{2EI(2a_2 L + a_1)}{FL^2}} + \frac{2}{3}a_2 L \qquad (5.22)$$

117

It is therefore possible to design a nonlinear hardening spring using Equation 5.22. By changing the parameters of the curved support platform and the spring beam, the force-displacement curves can be modified to fit for different applications.

Chapter 6

Summary, Conclusions and Suggestions for Future Work

This chapter presents the summary, conclusions and suggestions for future work for this thesis. Section 6.1 briefly describes the research. Section 6.2 then addresses major contributions and what is learned through the thesis. Finally, Section 6.3 suggests the future work that can be done for improvement and continuaity for this thesis.

6.1 Summary

This thesis has developed DRIE-etched zipping actuators that are built into a MEMS relay system. Chapter 1 first addresses the background of MEMS and MEMS actuators in Section 1.1. The motivation and goal of this thesis is next described in Section 1.2. Section 1.3 then overviews the relay developed in this theis by briefly describing its objectives, operation and performance. A KOH-etched relay contact is also presented in Section 1.3 that can achieve low contact resistance for laterally-moving MEMS relays.

Chapter 2 focuses on the design and modeling for both the actuators and the relay system. Section 2.1 introduces electrostatic actuators in detail and compares three kinds of common actuators: comb drive, parallel plate and zipping actuators. It is concluded that zipping actuators are the best candidate for the relay. Section 2.2

then explores the historical background of zipping actuators and addresses the high pull-in voltage problem for the DRIE-etched laterally-moving zipping actuators. A compliant starting cantilever is then designed into the actuator to reduce the pull-in voltage from 250 V to approximately 70 V. Section 2.3 next presents the modeling of the actuator-relay system. In order to design the actuator more accurately, numerical method is first developed in Section 2.3.1 to calculate the pull-in voltage and force-displacement curves for the actuator. Analytical method is also developed in Section 2.3.2 by approximately linearizing the electrostatic force. Optimization of the relay system is then performed in Section 2.3.4 by modulating the relay beam thickness and reducing the push/pull force ratio from 2.5:1 to 1.5:1.

Chapter 3 describes the fabrication and measurement of the actuator-relay system. Fabrication process flow is given in Section 3.1 and the fabrication results are presented in Section 3.2. Section 3.3 shows static and dynamic measurement results. The pull-in voltage is measured to be 75 V and the actuation voltage is 140 V. More than 40 million cycles are achieved without any stiction or fracture fatigue.

In Chapter 4, laterally-moving micro relay contacts are discussed. DRIE-etched relay contacts are first introduced and the contact resistance is measured in Section 4.1 to be approximately 1 Ω. Section 4.2 then presents the contacts created using wet anisotropic KOH etching, which results in slanted and smooth contact surfaces. Experimental devices are then designed and fabricated, and the resistance is measured to be approximately $50m\omega$. Section 4.2.3 discusses fabrication issues. In Section 4.2.5, a process plan is proposed to combine the KOH-etched relay contacts and the DRIE-etched actuator-relay system.

Chapter 5 explores other applications of zipping actuators. In Section 5.1, the concept of compliant starting zone is applied to vertically-moving zipping actuators, and a micro valve is designed using these actuators that can achieve high force and large stroke. Section 5.2 designs a nonlinear hardening spring that utilizes a bendable beam zipping along a curved support platform, and force-displacement equations are derived.

6.2 Conclusions

The design, analysis, fabrication and measurement of DRIE-etched electrostatic zipping actuators and a MEMS relay have been presented. The major contributions of this thesis are discussed as follows.

By reducing the pull-in voltage from 250 V to approximately 70 V, a compliant starting zone is shown to greatly improve the performance of zipping actuators used for driving high load MEMS devices. Such designs open up many new possibilities for electrostatic actuators such as 3-dimensional MEMS zipping electrostatic devices. For example, by using 2-stage compliant starting zone, a MEMS valve is designed that can theoretically switch fluid of up to 1×10^7; Pa.

To model the actuator, numerical and analytical methods are developed for solving the force-displacement characters of the actuators and both agree well with each other. The numerical method accurately solves the electrostatic zipping actuator problem by normalizing the beam bending equation and eliminating the moving boundary problem. The analytical method offers better understanding of the influence of different parameters such as the actuation force being proportional to $U^{2/3}$, which greatly improves the design process and makes it possible to optimize the actuator performance.

By modulating the relay beam thickness and thus optimizing its free eigenvalues ratio τ_2/τ_0, the relay push/pull force ratio is decreased from 2.5 : 1 to approximately 1.5 : 1. The actuation effort is therefore saved by approximately 40% to achieve a similar contact force.

A MEMS relay is then designed using the optimized bistable relay beam and two zipping actuators with compliant starting cantilevers. Electrodes are designed such that the actuators can both push and pull the relay beam.

The actuator-relay system is fabricated using DRIE in silicon wafer and then anodically bonded to a pyrex substrate. Only one mask is used to define the devices. In addition, inexpensive and quick-turnaround transparency masks are utilized in this thesis for critical features. To overcome the low resolution of transparency mask, the features are printed 10× and a 10:1 reduction stepper is used later to expose the

wafer. These features greatly simplify the fabrication process and lower the cost.

Both static and dynamic measurements are performed on the DRIE-etched relay. The initial pull-in voltage of the actuator is measured to be 75 V. Both actuators provide up to 10 mN over their 80 μm of stroke at 140 V. The relay achieves a contact force of approximately 1.8 mN. These results confirm theoretical expectations based on numerical, analytical and FEA, after accounting for fabrication variations. Stiction caused by charge leakage can be a problem for unipolar driven contact mode actuators and it is also observed on the zipping actuators in this thesis. Separate poles can be used to avoid the stiction but the fabrication process is more complex. This thesis then developed a bipolar drive by which the relay is operated at 100 Hz for over 120 hours through more than 40 million cycles without any observed stiction or fracture fatigue. The shortest pulse required to switch the relay is measured to be 400 μs. It is then also possible to use very short voltage pulses to drive the device, because the accumulated charge that creates the stiction is proportional to the contact time.

DRIE-etched relay contacts is next designed, fabricated and tested. It is found that metal sputtering has a higher efficiency than evaporation for depositing metal on DRIE-etched vertical contact surfaces. However, even using sputtering, the ratio of metal thickness on sidewalls versus on top surfaces is approximately 1:9, which makes it difficult to achieve low contact resistance through laterally-moving relays. In this thesis, the contact resistance is measured to be approximately 1 Ω. A new micro relay contact using wet anisotropically etched Si {111} surfaces is then designed to achieve lower contact resistance. Fabrication issues are discussed and experimental devices are fabricated. The ratio of metal thickness on sidewall versus on top surface is measured to be approximately 1:1.3 and the contact resistance is approximately 50 $m\Omega$, 20 times less than that achieved by DRIE. Fabrication errors caused by misalignment are also observed, and briefly-etched alignment forks are proposed to avoid the misalignment.

One nonlinear hardening spring is designed that utilizes a flexible beam zipping on a curved platform support. It is found that the beam stiffness increases as it zips along. Analytical methods are developed based on the zipping actuator analyses and

closed-form force-displacement equations are derived. According to the equations, both the zipping beam and the shape of the support platform influence the spring stiffness and hence it is possible to design nonlinear hardening springs with desired stiffness characteristics, by changing these parameters.

6.3 Suggestions for future work

6.3.1 Optimization of the actuator

The actuator performance may be optimized. To do this, the pull-in voltage can be calculated using numerical method described in Section 2.3.1 and must be kept lower than the required actuation voltage. The force-displacement can then be calculated using Equation 2.42 and optimized by changing the relevant parameters as discussed in Section 2.3.3. For example, different insulation layer materials may be considered according to their dielectric strength and relative permittivitty, and the best material can be selected in order to maximize the actuation force. Moreover, it is discussed in Section 2.3.3 that the actuation force is larger if using a thicker insulation layer and the highest allowable actuation voltage. Therefore, it is possible to get higher force by increasing the insulator thickness with a reasonable process time and use a higher actuation voltage.

6.3.2 Actuator array

Since the width of the zipping actuator is very small. (on the order of 200 μm.) It is possible to stack the actuators and get higher force for the same stroke. Moreover, when stacking the actuators, only one set of click-off tabs for the whole device is needed. This would decrease the device volume further and achieve higher energy density.

6.3.3 Dynamic characteristics of the actuator

As discussed in Section 2.3.6, the dynamic characteristics of the actuator may be calculated using numerical methods. In order to analyze the dynamic property of the full actuator-relay system, the relay beam and the contact may also be included in the model.

6.3.4 Full relay

Since it is difficult to achieve low contact resistance using DRIE-etched vertical sidewalls, KOH-etched contacts may be incorporated with the DRIE-etched relay. A process plan is suggested in Section 4.2.5. For fabrication of the full relay, high-quality electron beam mask must be used in order to achieve high resolution. In addition, pre-etched alignment features must be used for KOH etching to determine the $\langle 110 \rangle$ flat.

The relay may also be packaged by anodically bonding the device to pyrex substrates on both sides in order to 1) avoid contamination and hence reduce arcing problem during switching and 2) secure a vacuum environment for the relay and thus achieve higher switching speed and higher breakdown voltage.

6.3.5 More applications

The zipping actuators designed in this thesis may be applied to other areas. One example is the optical fiber aligner that requires a force of millinewtons to newtons and a large stroke on the order of sub-millimeters, which are very challenging for surface-micromachined MEMS actuators. However, by stacking several DRIE-etched zipping actuators designed in this thesis, the optical fiber aligner may be fabricated with a resonable volume on the order of $6mm \times 6mm \times 1mm$.

Another example is high load MEMS valves. Using zipping actuator with compliant starting zones, a design has been given in Section 5.1 that can theoretically switch high pressure fluid. More sophisticated devices may also be designed and fabricated.

Nonlinear hardening springs are very useful in many areas. Closed-form force-displacement equations for a beam zipping along a curved support platform are developed in this thesis, and can be used for designing such springs. In the future, general theories for zipping and/or peeling effects may be developed and applied for designing more and more beneficial products.

Appendix A

MATLAB Script for Solving Multi-component Actuator Before Pull-in

The MATLAB script presented in this appendix is used in Section 2.3.1 to compute the pull-in voltage and the force-displacement characteristics for the multi-component actuator before it is pulled in.

```
% for a constant thickness beam.
% Two beams
% x-----L1---------|------------L2-------|
% ------L3=L1----|||||||||||||
%                         |||||||||||
%                           |||||||||
%                             |||||||||
%                               |||||||||
%this routine outputs the solution at a given voltage without zippering
%% parameters                                                        10
global Delta;
global Delta2;
```

```
global Gama1;
global Gama2;
global Gama3;
global L1;
global L2;
global L3;
global beta;
global yi;
global t0;
global x0;
global gap; %minimum gap 15um
save=1;
E=160e9;    %Pascals
Ebs0=8.85e-12; %F/m
Ebs1=3.8*Ebs0;
w=0.3e-3;   %0.5mm
h=20e-6;   %20um, actuator cantilever thickness
h3=15e-6 %Starting cantilever
L1=1.5e-3;   %1.5mm
L2=3e-3;
L3=L1;
h0=0.4e-6;          %0.4um
w0=80e-6;    % maximum gap
gap=10e-6; %15um of gap
beta=Ebs0/Ebs1*h0/h;
Delta=w0/h;  % equilibrium height of spring
gap=gap/h;
% initial voltage, lambda...
v0=1
t0=ones(100,1);
```

```matlab
x0=linspace(0,1);

yi=x0*0;

% generate an intial solution at a fixed voltage with fixed
% beam thickness
for i=1:30
    U(i)=v0       %volts
    Gama1=6*Ebs0*(U(i))^2*L1^4/E/h^6;
    Gama2=6*Ebs0*(U(i))^2*L2^4/E/h^6;
    Gama3=6*Ebs0*(U(i))^2*L3^4/E/h^3/h3^3;
    [x,y]=Noncontact3ODE;
    ydum1(i,:)=y(1,:);
    ydum2(i,:)=y(5,:);
    ydum3(i,:)=y(9,:);
    hold on;
    yi=y;
    v0=v0+10;
    plot(x*L1, ydum1(i,:)*h)
    hold on;
    plot(L1+x*L2, ydum2(i,:)*h)
    plot(x*L1, ydum3(i,:)*h)
end


function [xint,Sxint, lambda]=Noncontact3ODE()
global t0;
global Delta;
global Gama;
global beta;
global Omega;
global w0;
global yi;
```

```
global x0;

solinit = bvpinit(linspace(0,1),@mat4init);

sol = bvp4c(@mat4ode,@mat4bc,solinit);

xint = linspace(0,1);

Sxint = bvpval(sol,xint);

function dydx=mat4ode(x,y)

global Delta;

global Gama1;

global Gama2;

global Gama3;

global beta;

global w0;

global t0;

global x0;

global gap;

hx=interp1(x0,t0,x);

dydx=[y(2)
      y(3)
      y(4)
      -Gama1/(y(1)-y(9)+beta)^2/hx
      y(6)
      y(7)
      y(8)
      -Gama2/(y(5)+gap+Delta*x+beta)^2/hx %linear electrode
      y(10)
      y(11)
      y(12)
      Gama3/(y(1)-y(9)+beta)^2/hx]; %linear electrode


function res = mat4bc(ya,yb,lambda)
```

80

90

100

130

```
global gap;
res = [ya(1)
       ya(2)
       yb(1)−ya(5)
       yb(2)−ya(6)
       yb(3)−ya(7)
       yb(4)−ya(8)
       yb(5)
       yb(6)
       ya(11)
       ya(12)
       yb(9)+gap
       yb(10)
    ];

function yinit = mat4init(x)
global la;
global Delta;
global yi;
global gap;
global L1;
global L2;
if abs(yi(1,10))>0
    num=floor(100*x);
    if num < 1
        num=1;
    end
    if num>100
        num=100;
    end
```

```matlab
        yinit=yi(:,num);
    else
    yinit =[   0
        0
        0
        0
        0
        0
        0
        0
        −gap
        0
        0
        0
    ];
end
```

Appendix B

MATLAB Code for Solving Zipping Actuator Problem After Pull-in

The MATLAB script presented in this appendix is used in Section 2.3.1 to compute the force-displacement characteristics of the zipping actuator after pull-in.

```
%To solve the zipper shape and force
%% parameters
global Delta;
global Delta2;
global Gama;
global beta;
global yi;
global t0;
global x0;
global s;
global la;
global w2;
global clamp;
```

```
global hinge;
global first;
global N;
N=500;
clamp=0;
hinge=1;
first=1;
E=160e9;   %Pascals
Ebs0=8.85e-12; %F/m
Ebs1=3.8*Ebs0;
w=0.3e-3;   %0.5mm
h=20e-6;   %10um
L=4.5e-3;   %4.5mm
h0=0.4e-6;          %0.4um
w0=80e-6;    % Maximum gap
w2=0e-6; %Displacement
beta=Ebs0/Ebs1*h0/h;
Delta=w0/h;  % equilibrium height of spring
Delta2=w2/h;
lambda=0.9;
la=lambda;
t0=ones(N,1);
x0=linspace(0,1, N);
beta=Ebs0/Ebs1*h0/h;
yi=x0*0; %Initial solution
clear l;
lambda=0.9;
figure;
for k=1:11
    lambda=0.9;
```

```
global hinge;
global first;
global N;
N=500;
clamp=0;
hinge=1;
first=1;
E=160e9;   %Pascals
Ebs0=8.85e-12; %F/m
Ebs1=3.8*Ebs0;
w=0.3e-3;   %0.5mm
h=20e-6;   %10um
L=4.5e-3;   %4.5mm
h0=0.4e-6;          %0.4um
w0=80e-6;    % Maximum gap
w2=0e-6; %Displacement
beta=Ebs0/Ebs1*h0/h;
Delta=w0/h;  % equilibrium height of spring
Delta2=w2/h;
lambda=0.9;
la=lambda;
t0=ones(N,1);
x0=linspace(0,1, N);
beta=Ebs0/Ebs1*h0/h;
yi=x0*0; %Initial solution
clear l;
lambda=0.9;
figure;
for k=1:11
    lambda=0.9;
```

```matlab
v0=80;
w2=w0*((k−1)/10);
Delta2=w2/h
first=1;
for i=1:10
    U(i)=v0        %volts

    Gama=6*Ebs0*(U(i)/h)^2/E*(L/h)^4;
    [x,y,lambda]=straightElectrodeODE(lambda);
    ydum(k,i,:)=y(1,:);
    hold on;
    l(k,i)=lambda;
    yi=y;
    v0=v0+20;
    plot((x*lambda+1−lambda)*L*1000, y(1,:)*h*1e6);
    hold on;
    lambda2=1;
    z=−Delta*(lambda2*x+1−lambda2);   %straight electrode
    plot((x*lambda2+1−lambda2)*L*1000,z*h*1e6);   %plot the actual electrode
    F(k,i)=−E*t0(N)*1/12*w*h^4/lambda^3/L^3*y(4,N);
    Fdum(k,i)=F(k,i)/Gama^(3/4);
    first=0;
end
end
for k=1:10
    Delta2k(k)=w0*((k−1)/10)/h;
end


function [xint,Sxint,lambda]=StraightElectrodeODE(lambda)
global t0;
```

```matlab
global Delta;
global Gama;
global beta;
global Omega;
global w0;
global yi;
global x0;
global N
solinit = bvpinit(linspace(0,1,N),@mat4init,lambda);
sol = bvp4c(@mat4ode,@mat4bc,solinit);
lambda=sol.parameters;
xint = linspace(0,1,N);
Sxint = bvpval(sol,xint);


function dydx=mat4ode(x,y,lambda)
global Delta;
global Gama;
global beta;
global w0;
global t0;
global dt0;
global ddt0;
global x0;
hx=interp1(x0,t0,x);
dydx=[y(2)
    y(3)
    y(4)
    -Gama*lambda^4/(y(1)+Delta*(lambda*x+1-lambda)+beta)^2/hx
];
```

```
function res = mat4bc(ya,yb,lambda)
global Delta;
global Gama;
global beta;
global Ebsr;
global Delta2;
global clamp;                                                          110
global hinge;
if clamp==1
    res = [  ya(1)+(1-lambda)*Delta
        ya(2)+lambda*Delta
        ya(3)
        yb(1)+Delta2
        yb(2)];
elseif hinge==1
    res = [  ya(1)+(1-lambda)*Delta
        ya(2)+lambda*Delta                                             120
        ya(3)
        yb(1)+Delta2
        yb(3)];
end

function yinit = mat4init(x)
global la
global Delta
global yi
global Delta2                                                          130
global clamp
global hinge
global first
```

137

```
global w0
global h
global N
if abs(yi(1,10))>0 & first==0
    num=floor(N*x);
    if num < 1
        num=1;                                                    140
    end
    if num>N
        num=N;
    end
    yinit=yi(:,num);
else
    if clamp==1
        a=-Delta+Delta2;
        b=2*Delta-2*Delta2;
        c=0;                                                      150
        d=-la*Delta;
        e=-(1-la)*Delta;
        yinit =[  a*x.^4+b*x.^3+c*x.^2+d*x+e
            a*x.^3+3*b*x.^2+d
            12*a*x.^2+6*b*x
          24*a*x+6*b
        ];
    elseif hinge==1
        a=(2*la+3)*(1-la)*Delta-3/2*Delta2;
        b=Delta2/2-(1-la)*Delta;                                  160
        c=0;
        d=-2*la*(1-la)*Delta;
        e=-(1-la)^2*Delta;
```

```
yinit =[  a*x.^4+b*x.^3+c*x.^2+d*x+e
          a*x.^3+3*b*x.^2+2*c*x+d
          12*a*x.^2+6*b*x+2*c
           24*a*x+6*b
        ];
    end
end                                                    170
```

Appendix C

MATLAB Code for Optimizing the Relay Beam

The MATLAB script presented in this appendix is used in Section 2.3.4 to optimize the relay beam push/pull force ratio.

```
%optimization routine
% uses eigenvalue solver
%
% optimizes ratio of lambda2/lambda1


global x0
global N
N=100
x0=0:1/N:1;
```

```
% set up beam thickness
t0=ones(N+1,1);
t0=t0*10;


dt0=deriv(x0,t0); %t0'
```

```
ddt0=deriv(x0,dt0); %t0''

tmin=0.5; %minimum thickness is 1/2 of the initial thickness


for i=1:10 %iteration number                                          20
    tos(i,:)=t0';
    [m,b]=getmatrix(t0,dt0,ddt0);
    [v,d]=eig(m,b);
    [dd,id]=sort(abs(diag(d)));
    %first mode
    yy=v(:,id(3));
    [w1,y1]=getval(yy);
    w1psum=0;


    for j=2:N                                                         30
        w1psum=w1psum+(w1(j+1)-w1(j-1))^2/(x0(j+1)-x0(j-1))/2;
    end


    % second mode
    yy=v(:,id(1));
    [w2,y2]=getval(yy);
    w2psum=0;


    for j=2:N
        w2psum=w2psum+(w2(j+1)-w2(j-1))^2/(x0(j+1)-x0(j-1))/2;        40
    end
    dum=(y1'.^2/w1psum/dd(1)-y2'.^2/w2psum/dd(1)^2*dd(3)).*abs(t0-tmin);
    %checkt=sign(t0-dum/abs(max(dum))*0.05);
    %checkt=max(checkt,0);
    del=dum/abs(max(dum))*0.04;
    t0=t0+del;
```

```
        t0=max(t0,tmin);
        t0=project_vol(t0);
        tt(i,:)=t0';
        cost(i)=dd(3)/dd(1)                                    50
        c1(i)=dd(1);
        w1c(i,:)=w1;
        c2(i)=dd(3);
        w2c(i,:)=w2;
        dt0=deriv(x0,t0);
        ddt0=deriv(x0,dt0);
end


% save solution.
% construct "lowest mode + derivatives"            60
yy=v(:,id(1));
[w0,y0]=getval(yy);


w0p=deriv(x0,w0);
w0ppp=deriv(x0,y0);
w0pppp=deriv(x0,w0ppp);




function [m,b]=getmatrix(t0,dt0,ddt0)

                                                                70

%
%form eigenvalue problem for beam equation
% (Iw'')'' = -T w''
%
% use formulation: y=w'';  (I y)'' +T y= Iy''+2I'y'+I''y+ Ty=0
%
```

```
% number of grid points=N+1
% ordering (w_1,y_1,w_2,y_2,.....w_N,y_N)
global N
```
```
dx=1/N;
x0=0:1/N:1;
m=zeros(2*N+2,2*N+2);
b=m;
% left boundary:  w=w''=0
m(1,1)=1;
%clamp
m(2,2)=-1;
m(2,1)=-2/dx^2;
m(2,3)=2/dx^2;
```
```
b(2,2)=-0;
for i=2:N
    tx=t0(i);
    txp=dt0(i);
    txpp=ddt0(i);
    if i==2
        txpp=ddt0(3);
    end
    if i==N
        txpp=ddt0(N-1);
```
```
    end
    j=2*(i-1)+1;
    b(j+1,j+1)=-1;
    m(j,j)=-2/dx^2;
    m(j,j+2)=1/dx^2;
    m(j,j-2)=1/dx^2;
```

144

```
    m(j,j+1)=-1;

    m(j+1,j+1)=tx*(-2/dx^2)+txpp;

    m(j+1,j+3)=tx/dx^2+txp/dx;

    m(j+1,j-1)=tx/dx^2-txp/dx;                               110

end

j=2*(N)+1

b(j+1,j+1)=-0;

m(j,j)=1;

% clamp

m(j+1,j+1)=-1;

m(j+1,j)=-2/dx^2;

m(j+1,j-2)=2/dx^2;


function dt=deriv(x,t)                                       120


n=size(t,1);

m=size(t,2);

n=max(n,m);

for i=2:n-1

    dt(i)=(t(i+1)-t(i-1))/(x(i+1)-x(i-1));

end

dt(1)=(t(2)-t(1))/(x(2)-x(1));

dt(n)=(t(n)-t(n-1))/(x(n)-x(n-1));

                                                            130

dt(1)=dt(2);

dt(n)=dt(n-1);


function [w,y]=getval(yy)


j=1;
```

```
n=size(yy,1)
for i=1:n/2
    w(j)=yy(2*(i-1)+1);
    y(j)=yy(2*i);
    j=j+1;
end
```

140

Appendix D

Zipping Actuator Masks

The masks presented in this appendix are used for fabricating the zipping actuator-relay system described in Chapter 3.
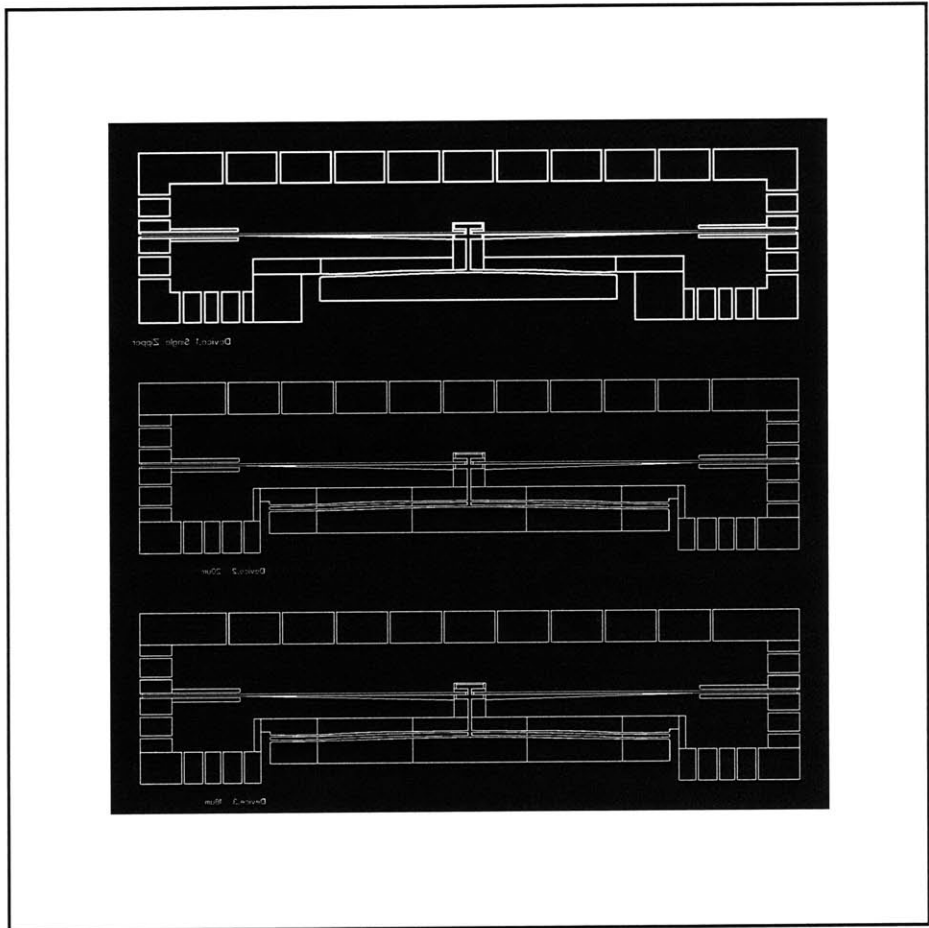
Figure D-1: Device mask
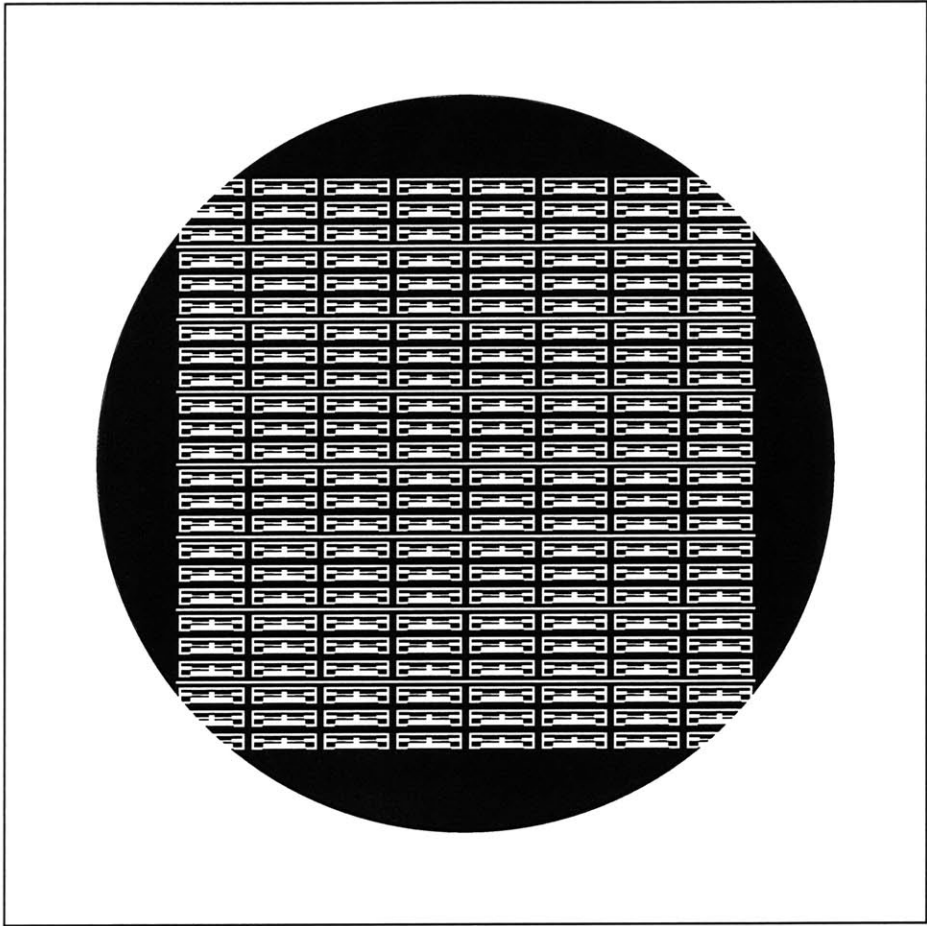
Figure D-2: Handle mask
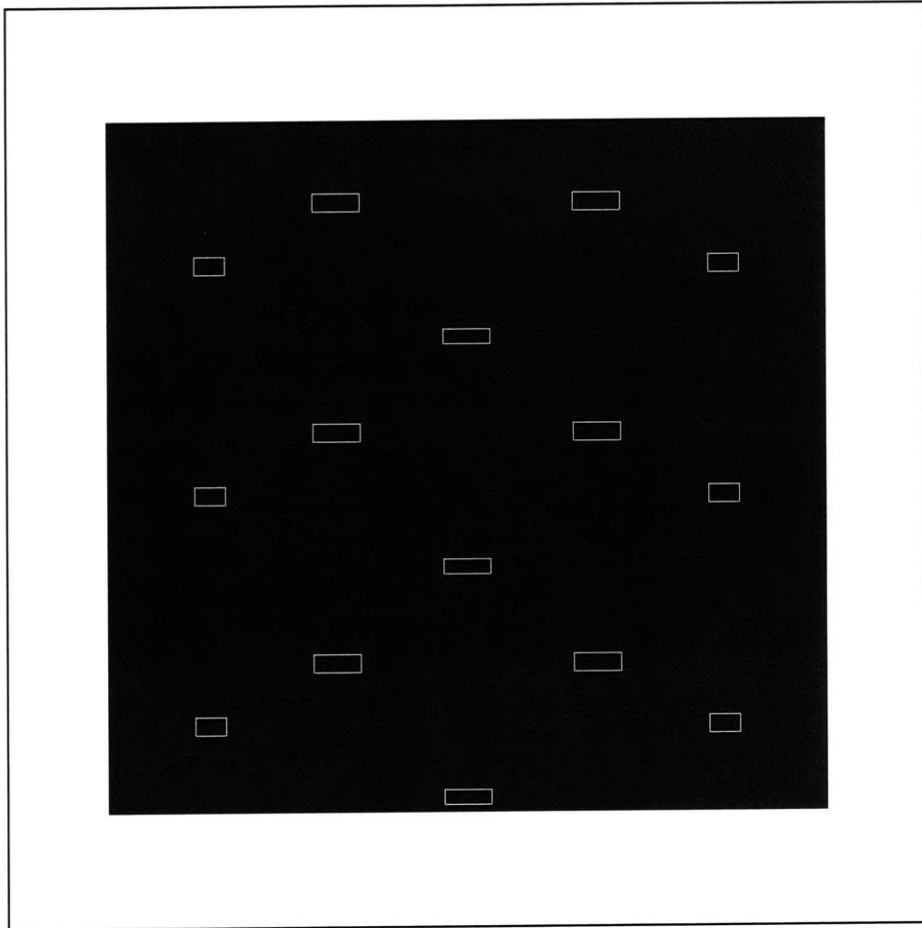
Figure D-3: Shadow mask

Appendix E

Masks for Koh-Etched Relay Contact

The masks presented in this appendix are used for fabricating the experimental KOH-etched relay contacts that are described in Section 4.2.
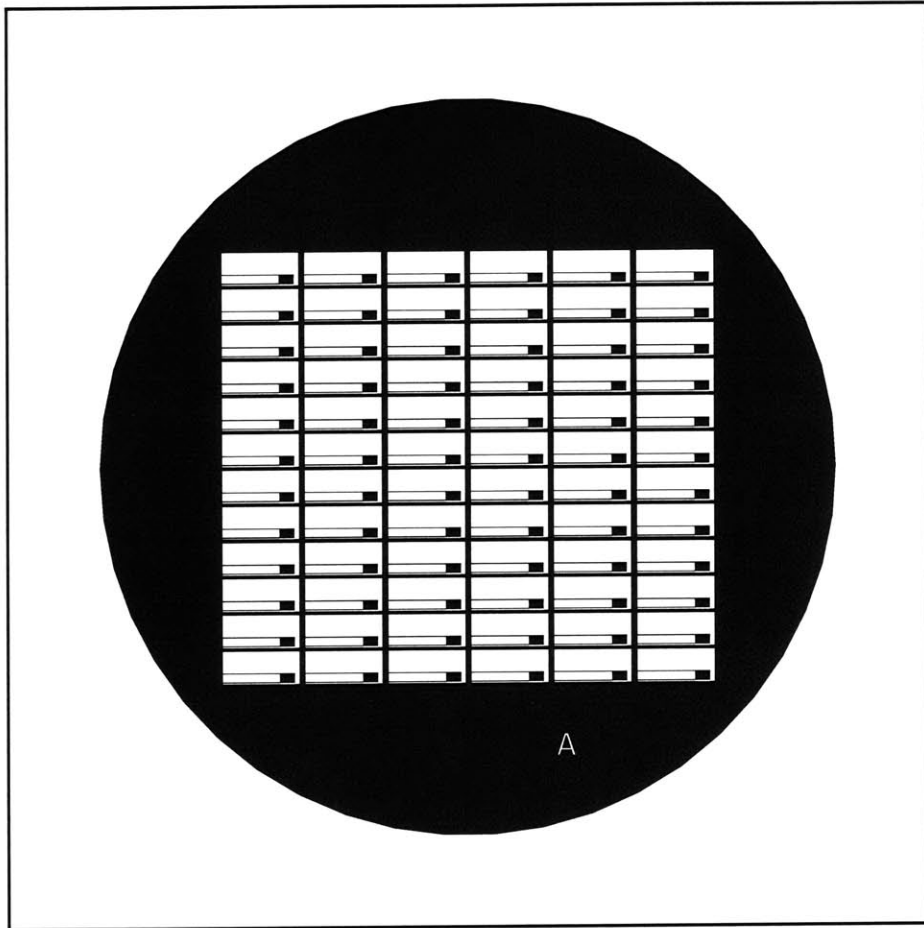
Figure E-1: Front side device mask
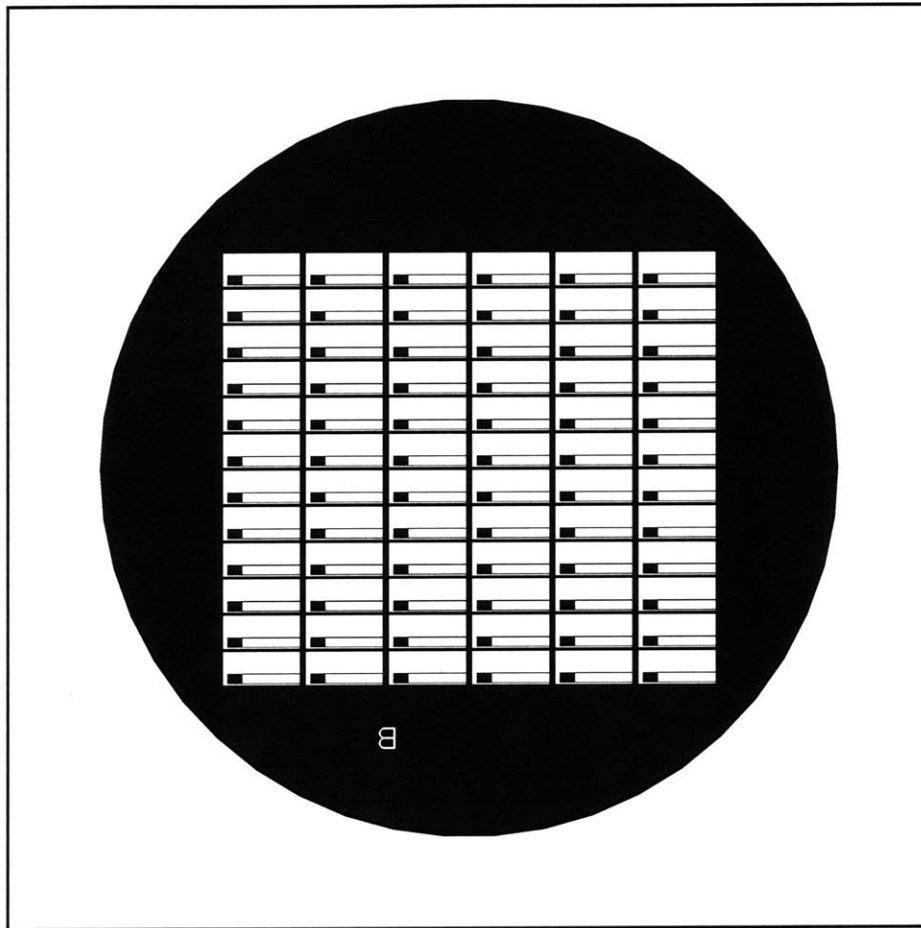
Figure E-2: Back side device mask
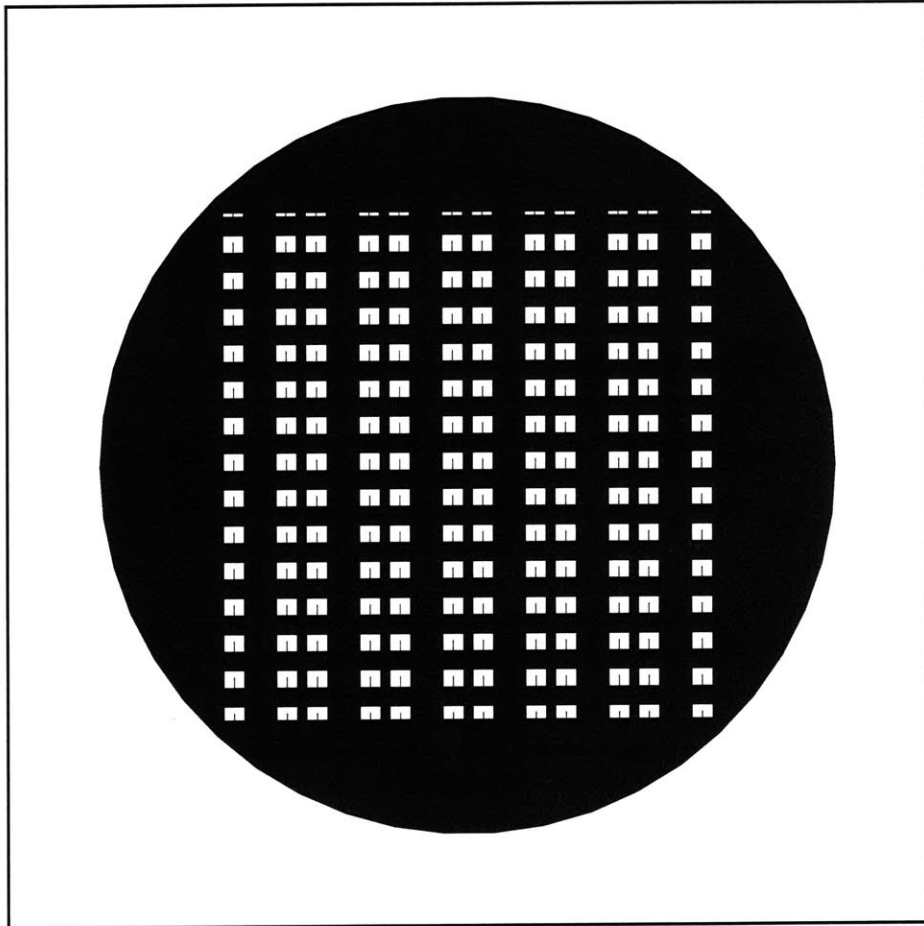
Figure E-3: Shadow mask

Appendix F

Processes

Table F.1 is used for fabricating the zipping actuator-relay system that is described in Chapter 3. As described in Section 4.2.5, Table F.2 is the process used for fabricating a full relay combining the DRIE-etched actuator/relay and the KOH-etched relay contacts. Both processes are realized or to be realized at the MTL at MIT.

Masks: 3 Chrome Masks. One for handle wafer shallow etching,
one for device wafer structure through etching,
the other one for striping oxide on contact pad.
Wafers: 4" blank Silicon wafer $\langle 100 \rangle$, $0.008 \sim 0.015$ Ωcm n type,
double side polished, 300μm thick.

step#	Lab	Machine	Recipe	Description
			Handle Wafer(Pyrex) waer #w1	
1	TRL	Pre-metal	Piranha clean	
2	TRL	ebeam	Metal deposition	50 Åof Au, 300 Åof Cr
3	TRL	HMDS	HMDS	25 Å
4	TRL	Coater	20 μm	Double,20 μm positive
5	TRL	Prebake	90 °C, 60min	Pre bake
6	TRL	EV1	$\sim$ 45 s	Exposure, mask # m1
7	TRL	Photo-Wet-1	3$\sim$4 min	Develop P.R
8	TRL	Postbake	30 min	Post bake
9	TRL	Acid hood	Straight HF Etch	About 3 min for 20 μm
10	TRL	Acid hood	Piranha clean	Strip PR/clean
			Device Wafer wafer #w2	
11	TRL	Acid hood	Piranha clean	
12	TRL	HMDS	HMDS	$\sim$ 25 Å
13	TRL	Coater	Coat	12μm positive P.R
14	TRL	Prebake oven	90 °C, 30min	Pre bake
15	TRL	EV1 15s	Exposure,	Mask #m2
16	TRL	Photo-Wet-1	3$\sim$4 min	Develop P.R
17	TRL	Postbake	30 min	Post bake
18	TRL	STS2	500 μm	Etch through
19	TRL	Acid hood	Piranha Clean	Strip P.R
20	TRL	RCA	RCA Clean	
21	TRL	TubeA2	Oxidation	$\sim$ 2000 Å
			Shadow wafer (#w3)	
22	TRL	Acid hood	Piranha clean	
23	TRL	HMDS HMDS	$\sim$ 25 Å	
24	TRL	Coater	12 μm	12 μm positive P.R
25	TRL	Pre-bake oven	90 °C, 30 min	Pre bake
26	TRL	EV1 15 s	Exposure	masks #m3
27	TRL	Photo-Wet-1	3$\sim$4 min	Develop P.R
28	TRL	Postbake	30 min	Post bake
29	TRL	STS2 300 μm	Etch through	
30	TRL	Acid hood	Piranha Clean	Strip P.R

156

Oxide etching of device wafer (# w2)				
31	TRL	Acid hood	Piranha clean	
32	TRL	EV501		Mount #w3 on #w2
33	TRL	Prebake oven	90 °C, 30 min	Pre bake
34	TRL	Plasmaquest	SiO2 Strip	from both sides
35	TRL	Acid hood	Piranha Clean	Dismounting, Clean
Bonding Handle Wafer and Device Wafer				
36	TRL	Acid hood	Piranha clean	Clean #w1 and #2
37	TRL	Evaligner-bonder	Anodic Bonding	bond #w1 and #w2

Table F.1: fabrication process for the actuator

Masks: 7 Masks. One for handle wafer shallow etching, one for device wafer
structure through etching two for top/bottom side KOH mask etching, one for
striping oxide on contact pad and two for metal sputtering.Wafers: 4" blank
Silicon wafer $\langle 100 \rangle$, n type, $0.008 \sim 0.015 \ \Omega$ cm, double side polished,
300 μm thick.

step#	Lab	Machine	Recipe	Description
Handle wafer (Pyrex) (#w1)				
1	TRL	Pre-metal	Piranha clean	
2	TRL	ebeam	Metal deposition	50 Åof Au, 300 Åof Cr
3	TRL	HMDS	HMDS	25 Å
4	TRL	Coater	20 μm	Double layer, 20 μm positive
5	TRL	Prebake	90 °C, 60min	Pre bake
6	TRL	EV1	$\sim$ 45 s	Exposure, Mask # m1
7	TRL	Photo-Wet-1	3~4 min	Develop P.R
8	TRL	Postbake	30 min	Post bake
9	TRL	Acid hood	Straight HF Etch	About 3 min for 20 μm
10	TRL	Acid hood	Piranha clean	Strip PR/clean
Device wafer (#w2)				
11	TRL	Acid hood	Piranha clean	
12	TRL	HMDS	HMDS	$\sim$25
13	TRL	Coater	12 μm	Coat 12 μm positive P.R
14	TRL	Prebake oven	90 °C, 30 min	Pre bake
15	TRL	EV1	15 s Exposure,	Mask # m2: device features
16	TRL	Photo-Wet-1	3~4 min	Develop P.R.
17	TRL	Postbake	30 min	Post bake
18	TRL	STS2/3	300 μm	Etch through
19	TRL	Acid hood	Piranha Clean	Strip P.R
20	ICL	RCA	RCA Clean	
21	ICL	Tube 6D	LPCVD Nitride	2000 Å
5 Shadow wafers (# w3, w4, w5, w6 and w7)				
22	TRL	Acid hood	Piranha clean	
23	TRL	HMDS HMDS	$\sim$ 25 Å	
24	TRL	Coater	12 μm	Coat 12 μm positive P.R
25	TRL	Pre-bake oven	90 °C, 30 min	Pre bake
26	TRL	EV1 15 s	Exposure	masks #m3~m7
27	TRL	Photo-Wet-1	3~4 min	Develop P.R
28	TRL	Postbake	30 min	Post bake
29	TRL	STS2 300 μm	Etch through	
30	TRL	Acid hood	Piranha Clean	Strip P.R

Nitride etching of device wafer (# w2)			
31	TRL	Acid hood	Piranha clean	
32	TRL	EV501		Mount #w3 & #w4 on #w2
33	TRL	Prebake oven	90 °C, 30 min	Pre bake
34	TRL	Plasmaquest	Nitride Strip	from both sides
35	TRL	Acid hood	Piranha Clean	Dismounting, Clean
KOH etching of the device wafer (#w2)			
36	ICL	KOH hood	KOH etch	~2 hours, both sides
37	EML	Acid hood	Piranha clean	Clean the wafer
Bonding handle wafer (#w1) and device wafer (# w2)			
38	TRL	EV501	Anodic Bonding	Bond #w1 & #w2
Nitride etching for contact			
39	TRL	EV 501	mounting	#w5 & #w2
40	TRL	Plasmaquest	Oxide etching	Etch 2000 Å
Metal sputtering			
41	TRL	EV 501	mounting	Shadow wafer #w6, #w7 & #w2)
42	EML	Sputterer	Au Sputtering	100 ÅTi + 0.7 μm Au, both sides
43	EML	Acid hood	Piranha clean	Clean, dismounting
The end			

Table F.2: fabrication process for the actuator and KOH-etched relay contacts

Bibliography

[1] J. Li, M. P. Brenner, J. H. Lang, A. H. Slocum, and R. Struempler. Drie-fabricated curved-electrode zipping actuators with low pull-in voltage. In *Proc. 12th Int. Conf. Solid-State Sensors and Actuators*, pages 480–483, Boston, June 2003.

[2] J. Li, M. P. Brenner, J. H. Lang, and A. H. Slocum. Drie etched electrostatic curved-electrode zipping actuators. *submitted to J. Microeletromech. Syst.*

[3] M. Shikida and K. Sate. Fabrication of an s-shaped actuator. *J. Microeletromech. Syst.*, 6(1):18–24, 1997.

[4] R. Legtenberg, J. Gilbert, and S. D. Senturia. Curved electrode actuators. *J. Microeletromech. Syst.*, 6(3):257–265, 1997.

[5] N. Maluf. *An Introduction to Microelectromechanical Systems Engineering*, chapter 1. Boston: Artech House, 2000.

[6] S. D. Senturia. *Microsystem Design*, chapter 1. Kluwer Academic Publishers, 2000.

[7] K. D. Wise. Special issue on integrated sensors, microactuators, and microsystems (mems). *Proceedings of the IEEE*, 86(8):1531–1787, August 1998.

[8] N. Yazdi, F. Ayazi, and K. Najafi. Micromachined inertial sensors. *Proceedings of the IEEE*, 86(8):1640–1659, August 1998.

[9] P. F. Van Kessel, L. J. Hornbeck, R. E. Meier, and M. R. Douglas. A mems-based projection display. *Proceedings of the IEEE*, 98:1687–1704, 1998.

[10] S. J. Walker and D. J. Nagel. Optics and mems. In *Tech. Rep. NRL/MR/6336-99-7975*, Naval Res. Lab, Washington DC, 1999. PDF version available at http://mstd.nrl.navy.mil/6330/6336/Moems.pdf.

[11] F. E. H. Tay. *Microfluidics and BioMEMS applications*. Boston : Kluwer Academic Publishers, 2002.

[12] H. J. De Los Santos. *Introduction to Microelectromechanical (MEM) Microwafer Systems*. Artech House, Norwood, MA, 1999.

[13] M. A. Schmidt. Wafer-to-wafer bonding for microstructure formation. *Proc. IEEE*, 86:1575–1585, 1998.

[14] E. Thielicke and E. Obermeier. Microactuators and their technologies. *Mechatronics*, 10:431–455, 2000.

[15] M. Tabib-Azar. *Microactuators*. Kluwer Academic Publishers, Boston/Dordrecht/London, 1998.

[16] H. Miyajima, N. Asaoka, T. Isokawa, M. Ogata, Y. Aoki, M. Imai, O. Fujimori, M. Katashiro, and K. Matsumoto. A mems electromagnetic optical scanner for a commercial confocal laser scanning microscope. *J. Microeletromech. Syst.*, 12(3):243–251, 2003.

[17] E. Thielicke and E. Obermeier. New moems-switch device with electrostatic actuator. In *Proc. IEEE/LEOS Optical MEMS*, pages 159–160, Lugano, Switzerland, August 2002.

[18] H. Schlaak, F. Arndt, J. Schimkat, and M. Hanke. Silicon microrelay with electrostatic moving wedge actuator. In *Proc. Fifth Int. Conf. on Microelectrooptomechanical Systems and Components*, pages 463–468, Potsdam, 1996.

[19] Jo-Ey Wong, Jeffrey Lang, and Martin Schmidt. An electrostatically-actuated mems switch for power app-lication. In *Proc. IEEE 13th Ann. Int. Conf. Micro Electro Mechanical Syst.*, pages –, Miyazaki, Japan, January 2000.

[20] Collin A. Rich and Kensall D. Wise. A high-flow thermopneumatic microvalve with improved efficiency and integrated state sensing. *J. Microeletromech. Syst.*, 12(2):201–207, 2003.

[21] D. Maillefer, H. van Linte, G. Rey-Mermet, and R. Hirschi. A high-performance silicon micropump for an implantable drug delivery system. In *Proc. IEEE International Workshop on Micro Electro Mechanical Systems*, pages 541–546, Orlando, USA, February 1999.

[22] William L. Benard, Harold Kahn, Arthur H. Heuer, and Michael A. Huff. Thin-film shape-memory alloy actuated micropumps. *J. Microeletromech. Syst.*, 7(2):245–261, 1998.

[23] J. Qiu, J. Lang, and A. Slocum. A centrally-clamped parallel-beam bistable mems mechanism. In *Proc. IEEE International Workshop on Micro Electro Mechanical Systems*, pages 353–356, Switzerland, January 2001.

[24] J. Qiu. *An Electrothermally-Actuated Bistable MEMS Relay for Power Applications*. PhD thesis, Massachusetts Institute of Technology, 2003.

[25] J. Qiu, J. Lang, A. Slocum, and R. Struempler. A high-current electrothermal bistable mems relay. In *Proc. IEEE International Workshop on Micro Electro Mechanical Systems*, pages 64–67, Japan, January 2003.

[26] Z. Li, D. Zhang, T. Li, W. Wang, and G. Wu. Bulk micromachined relay with lateral contact. *J. Micromech. Microeng.*, 10(3):329–333, 2000.

[27] E. H. Yang, R. Dekany, and S. Padin. Design and fabrication of a large vertical travel silicon inchworm microactuator for advanced segmented silicon space telescope (assist). In *SPIE Photonics West, Micromachining and Microfabrication Converence*, San Jose, USA, January 2003.

[28] W. Tang, T. Nguyen, and R. Howe. Laterally driven polysilicon resonant microstructures. *Sens. Actuators*, 20:25–32, 1989.

[29] A. A. Ayon, C. C. Lin, R. A. Braff, and M. A. Schmidt. Etching characteristics and profile control in a time multiplexed inductively coupled plasma etcher. In *Proc. 1998 Solid-State Sensor, Actuator, and Microsystems Workshop*, pages 41–44, Hilton Head, USA, June 1998.

[30] C. Yeh and K. Najafi. Cmos interface circuitry for a low-voltage micromachined tunneling accelerometer. *J. Microeletromech. Syst.*, 7:6–15, 1998.

[31] C. H. Liu and T. W. Kenny et al. Characterization of a high-sensitivity micromachined tunneling accelerometer with micro-g resolution. *J. Microeletromech. Syst.*, 7(2):235–244, 1998.

[32] G. Vdovin, P. M. Sarro, and S. Middelhoek. Technology and applications of micromachined adaptive mirrors. *J. Micromech. Microeng.*, 9(2):8–19, 1999.

[33] P. M. Zavracky, N. E. McGruer, R. H. Morrison, and D. Potter. Microswitches and microrelays with a view toward microwave applications. *Int. J. RF Microwave Comput.-Aided Eng.*, 9(4):338–347, 1999.

[34] L. Yobas, M. A. Huff, F. J. Lisy, and D. M. Durand. A novel bulk-micromachined electrostatic microvalve with a curved-compliant structure applicable for a pneumatic tactile display. *J. Microeletromech. Syst.*, 10(2):187–196, 2001.

[35] T.Ohnstein, T. Fukiura, J. Ridley, and U. Bonne. Micromachined silicon microvalve. In *Proc. IEEE Ann. Int. Conf. Micro Electro Mechanical Syst.*, pages 95–98, January 1990.

[36] C. Divoux, J. Charton, W. Schwartz, E. Stadler, J. Margaill, L. Jocou, T. Enotl, J.C. Barbel, J. Chiaroni1, and P. Berruyer. A novel electrostatic actuator for micro deformable mirrors: Fabrication and test. In *Proc. 12th Int. Conf. Solid-State Sensors and Actuators*, pages 488 481, Boston, June 2003.

[37] T-K A. Chou and K. Najafi. Fabrication of out-of-plane curved surfaces in si by utilizing rie lag. In *Proc. IEEE International Workshop on Micro Electro Mechanical Systems*, pages 145–148, Switzerland, January 2002.

[38] H. S. Kim and K. Najafi. Large deflection out-of-plane electrostatic buckled electrode actuators. In *Proc. 12th Int. Conf. Solid-State Sensors and Actuators*, pages 794–797, Boston, June 2003.

[39] G. Perregaux, S. Gonseth, P. Debergh, J. Thiebaud, and H. Vuillioenet. Arrays of addressable high-speed optical microshutters. In *Proc. IEEE 14th Ann. Int. Conf. Micro Electro Mechanical Syst.*, pages 232–235, Switzerland, January 2001.

[40] F. Sherman, C.-J. Kim, J. Woo, and C.-M. Ho. In-plane microactuator for fluid control application. In *Proc. IEEE 11th Ann. Int. Conf. Micro Electro Mechanical Syst.*, pages 454–459, Heidelberg, Germany, January 1998.

[41] F.Bennini, J. Fruhauf, and W. Dotzel. High force and large displacement electrostatic actuators with curved electrode using silicon bulk micromachinng. In *Proc. 7th International Conference on New Actuators (Actuator 2000)*, pages 87–90, Bremen, Germany, June 2000.

[42] G. Smith, J. Maloney, L. Fan, and D. L. DeVoe. Large displacement microactuators in deep reactive ion etched single crystal silicon. In *Proc. of SPIE, Vol 4559*, pages 144–147, January 2001.

[43] J. Branebjerg and P. Gravesen. A new electrostatic actuator providing improved stroke length and force. In *Proc. IEEE International Workshop on Micro Electro Mechanical Systems*, pages 6–11, Germany, February 1992.

[44] M. Elwenspoe, L. Smith, and B. Hok. Active joints for micro robot limbs. In *Proc. IEEE International Workshop on Micro Electro Mechanical Systems*, pages 37–41, Germany, February 1992.

[45] A. H. Slocum. Precision machine design: Macromachine design philosophy and its applicability to the design of micromachines. In *IEEE International Workshop on Micro Electro Mechanical Systems*, pages –, Germany, February 1992.

[46] M. P. Brenner, J. H. Lang, J. Li, J. Qiu, and A. H. Slocum. Optimum design of a mems relay switch. In *Proc. Modeling and Simulation of Microsystems*, pages 64–67, San Juan, Puerto Rico, USA, April 2002.

[47] M. P. Brenner, J. H. Lang, J. Li, J. Qiu, and A. H. Slocum. Optimal design of a bistable switch. *PNAS*, 100(17):9663–9667, 2003.

[48] M. Madou. *Fundamentals of Microfabrication*. New York: CRC Press, 1997.

[49] M. P. Brenner, J. H. Lang, J. Li, and A. H. Slocum. Optimum design of an electrostatic zipper actuator. In *Proc. Modeling and Simulation of Microsystems*, Boston, USA, March 2004.

[50] L. Kantorovich and G. Akilov. *Functional Analysis in Normed Spaces*. Macmillan, New York, 1964.

[51] S. S. Rao. *Mechanical Vibrations*, chapter 8. Addison-Wesley Publishing Company, 1995.

[52] J. Zhang and T. H. Gong. Micromachining technologies for capillary electrophoresis utilizing pyrex glass etching and bonding. In *Proc. SPIE v 4174*, pages 356–362, January 2000.

[53] T. Cormany, P. Enoksson, and G. Stemme. Deep wet etching of borosilicate glass using an anodically bonded silicon substrate as mask. *J. Micromech. Microeng.*, 8(2):84–87, 1998.

[54] K. Chen, A. A. Ayon, X. Zhang, and S. M. Spearing. Effect of process parameters on the surface morphology and mechanical performance of silicon structures after deep reactive ion etching (drie). *J. Microeletromech. Syst.*, 11(3):264–275, 2002.

[55] M. Walker. Comparison of bosch and cryogenic process for patterning high aspect ratio features in silicon. In *Proc. Int. Conf. on Microelectronic and MEMS Technologies, SPIE-4407*, pages 89–99, Edinburgh, UK, 2001.

[56] J. Qiu, J. Sihler, J. Li, and A. H. Slocum. An instrument to measure the stiffness of mems mechanisms. In *Proc. 10th International Conference on Precision Engineering*, pages 599–603, Yokohama, Japan, July 2001.

[57] C. Cabuz, E. I. Cabuz, T. R. Ohnstein, J. Neus, and R. Maboudian. Factors enhancing the reliability of touch-mode electrostatic actuators. *Sensors and Actuators A*, 79:245–25, 2000.

[58] B. McCarthy, G. G. Adams, N. McGruer, and D. Potter. A dynamic model, including contact bounce, of an electrostatically actuated microswitch. *J. Microeletromech. Syst.*, 11(3):276–283, 2002.

[59] Y.-J. Yang and S. D. Senturia. Numerical simulation of compressible squeezed-film damping. In *Proc. 1996 Solid-State Sensor, Actuator, and Microsystems Workshop*, pages 76–79, Hilton Head, USA, June 1996.

[60] B. J. Hamrock. *Fundamentals of Fluid Film Lubrication*. New York: McGraw-Hill, 1994.

[61] S. A. Campbell. *The Science and Engineering of Microelectronic Fabrication*. New York: Oxford University Press, 1996.

[62] H. Seidel et al. Anisotropic etching of crystalling silicon in alkaline solutions. *J. Electrochemical Society*, 137(11):3612–3632, 1990.

[63] Q. Zhang et al. A new approach to convex corner compensation for anisotropic etching of (100) si in koh. *Sens. Actuators A*, 56:251–254, 1996.

[64] Mattias Vangboy and Ylva Backlund. Precise mask alignment to the crystallographic orientation of silicon wafers using wet anisotropic etchingbulk. *J. Micromech. Microeng.*, 6(3):279–284, 1996.

[65] Mattias Vangboy and Ylva Backlund. Terracing of (100)-si with one mask and one etching step using misaligned. *J. Micromech. Microeng.*, 6:39–41, 1996.

[66] J. Sihler. *A Low Leakage 3-Way Silicon Microvalve*. PhD thesis, Massachusetts Institute of Technology, 2004.